

**MICROSTRUCTURES AND MECHANICAL PROPERTIES OF  
PALLADIUM–SILVER DENTAL CASTING ALLOYS**

DISSERTATION

Presented in Partial Fulfillment of the Requirements for  
the Degree Doctor of Philosophy  
in the Graduate School of The Ohio State University

By

Dongfa Li, B.S., M.S., M.S.

\* \* \* \* \*

The Ohio State University

2006

Dissertation Committee:

Dr. William A. Brantley, Adviser

Dr. Glenn S. Daehn

Dr. William M. Johnston

Approved by

---

Adviser

Oral Biology Graduate Program

## ABSTRACT

In recent years, with the cost of palladium less than that for gold, palladium–silver dental casting alloys have gained renewed interest for dental metal-ceramic restorations due to their economic advantages and favorable properties. The objective of this study was to characterize the microstructures and mechanical properties of palladium–silver dental casting alloys. Six commercial alloys were selected: Rx 91 (Pentron); Super Star (Heraeus Kulzer); W-1, Aries, IS 64, and d.SIGN 59 (Ivoclar Vivadent). Following standard dental laboratory procedures, the alloys were melted with a multi-orifice gas-oxygen torch and centrifugally cast into two types of specimens. The first type simulated a coping for a maxillary central incisor restoration, and the second type met the dimensional requirements of ADA Specification Nos. 5 and 38 for tensile test bars, with gauge dimensions of 3 mm diameter  $\times$  15 mm length. Slices with a thickness of 1 mm were also sectioned from the bar specimens for microstructural study. Three kinds of heat treatment were conducted: the entire simulated porcelain-firing process; the cumulative effect of each individual step of the simulated porcelain-firing process, and isothermal annealing for 0.5 hour at step intervals of 50°C from 400° to 950°C. Vickers hardness measurements (which correlate with alloy yield strength) were obtained using 1 kg load for bulk hardness and a light 10 g or 25 g load for individual phase or constituent regions. Tensile tests and uniaxial tension-compression fatigue tests were carried out on bar

specimens that were subjected to heat treatment simulating the full porcelain-firing cycles. The crosshead speed used for the tensile test was 2 mm/min. The R ratio for the compression and tension stress amplitudes was  $-1$ , and the frequency was 10 Hz. The highest stress at which fracture did not occur after a clinically relevant number of 2 million cycles was designated as the fatigue limit. The optical microscope, scanning electron microscope (SEM), and transmission electron microscope (TEM) were employed to study the porosity, microstructures and fracture surfaces.

In the as-cast condition, W-1 had a typical dendritic microstructure, whereas the other five alloys exhibited a nearly equiaxed grain structure with some evidence of residual dendritic character. After the simulated porcelain-firing heat treatment, the nearly equiaxed as-cast grain structure in the coping and slice specimens were fully homogenized and numerous precipitates were present. However, except for Aries, the microstructure was not completely homogenized in all of the relatively larger bar specimens for the tensile and fatigue tests. Besides discontinuous grain boundary precipitates, two other precipitate morphologies were observed within grains: spherical precipitates and platelet-like precipitates, which formed in alloys with relatively lower and higher indium contents, respectively. The as-cast dendritic structure in W-1 was retained after the simulated porcelain-firing heat treatment and the annealing heat treatments. During the simulated porcelain-firing process after the initial alloy oxidation, the Vickers hardness reached highest values in three alloys: Aries, IS 64 and d.SIGN 59. After each of the subsequent heat treatment steps that simulated the firing of additional porcelain layers, the Vickers hardness had no substantial changes. During annealing

heat-treatment, Super Star showed two hardness peaks at approximately 500° and 650°C, while the other five alloys exhibited one hardness peak in the temperature range from 550° to 700°C.

The TEM microstructures of the as-cast W-1 and Rx 91 were similar, and three phases were observed: solid solution matrix, ordered face-centered cubic (fcc) granular precipitates, and ordered fine-scale face-centered tetragonal (fct) precipitates. After simulated porcelain-firing heat-treatment, the original granular precipitates remained, and new smaller granular precipitates appeared. In the annealing temperature range, Rx 91 exhibited the same TEM microstructure as in the as-cast condition. Super Star, however, had a complicated TEM microstructure, and two kinds of new precipitates were observed when annealing was performed at temperatures corresponding to the two hardening peaks.

In the presence of porosity up to 4%, Aries, IS 64, and d.SIGN 59 exhibited acceptable mechanical properties for clinical use. Casting porosity and variation in microstructures were considered the causes of variation in mechanical properties among specimens of the same alloy. The fatigue limits of Super Star, Rx 91, W-1, IS 64 and d.SIGN 59 were approximately in the range of 15% to 25% of the 0.2% offset yield strength. The general insensitivity of fatigue limit to casting porosity for most IS 64 and d.SIGN 59 specimens suggests that there is a critical pore size, above which fatigue resistance is decreased significantly. During fatigue, slip in the Pd solid solution matrix is a common permanent deformation mechanism, while twinning could provide an additional permanent deformation mode. The low ratio of fatigue limit to yield strength for the Pd–Ag alloys tested is attributed to their complex microstructures and casting defects.

Dedicated to my wife Yinyan and son Edward

## ACKNOWLEDGMENTS

I would like to express my sincere appreciation to my adviser, Dr. William A. Brantley, for his guidance and support for this expensive research. His deep scientific knowledge, insight, kindness, considerateness and tremendous patience make him not only a great mentor but also like a dear parent.

I wish to extend my sincere thanks to Dr. Glenn S. Daehn for his valuable suggestions and Dr. William M. Johnston for his kind assistance and data analysis for this study. I would like to thank Tridib Dasgupta, Director of Materials Research at Ivoclar Vivadent (US) for providing tensile testing specimens, performing tensile test, and helpful comments on the properties of Pd–Ag alloys.

I thank Dr. Reza Heshmati for casting and heat-treating alloy specimens, Mr. Lloyd Barnhart in the Department of Materials Science and Engineering for fatigue testing, Dr. Wenhua Guo for TEM observation, and Dr. Satish Alapati for SEM examination. I also thank all other members in our research group, Dr. Naoki Baba, Dr. Xingxue Hu, Dr. Yurdanur Sanli, Dr. Ruohong Liu, Dr. David Li and Dr. Frank Meng for various help and support. Thanks also go to Mr. Andrew Stevenson in the Fixed Prosthodontics Laboratory, Dr. Sreenivas Bhattiprolu at the Microscopic and chemical Analysis Research Center, Mr. Steven Bright in the Materials Science and Engineering Department, Mrs. Laura Kelley in the College of Dentistry, Mr. Carl Kipp, Ms. Connie

Mason, Dr. Sunny Skaria and Ms. Andrea Anderson in the Section of Restorative and Prosthetic Dentistry for help in my research. I want to thank many other people at the University and the College of Dentistry who provided me various kinds of help while all of their names are not listed here.

Finally, I extend my love and gratitude to my wife Yinyan and son Edward for their patience, love, and continuous support.

Financial support for this investigation was provided by NIDCR Grant DE 10147.

## VITA

November 1967	.....	Born in Hubei, China
July 1988	.....	B.S., Materials Science & Engineering Huazhong University of Science & Technology Wuhan, Hubei, China
July 1991	.....	M.S., Materials Science & Engineering Institute of Metal Research Chinese Academy of Sciences Shenyang, Liaoning, China
July 1991 – August 1998	.....	Research Scientist Institute of Metal Research Chinese Academy of Sciences Shenyang, Liaoning, China
March 1996 – August 1998 (Concurrent)	.....	National Natural Science Foundation of China Beijing, China
January 1999 – Present	.....	Graduate Research Associate The Ohio State University Columbus, Ohio
June 2001	.....	M.S., Dental Materials The Ohio State University Columbus, Ohio

## PUBLICATIONS

1. Li D, Brantley WA, Mitchell JC, Daehn GS, Monaghan P, Papazoglou E. Fatigue studies of high-palladium dental casting alloys: Part I. Fatigue strengths and fracture characteristics. *Journal of Materials Science: Materials in Medicine* 13 (2002).

2. Guo WH, Brantley WA, Li D, Monaghan P, Clark WAT. Fatigue studies of high-palladium dental casting alloys: Part II. Transmission electron microscopic observations. *Journal of Materials Science: Materials in Medicine* 13 (2002).
3. D.F. Li, X.M. Zhang, E. Gautier, and J.S. Zhang. Morphology transitions of deformation-induced thin plate martensite in Fe-Ni-C alloys. *Acta Mater.* Vol. 46, No.13 (1998).
4. C.H. Zhou, K. Yang, D.F. Li, Y.X. Lu. Hydrogen effect on deformation behavior of titanium alloy at high temperature. *Acta Metallurgica Sinica* (English Letters). Vol. 11, No. 3 (1998).
5. D.F. Li, C.G. Fan, Y.Y. Li, and H.M. Cheng. Tensile properties and deformation-induced martensitic transformation at cryogenic temperatures in Fe-Cr-Ni-Mn-N alloys. *Advances in Cryogenic Engineering* Vol. 42A. Plenum Press, New York (1997).
6. Yang K, Zhou CH, and Li DF. The thermal plasticity of titanium alloys and fabrication of Ti-based composites by hydrogenation. *Journal of Rare Metals and Engineering* 26, No.1 (1997) (in Chinese).
7. Y.N. Liang, S.Z. Li, and D.F. Li. Some development for single-pass pendulum scratching. *Wear* 199 (1996).
8. A.C. Wang, Y.Y. Li, K. Yang, D.F. Li, C.G. Fan and C.X. Shi. Effect of P (Mn) content on the coarsening of  $\gamma'$  in Incoloy 903. *Materials Letters* 23 (1995).
9. A.C. Wang, Y.Y. Li, K. Yang, D.F. Li, C.G. Fan. Study of the effect of P on the EDC of some elements in Fe-based ternary systems by thermodynamic evaluation. *Materials Letters* 24 (1995).
10. Wang Anchuan, Li Yiyi, Li Dongfa, Yang Ke, Fan Cungan, and Shi Changxu. Effects Nb and Ti contents on micro-segregation of J90 alloy. *Acta Mater. Sinica* Vol. 31, 1995 (in Chinese).
11. Xu Zhao, Dongfa Li, Ke Yang, Cungan Fan, and Yiyi Li. Growth kinetics of  $\gamma'$  particles in Incoloy 907. *J. Mat. Sci. Technol.* Vol. 10 (1994).
12. A.C. Wang, Y.Y. Li, D.F. Li, K. Yang, and C.G. Fan. Effect of segregation on the cryogenic mechanical properties of some precipitation-hardened austenitic alloys. *Advances in Cryogenic Engineering (Mater.)* Vol. 40. Plenum Press, New York (1994).
13. A.C. Wang, C.G. Fan, D.F. Li, X. Zhao, K. Yang, Y.Y. Li, and C.X. Shi. Effects of strengthening particle size on hydrogen performance of Incoloy 903. *J. Mater. Sci. Lett.* 13 (1994).

14. X.M. Zhang, D.F. Li, Z.S. Xing, E. Gautier, J.S. Zhang, and A. Simon. Morphology transition of deformation-induced lenticular martensite in Fe-Ni-C Alloys. *Acta Metall. Mater.* Vol. 41, No. 6 (1993).
15. Q.Y. Long, Z. Zhu, X.M. Zhang, and D.F. Li. Acoustic emission of martensitic transformation induced by strain during tensile testing in a Fe-Ni-C alloy. *Scrip. Metall. Mater.* 26 (1992).
16. X.M. Zhang, D.F. Li, X. Zhao, Z.S. Xing, J.S. Zhang, E. Gautier, A. Simon. Morphology transitions of deformation-induced martensites in Fe-Ni-C alloys. *Proc. International Conference on Martensitic Transformations (1992)*. Monterey Institute for Advanced Studies 1993. Monterey, CA, USA.

#### FIELDS OF STUDY

Major Field: Oral Biology

## TABLE OF CONTENTS

	<u>Page</u>
Abstract.....	ii
Dedication.....	v
Acknowledgments.....	vi
Vita.....	viii
List of Tables.....	xv
List of Figures.....	xvii
Chapters:	
1. Introduction and Background for Study.....	1
1.1 General Background of Dental Casting Alloys.....	1
1.2 High-Palladium Dental Casting Alloys.....	4
1.2.1 Historical Background.....	4
1.2.2 Compositions, Microstructures and Mechanical Properties of High-Palladium Alloys.....	5
1.2.3 Microstructures of Plastically Deformed and Fatigued High- Palladium Alloys Observed with TEM.....	9
1.2.4 Adherence of Porcelain to High-Palladium Alloys and Mechanisms for Surface Oxide Formation.....	11
1.2.5 Palladium Corrosion and Biocompatibility of High-Palladium Dental Alloys.....	13
1.3 Palladium–Silver Dental Casting Alloys.....	16
1.3.1 Background.....	16

1.3.2	Compositions, Microstructures and Mechanical Properties of Palladium–Silver Alloys.....	17
1.3.3	Corrosion and Biocompatibility of Palladium–Silver Dental Alloys.....	20
1.4	Purpose of This Study.....	22
2.	Microstructures and Tensile Properties of Palladium–Silver Alloys for Metal–Ceramic Restorations.....	37
2.1	Introduction.....	37
2.2	Materials and Methods.....	39
2.3	Results.....	40
2.3.1	Mechanical Properties.....	41
2.3.2	Porosity and Microstructures of Sectioned Specimens.....	41
2.3.3	SEM Examination of Fracture Surfaces.....	42
2.4	Discussion.....	43
2.5	Conclusions.....	46
3.	Effects of Porcelain-Firing and Isothermal Treatment on the Microstructures and Hardness of Palladium–Silver Alloys.....	57
3.1	Introduction.....	57
3.2	Materials and Methods.....	60
3.3	Results.....	61
3.3.1	Hardness Variation During Porcelain Firing Process.....	61
3.3.2	Hardness vs. Annealing Temperatures.....	61
3.3.3	Microstructural Changes During Porcelain Firing Process.....	61
3.3.4	Microstructural Variation During Annealing Heat Treatment.....	62
3.4	Discussion.....	63
3.5	Conclusions.....	65
4.	Annealing Study, Vickers Hardness Measurements and Microstructural Observations of Palladium–Silver Dental Alloys.....	75

4.1	Introduction.....	75
4.2	Materials and Methods.....	77
4.3	Results.....	78
	4.3.1 Hardness <i>vs.</i> Annealing Temperatures.....	78
	4.3.2 Microstructural Observation.....	80
4.4	Discussion.....	82
4.5	Conclusions.....	85
5.	Transmission Electron Microscopic Study of Palladium–Silver Dental Casting Alloys.....	96
	5.1 Introduction.....	96
	5.2 Materials and Methods.....	98
	5.3 Results.....	99
	5.3.1 Microstructures of As-Cast and Simulated Porcelain-Firing Heat-Treated W-1 and RX 91.....	99
	5.3.2 Microstructures in Rx 91 and Super Star after Annealing Heat Treatment.....	99
	5.4 Discussion.....	100
	5.5 Conclusions.....	103
6.	Fatigue Limits and SEM/TEM Observations of Fracture Characteristics for Pd Ag Alloys.....	111
	6.1 Introduction.....	111
	6.2 Materials and Methods.....	113
	6.3 Results .....	115
	6.3.1 Microstructures and Fatigue Limits of Pd–Ag Alloys.....	115
	6.3.2 Fracture and Microstructural Characteristics of Fatigued Pd–Ag Alloys.....	116

6.4 Discussion.....	117
6.5 Conclusions.....	120
7. Microstructures and Fatigue Behavior of Two Commercial Pd–Ag Dental Casting Alloys in the Presence of Casting Porosity.....	132
7.1 Introduction.....	132
7.2 Materials and Methods.....	134
7.3 Results.....	137
7.3.1 Microstructures.....	137
7.3.2 Vickers Hardness.....	137
7.3.3 Fatigue Limits.....	138
7.3.4 Casting Porosity and Fracture Characteristics.....	138
7.4 Discussion.....	139
7.4.1 Specimen Size and Microstructures.....	139
7.4.2 Comparison of Fatigue Properties for IS 64 and d.SIGN59.....	140
7.4.3 Effects of Specimen Size and Casting Porosity on Fatigue Performance.....	141
7.5 Conclusions.....	143
Bibliography.....	154

## LIST OF TABLES

<u>Table</u>	<u>Page</u>
1.1 Alloy classification of the American Dental Association.....	23
1.2 Mechanical property requirements in ANSI/ADA Specification No. 5 for dental casting alloys.....	23
1.3 Compositions (wt.%) of high-palladium dental alloys (provided by manufacturers).....	24
1.4 Properties of the alloys in Table 1.3 after simulated porcelain firing heat treatment (provided by manufactures).....	25
1.5 Mechanical properties of one dendritic and two equiaxed fine-grained high-palladium alloys.....	26
1.6 Mechanical properties of three dendritic Pd-Cu-Ga high-palladium alloys.....	27
1.7 Number of cycles to failure of all-new metal Spartan Plus and Protocol tested at different amplitudes (loads).....	28
1.8 Number of cycles to failure for 50/50% Spartan Plus and Protocol and all-old metal Spartan Plus tested at different stress amplitudes (loads).....	29
1.9 Elemental release ( $\mu\text{g}/\text{cm}^2$ ) from Liberty and Legacy into corrosion medium.....	30
1.10 Compositions (wt. %) of palladium–silver dental alloys (provided by manufacturers).....	31
1.11 Properties of the alloys in Table 1.10 after simulated porcelain firing heat treatment (provided by manufactures).....	32
2.1 Nominal compositions of Aries, IS 64 and d.SIGN 59 (provided by Ivoclar Vivadent).....	47

<u>Table</u>	<u>Page</u>
2.2 Summary of Two-way ANOVA results for comparison of mechanical property measurements.....	47
2.3 Mechanical properties of Aries, IS 64 and d.SIGN 59. Groups in the same column with the same letters are not significantly different ( $P > 0.05$ ).....	48
2.4 Mechanical properties, porosity area fraction and maximum equivalent pore diameter of specimens with the lowest and highest 0.2% yield strength in each testing group in Table 2.3.....	49
3.1 Initial alloy oxidation procedure and porcelain-firing process for IPS Classic.....	67
4.1 Nominal compositions (wt. %) and mechanical properties reported by the manufacturers for the three Pd–Ag dental alloys studied.....	86
6.1 Nominal mechanical properties for Super Star, Rx 91, and W-1 Pd–Ag dental alloys provided by manufacturers (after heat treatment for porcelain application).....	121
6.2 Fatigue cycles to failure for Super Star, Rx 91, and W-1.....	122
7.1 Mechanical properties reported by manufacturer (simulated heat treatment for porcelain application).....	145
7.2 Vickers hardness (VHN) for copings and fatigue test specimens.....	145
7.3 Statistical comparisons between as-cast and heat treated coping specimens using two-way ANOVA.....	146
7.4 Statistical comparisons between heat-treated coping specimens and fatigue test specimens by using two-way ANOVA.....	146
7.5 Number of cycles to failure for IS 64 and d.SIGN 59 specimens tested at different stress amplitudes.....	147

## LIST OF FIGURES

<u>Figure</u>	<u>Page</u>
1.1 Pd–Ga phase diagram.....	33
1.2 Pd–Ag phase diagram.....	33
1.3 Pd–Sn phase diagram.....	34
1.4 Pd–In phase diagram.....	34
1.5 Ag–Sn phase diagram.....	35
1.6 Ag–In phase diagram.....	35
1.7 TEM dark-field micrograph of heat-treated Pd–Ag alloy Super Star, showing discontinuous fct precipitates.....	36
1.8 TEM dark-field micrograph showing interfacial dislocations formed by the misfit of the fct precipitate phase containing nanoscale striations and the fcc palladium solid solution matrix in heat-treated Pd–Ag alloy Super Star.....	36
2.1 Porosity in the longitudinally sectioned fractured specimens: (a) optical low- magnification micrograph showing evenly distribution pores in heat-treated Aries (scale bar length = 400 $\mu\text{m}$ ); (b) SEM micrograph showing the morphology of the pores in heat-treated d.SIGN 59 (scale bar length = 50 $\mu\text{m}$ ).....	50
2.2 Scanning electron micrographs showing the as-cast microstructure of (a) Aries. Bar = 30 $\mu\text{m}$ ; (b) IS 64. Bar = 10 $\mu\text{m}$ ; (c) d.SIGN 59 specimen with the lowest yield strength in the group (Specimen No. 9 in Table 2.4). Bar = 15 $\mu\text{m}$ ; (d) d.SIGN 59 specimen with highest yield strength (Specimen No. 10 in Table 2.4). Bar = 10 $\mu\text{m}$ .....	51

<u>Figure</u>	<u>Page</u>
2.3 Scanning electron micrographs showing microstructures of specimens after simulated porcelain-firing heat treatment: (a) Aries. Bar = 10 $\mu\text{m}$ ; (b) d.SIGN 59. Bar = 5 $\mu\text{m}$ ; (c) longitudinally sectioned d.SIGN 59. Bar = 20 $\mu\text{m}$ . Specimens (a) and (b) were sectioned perpendicularly to the axis of the tensile test specimen.....	53
2.4 Scanning electron micrographs of fractured surfaces showing: (a) dimples and embedded platelets in as-cast d.SIGN 59. Bar = 10 $\mu\text{m}$ ; (b) porosity and embedded platelets in heat-treated d.SIGN 59. Bar = 10 $\mu\text{m}$ .....	55
3.1 Variation of Vickers hardness after each step in the entire simulated porcelain-firing process. AC: as-cast; OXD: oxidation; OP1: opaque I; OP2: opaque II; BD1: body I; BD2: body II; GZ1: glazing I; GZ2: glazing II.....	68
3.2 Vickers hardness as a function of annealing temperature for Aries, IS 64, and d.SIGN 59.....	69
3.3 SEM micrographs showing the microstructures after different steps in the porcelain firing simulation process: (a) Aries after initial oxidation (length of scale bar = 10 $\mu\text{m}$ ); (b) IS 64 after initial oxidation (length of scale bar = 10 $\mu\text{m}$ ); (c) Aries after body I (length of scale bar = 10 $\mu\text{m}$ ); (d) d.SIGN 59 after glazing I (length of scale bar = 5 $\mu\text{m}$ ).....	70
3.4 SEM micrographs showing the microstructures annealed at different temperatures: (a) Aries at 700 $^{\circ}\text{C}$ (length of scale bar = 15 $\mu\text{m}$ ); (b) back scattering image of (a) (length of scale bar = 15 $\mu\text{m}$ ); (c) IS 64 at 800 $^{\circ}\text{C}$ (length of scale bar = 10 $\mu\text{m}$ ); (d) IS 64 at 900 $^{\circ}\text{C}$ (length of scale bar = 10 $\mu\text{m}$ ); (e) d.SIGN 59 at 650 $^{\circ}\text{C}$ (length of scale bar = 15 $\mu\text{m}$ ); (f) d.SIGN 59 at 900 $^{\circ}\text{C}$ (length of scale bar = 15 $\mu\text{m}$ ).....	72
4.1 Vickers hardness as function of annealing temperature for (a) W-1, (b) Rx 91, and (c) Super Star.....	87
4.2 (a) SEM photomicrograph (secondary electron image) showing the dendritic structure of W-1 annealed at 922 $^{\circ}\text{C}$ . (b) Higher-magnification photomicrograph of an interdendritic region, showing a multi-phase structure. Length of scale bar = 150 $\mu\text{m}$ for (a), and 5 $\mu\text{m}$ for (b).....	89

<u>Figure</u>	<u>Page</u>
4.3	Secondary electron images of Rx 91: (a) Annealed at 409°C, showing equiaxed grains with substructure, grain boundary precipitates, and casting porosity. (b) Annealed at 652°C, showing fine-scale porosity and precipitates in matrix and grain boundaries. (c) Annealed at 947°C, showing discontinuous precipitates in grain boundaries and adjacent matrix regions denuded of precipitates. (d) Higher- magnification photomicrograph of cube-shaped precipitates in matrix. Length of scale bar = 15 μm for (a), 5 μm for (b) and (c), and 3 μm for (d).....90
4.4	SEM photomicrographs of Super Star annealed at 417°C, showing highly segregated microstructures: (a) secondary electron image; (b) backscattered electron image. Length of scale bar = 30 μm.....92
4.5	SEM photomicrographs of Super Star annealed at 512°C: (a) secondary electron image; (b) backscattered electron image. Some redistribution of component elements has taken place, compared to the Figure 4.4. Length of scale bar = 30 μm.....93
4.6	SEM photomicrographs of Super Star annealed at higher temperatures: (a) 561°C; (b) 662°C; (c) 947°C. Needle-like precipitates and discontinuous precipitates appeared after annealing at 947°C. Length of scale bar = 30 μm for (a), 10 μm for (b), and 15 μm for (c).....94
5.1	TEM micrographs of as-cast Rx 91: (a) granular precipitates (length of scale bar = 200 nm); (b) fine-scale fct precipitates (length of scale bar = 50 nm); (c) dark-field image showing striations in grain boundary fct phase (length of scale bar = 100 nm).....104
5.2	TEM micrographs in simulated porcelain firing heat-treated W-1: (a) granular precipitates with different sizes (length of scale bar = 200 nm); (b) dislocations inside granular precipitates (length of scale bar = 500 nm).....106
5.3	TEM micrograph and electron diffraction patterns showing cubic-cubic orientation between the matrix and the granular precipitate phase in Rx 91 after annealing at 947°C: (a) dark-field image of the granular precipitates (length of scale bar = 200 nm); (b) selected-area electron diffraction pattern (SADP) of palladium solid solution matrix, <b>B</b> = [100]; (c) Convergent-beam electron diffraction pattern of a granular precipitate with the same condition as in (b). <b>B</b> = [100].....107

<u>Figure</u>	<u>Page</u>	
5.4	TEM micrographs showing the microstructures in Super Star after annealing at different temperatures: (a) elliptical precipitates after annealing at 512°C (length of scale bar = 200 nm); (b) ordered precipitates after annealing at 662°C (length of scale bar = 100 nm); (c) fine-scale fct precipitates in grains after annealing at 947°C (length of scale bar = 100 nm); (d) fct phase in grain boundary region after annealing at 947°C (length of scale bar = 200 nm).....	109
6.1	SEM images of heat-treated (a) Super Star (scale bar length = 50 μm), (b) Rx 91 (scale bar length = 4 μm), and (c) W-1 (scale bar length = 300 μm). (a) is a backscattered electron image, and (b) and (c) are secondary electron images. The as-cast dendritic character of W-1 is maintained after the porcelain-firing heat treatment. The inhomogeneous compositions of the equiaxed regions with dendritic character in Super Star are evident in the backscattered electron image. The higher-magnification photomicrograph of Rx 91 shows the discontinuous grain boundary precipitates and the etching pattern within grains.....	123
6.2	Secondary electron SEM image showing the incomplete solidification (dendritic structure) around the fatigue crack initiation region on the fracture surface of one Super Star alloy specimen, which failed after 1,516,640 cycles at 0.15σ <sub>0.2</sub> (scale bar length = 10 μm).....	125
6.3	Secondary electron SEM images of fatigue fracture surfaces for (a) Super Star, 1,516,640 cycles at 0.15σ <sub>0.2</sub> (scale bar length = 20 μm), (b) Rx 91, 1,226,010 cycles at 0.15σ <sub>0.2</sub> (scale bar length = 10 μm), and (c) W-1, 907,330 cycles at 0.20σ <sub>0.2</sub> (scale bar length = 10 μm), showing typical fatigue striations in the alloys.....	126
6.4	Secondary electron SEM images of the fatigue fracture surfaces for (a) Super Star, 715,875 cycles at 0.20σ <sub>0.2</sub> (scale bar length = 1 μm) and (b) W-1, 659,555 cycles at 0.15σ <sub>0.2</sub> (scale bar length = 5 μm), showing terraced patterns of striations.....	128
6.5	TEM bright-field image of tangled dislocations and stress-induced slip bands in fatigued W-1, 183,210 cycles at 0.20σ <sub>0.2</sub> (scale bar length = 200 nm).....	129
6.6	TEM bright-field image showing interphase boundary dislocations between the spherical precipitates and the surrounding twinned matrix of fatigued Rx 91, 983,905 cycles at 0.15σ <sub>0.2</sub> (scale bar length = 200 nm).....	130

<u>Figure</u>	<u>Page</u>
6.7	TEM dark-field image showing twinning inside discontinuous precipitates due to fatigue deformation in Rx 91, 983,905 cycles at $0.15\sigma_{0.2}$ (scale bar length = 50 nm).....131
7.1	SEM images showing the microstructures of (a) as-cast and (b) heat-treated IS 64 coping specimens, and (c) as-cast and (d) heat-treated d.SIGN 59 coping specimens. Length of scale bar = 15 $\mu\text{m}$ for (a), and 10 $\mu\text{m}$ for (b), (c) and (d).....148
7.2	SEM images showing the incompletely homogenized microstructures in fatigue test specimens after simulated porcelain-firing heat treatment for (a) IS 64 and (b) d.SIGN 59. Length of scale bar = 30 $\mu\text{m}$ for (a) and 10 $\mu\text{m}$ for (b).....150
7.3	SEM image showing casting porosity in IS 64 specimen broken at 1,651,575 cycles (length of scale bar = 1 mm).....151
7.4	Optical micrographs showing casting porosity in longitudinally cross-sectioned d.SIGN 59 specimen survived 2 million cycles. (a) and (c) were taken in regions near two opposite surfaces; (b) was taken in central region. Length of scale bar = 400 $\mu\text{m}$ .....151
7.5	SEM images showing fatigue striations on the fracture surfaces of (a) IS 64 specimen broken at 1,651,575 cycles and (b) d.SIGN 59 specimen broken at 405,874 cycles. Length of scale bar = 10 $\mu\text{m}$ for (a) and 15 $\mu\text{m}$ for (b).....153

## **CHAPTER 1**

### **INTRODUCTION AND BACKGROUND FOR STUDY**

#### **1.1 General Background of Dental Casting Alloys (Anusavice, 1996)**

Casting alloys have been widely used in dentistry to make inlays, onlays, crowns, conventional all-metal bridges, metal-ceramic bridges, resin-bonded bridges, endodontic posts, and removable partial denture frameworks. Compared to other shaping processes, certain advantages are inherent in the metal casting process, for example, dental prostheses with most intricate shapes and almost any size can be cast, and the process is simple, quick and relatively economical.

In the oral environment, it is required that all dental casting alloys be biocompatible and exhibit sufficient physical and mechanical properties to ensure adequate function and structural durability over long periods of time. The following clinically important requirements and properties should be considered: biocompatibility, corrosion resistance, tarnish resistance, presence of allergic components, aesthetics, thermal properties, melting range, compensation for solidification, strength requirements, ease of fabrication for prostheses and frameworks, castability, ease of finishing the casting, porcelain bonding (for metal-ceramic restoration), and unit material and dental laboratory costs.

The first reported application of the lost-wax casting technique in dentistry can be tracked to 1907, when Dr. William H. Taggart delivered a presentation to the New York Odontological Group on the fabrication of cast gold inlay restorations developed in 1905. This soon led to wide application of casting of inlays in the dental field. As pure gold did not have required mechanical properties, existing jewelry alloys were quickly adopted, and they were further strengthened by additions of copper, silver, or platinum.

Dental gold casting alloys were first classified as Type I (soft), Type II (medium), Type III (hard), and Type IV (extra hard) by the dental materials group at the National Bureau of Standard (currently the National Institute of Standards and Technology) in 1932. In the following years, the content of gold in gold alloys was decreased, and palladium was added to substitute for platinum and counteract the tarnish potential of silver. By 1948, the composition of dental casting noble alloys had become rather diverse.

Nickel-chromium and cobalt-chromium alloys were introduced into dentistry in the 1930s to replace the conventional Type IV gold alloys. Due to their successful application as removable partial denture frameworks, initial efforts were made to use these alloys for other types of restorations, but intensive research had not started until the rapid gold price escalation in the 1970s. After the United States abandoned the gold standard in 1971, the following areas were stimulated in developing new dental alloys: (1) In some alloys, gold was partially replaced with palladium. (2) In other alloys, gold was completely replaced by palladium. (3) Base metals with nickel as the major element were developed to replace noble metals for metal-ceramic applications.

Weinstein *et al.* (1962) demonstrated in 1959 that the thermal expansion coefficient of dental porcelain could be modified to closely match that of the casting alloy and produce thermally compatible metal-ceramic prostheses. This breakthrough made possible the successful application of metal-ceramic prostheses in dentistry. The melting temperature of the alloys should be sufficiently high to permit porcelain firing onto the alloys without deforming the metal substrate.

In the early years of the ADA Acceptance program, most dental alloy compositions were based on gold, and chemical composition was considered to be one of the most important aspects for considering a casting alloy for dental applications. Currently, several hundred brands of dental casting alloys are available on the world market. It has been found to not be practical to set up detailed standards on the basis of alloy composition. The American Dental Association (ADA) in 1984 proposed a simple classification with three categories: high noble (HN), noble (N), and predominantly base metal (PB) (Table 1.1). Many manufacturers have adopted this classification for the simplification of communication between dentists and dental laboratory technicians.

There has been a trend to establish standards using performance as the criterion for evaluating dental casting alloys. The current dental casting alloy classification system, American National Standards Institute/American Dental Association (ANSI/ADA) Specification No. 5 (1997), is divided into Type I through Type IV as shown in Table 1.2, which was originally established for gold alloys. The specification provides a classification and specifies requirements and testing methods for dental casting alloys used as dental restorations and appliances.

## **1.2 High-Palladium Dental Casting Alloys**

### **1.2.1 *Historical Background***

High-palladium dental casting alloys contain more than 75 wt. % Pd and are used for metal-ceramic restorations, all-metal restorations, implant-supported prostheses (Carr and Brantley, 1991) and potentially for removable partial denture framework (Asgar, 1988). The alloy CM Metal (78% Pd, 9% In, 7.6% Sn, 5% Co, 0.2% Si) patented by Boyajian (1981) was the precursor of this alloy group. Although CM Metal never became commercially successful, the alloy initiated research for other high-palladium alloy development (Vrijhoef and Greener, 1988). The first high-palladium casting alloy of commercial importance was based on the Pd–Cu–Ga system and patented as the Pd–Cu–Ga alloy Option by Schaffer (1983). This alloy became successful, and since then a series of alloys with compositions like Option have been marketed. However, these Pd–Cu–Ga alloys generally exhibited high hardness and yield strength, which might cause problems during finishing and polishing of restorations for dental laboratories and clinicians (Carr and Brantley, 1991). In addition, the marginal creep was questioned, as the alloys tested had relatively poor creep resistance at high stresses and temperatures close to the glass transition temperature of dental porcelain (Anusavice *et al.*, 1985). As a solution, Pd–Ga alloys with a small amount of Ag and lower hardness were subsequently introduced (Carr and Brantley, 1991) and became an important group of the high-palladium alloys.

### **1.2.2 Compositions, Microstructures and Mechanical Properties of High-Palladium Alloys**

Compositions of high-palladium dental alloys marketed by three major manufacturers in the United States are given in Table 1.3. The microstructures of high-palladium alloys can be roughly predicted from the Pd–Ga phase diagram (Okamoto, 2000) shown in Figure 1.1, even though the phase relationships in as-cast alloys can depart substantially from the equilibrium situation because of the rapid solidification rates under normal dental laboratory conditions. Due to their complex compositions, multiple phases exist in high-palladium alloys, which solidify with either dendritic microstructures or fine-grained microstructures if ruthenium is added as a grain-refining element (Carr and Brantley, 1991; Brantley *et al.*, 1993; Wu *et al.*, 1997; Brantley *et al.*, 1999; Papazoglou *et al.*, 1999; Pinasco *et al.*, 1999; Papazoglou *et al.*, 2000). In as-cast Pd–Cu–Ga alloys, a lamellar eutectic structure occurs as an interdendritic constituent or as a near-surface constituent in fine-grained alloys (Brantley *et al.*, 1993). This eutectic structure forms due to the effect of copper in shifting the binary Pd–Ga eutectic to lower gallium concentrations (Cascone, 1984) and the similar effect occurs from the rapid cooling under dental casting conditions (Anusavice, 1996), but this structure is largely absent in Pd–Ga alloys, which have grain boundary precipitates (Brantley *et al.*, 1993).

The microstructure differences between high-palladium alloys may result in large mechanical property differences, even though they have similar compositions. It has been shown (Wu *et al.*, 1997) that the two-phase eutectic structure in the as-cast fine-grained Pd–Cu–Ga alloy Liberty does not contribute to the high hardness of this alloy, which is instead due to the presence of a previously unidentified hard grain boundary phase

(Pd<sub>5</sub>Ga<sub>2</sub>). The hard phase has an approximate composition (wt. %) of 74% Pd, 11% Cu and 10% Ga, along with 1-2% Sn, Au, and Ru. The high hardness of the Option, Spartan and Spartan Plus Pd–Cu–Ga alloys is attributed to the hard phase in the interdendritic region (Brantley *et al.*, 1999).

Using transmission electron microscopy (TEM), a complex structure of thin (5–25 nm) lath-like precipitates was observed in a commercial Pd–Cu–Ga dental alloy with a composition similar to Option and Spartan (Odén and Herø, 1986). The submicron precipitate network was assumed to consist of alternating face-centered tetragonal (fct) Pd<sub>3</sub>Ga<sub>x</sub>Cu<sub>1-x</sub> phases with different *c/a* ratios for the lattice parameters. Odén and Herø proposed that the high strength and hardness of many Pd-Cu-Ga alloys resulted from the network. This mechanism seemed to account for the lower hardness of Pd–Ga alloys without copper. However, further TEM investigation (Cai *et al.*, 1997; Nitta *et al.*, 1999) indicated that this proposed strengthening mechanism was incorrect, since the same structure was observed in both Pd–Cu–Ga and Pd–Ga alloys. Cai *et al.* (1997) identified this structure in the high-palladium-alloys as a tweed structure. The tweed structure may be present in all high-palladium dental alloys, and appears in TEM as lying within bands approximately 200 nm wide. The fine-scale tweed structure lies along two <111> directions within each band (Cai *et al.*, 1997). These bands bounding the fine-scale tweed structure were subsequently proven by Nitta *et al.* (1999) to be 120° microtwins along the [111] zone axis with a (1  $\bar{1}$  0) mirror plane. Within these bands the alloy has an fct structure with (*c/a*) ratio of 1.03. The tweed structure in Legacy and Protocol was

maintained after simulated porcelain-firing heat treatment, and the amount of tweed structure in an as-cast Liberty specimen increased after five years of aging at room temperature (Cai *et al.*, 1997; Nitta *et al.*, 1999).

The strengthening mechanisms for high-palladium dental alloys are complicated. The presence of multiple solute elements in the face-centered cubic (fcc) palladium solid solution causes substantial solid solution strengthening, and additional strengthening from the dendritic structure or interdendritic constituents, or second phases such as the hard phase and the eutectic constituent in fine-grained alloys has been proposed (Brantley *et al.*, 1993; Brantley *et al.*, 1996; Wu *et al.*, 1997; Brantley *et al.*, 1999).

The mechanical properties, melting range and density of the high-palladium alloys marketed by three major US manufacturers (Table 1.3) are given in Table 1.4. The tensile properties of representative high-palladium alloys for the as-cast condition and after simulated porcelain firing cycles are given in Table 1.5 (Papazoglou *et al.*, 1999) and Table 1.6 (Papazoglou *et al.*, 2000). The two Pd–Cu–Ga alloys Spartan Plus (dendritic as-cast microstructure) and Liberty (equiaxed fine-grained as-cast microstructure) are substantially stronger than the Pd–Ga alloy Protocol (equiaxed fine-grained microstructure). After the simulated porcelain-firing heat treatment, significant changes occur in the yield strength and percentage elongation for Spartan Plus, but not for Protocol (Table 1.5). All three Pd–Cu–Ga alloys with dendritic as-cast microstructures are responsive to the simulated porcelain-firing heat treatment, which is considered (Brantley *et al.*, 1993; Carr *et al.*, 1993) to eliminate the original as-cast microstructure; significant decreases occur in yield strength and significant increases occur in percentage elongation (Table 1.6). These changes in mechanical properties are

related to transformation of the grain boundary hard phase found in Pd–Cu–Ga alloys, while this phase is absent in the Pd–Ga alloys (Wu *et al.*, 1997; Brantley *et al.*, 1999). In all of these high-palladium alloys, there is no significant difference in the modulus of elasticity (Papazoglou *et al.*, 1999; Papazoglou *et al.*, 2000), indicating its general structure-insensitivity. The similar values of strain-hardening exponent suggest similar dislocation processes for plastic deformation of these alloys, while the different values of the strength coefficient may suggest different types of dislocation obstacles.

It is interesting that substantial microstructural changes were observed in three as-cast Pd–Cu–Ga alloys, Athenium, Liberty and Spartan Plus, after five years of storage (aging) at room temperature (Brantley *et al.*, 1995). Castings of both Athenium and Liberty had a near surface zone approximately 20  $\mu\text{m}$  in depth that was denuded of the eutectic constituent that had extended to the air-abraded surface in specimen before aging. The aged Spartan Plus castings retained a dendritic microstructure, but there was evidence of considerable phase transformation in the interdendritic regions.

Dental laboratory technique-sensitivity for the high-palladium alloys was observed when preparing cast tensile test specimens, which are much larger than single-tooth restorations. Although there was no significant porosity (<1%) difference in Spartan Plus, Liberty and Protocol, porosity was a significant factor for the ultimate tensile strength of Liberty and Protocol, but not Spartan Plus (Papazoglou *et al.*, 2000). The much larger tensile test specimens of as-cast Liberty did not contain the near-surface eutectic constituent that was abundant in thin-walled specimens simulating maxillary central incisor copings (Carr and Brantley, 1991; Brantley *et al.*, 1993). In addition, the as-cast dendritic microstructure in the large Spartan Plus tensile test specimens was not

fully eliminated by porcelain-firing simulating heat treatment (Li *et al.*, 2002). These examples illustrate the importance of laboratory technique and casting thickness on the as-cast microstructure of high-palladium alloys.

The fatigue properties of the Pd–Cu–Ga alloy Spartan Plus with a dendritic as-cast microstructure and the Pd–Ga alloy Protocol with an equiaxed fine-grained as-cast microstructure were studied, and the results are presented in Tables 1.7 and 1.8 (Li *et al.*, 2002). After simulated porcelain-firing heat treatment, the fatigue limits ( $2 \times 10^6$  cycles, using cyclic tension-compression loading at 10 Hz with a stress ratio of -1) for all-new metal Spartan Plus and Protocol were approximately 0.20 and 0.15 of the 0.1% yield strength for each alloy, respectively. The fatigue resistance of Spartan Plus and Protocol specimens containing 50% old metal (previously melted one time) and 50% new metal was comparable to that of specimens containing all new metal. However, the fatigue resistance of Spartan Plus with all metal previously melted one time decreased dramatically, and in order to maintain adequate fatigue resistance, it was suggested at least 50% percent new metal be added when remelting scrap metal of Spartan Plus that was previously melted one time.

### ***1.2.3 Microstructures of Plastically Deformed and Fatigued High-Palladium Alloys Observed with TEM***

The microstructures of permanently deformed Liberty and Protocol alloys were investigated using TEM (Guo *et al.*, 2003a). Both alloys exhibited the same characteristic tweed structure. Dislocations were only observed in the highly ductile fcc palladium solid solution matrix of the two alloys and in the body-centered cubic (bcc) precipitates of Liberty. This bcc phase was not previously detected in undeformed as-cast and heat-

treated high-palladium alloys (Cai *et al.*, 1997; Nitta *et al.*, 1999). In deformed Liberty, the bcc phase was only found in some grains and always appeared in the grain boundaries of the palladium solid solution matrix and the tweed bands. Energy-dispersive spectrometric (EDS) analysis showed that this phase contained a significantly higher concentration of copper and lower concentration of tin than the palladium solid solution. Fine-scale precipitates several nanometers in dimensions were observed in some (but not all) palladium solid solution matrix grains of deformed Protocol, and compared to the matrix, the precipitates were highly Ru-enriched and correspondingly lower in palladium content. In addition, particles of almost pure Ru, used as a grain-refining element in high-palladium alloys, were found in the palladium solid solution matrix of both deformed alloys.

TEM examination (Guo *et al.*, 2002) of Spartan Plus specimens after fatigue loading revealed that the principal microdeformation mode during fatigue was twinning in the palladium solid solution matrix, and the twin interactions were similar to those observed for deformed Liberty. In Protocol TEM examination showed that the dominant microdeformation mode was planar slip. Because of the higher fatigue limit of Spartan Plus than Protocol, the twinning mechanism within its palladium solid solution matrix appeared to enhance the fatigue behavior of Spartan Plus. In contrast, the planar slip in Protocol and the resulting accumulation of microdeformation during fatigue might provide not only crack initiation sites and decrease the fatigue limit, but also cause some cyclic hardening. Precipitates were present throughout the palladium solid solution matrix of Protocol. These precipitates were apparently induced by the fatigue loading, whereas such precipitates occurred only in some grains when this alloys was deformed in

tension (Guo *et al.*, 2003a). With increasing number of fatigue cycles and greater stress amplitude, the precipitate size and density in Protocol appeared to increase. The characteristic tweed structure found in a previous TEM study of heat-treated Protocol (Cai *et al.*, 1997), in which the starting castings simulated maxillary incisor copings, was not observed in the much larger fatigued specimens.

#### ***1.2.4 Adherence of Porcelain to High-Palladium Alloys and Mechanisms for Surface Oxide Formation***

The adherence of porcelain to high-palladium alloys used for metal-ceramic restorations has been intensively studied by Papazoglou and colleagues (Papazoglou *et al.*, 1993, and 1996; Papazoglou and Brantley, 1998). Early evaluation of the adherence was reported as the area fraction of porcelain remaining on the alloy, and the adherence of Vita VMK porcelain (Vident, Baldwin Park, CA) to Pd–Cu–Ga alloys was superior compared to Pd–Ga alloys (Papazoglou *et al.*, 1993). The relative porcelain adherence to the alloys was correlated to the complex interaction zones between porcelain and the alloys (Papazoglou *et al.*, 1996). For example, the minimal adherence of the porcelain to Legacy was due to complex interfacial reactions of Ga<sub>2</sub>O<sub>3</sub> and possibly palladium oxide with the porcelain, resulting in formation of island-like regions that fractured readily during loading. Later the bond failure force was found not to correlate with porcelain adherence (Papazoglou and Brantley, 1998). In this study, the use of two different methods for assessing the metal-ceramic bond provided useful information on the relationship of data obtained by different experimental techniques.

After the oxidation process recommended by manufactures, the oxides formed and the corresponding effects on porcelain adherence is complex. X-ray diffraction studies of high-palladium alloys after conventional air-abrasion of the cast alloy surface and oxidation following the recommendation of the manufacturer showed that  $\text{CuGa}_2\text{O}_4$  and  $\text{SnO}_2$  were the major oxides on the oxidized Pd-Cu-Ga alloys Spartan Plus and Liberty, respectively, whereas  $\beta\text{-Ga}_2\text{O}_3$  was the major oxide on the oxidized Pd-Ga alloys Legacy and Protocol (Brantley *et al.*, 1996). In contrast, when the as-cast alloy was metallographically polished, only  $\text{In}_2\text{O}_3$  formed on the surface of oxidized Legacy and a mixture of  $\text{In}_2\text{O}_3$  and  $\beta\text{-Ga}_2\text{O}_3$  formed on the surface of oxidized Protocol. The oxidation mechanisms were determined using x-ray photoelectron spectroscopy (XPS) and angle-resolved x-ray diffraction (ARXRD). For Pd-Ga alloys, oxide layer growth was via oxygen diffusion through the scale (oxide layer) to the metal, causing the scale to grow at the metal-oxide interface. For Pd-Cu-Ga alloys, the oxide layer formed by metal ions diffusing through the scale to the surface and reacting with oxygen, causing the scale to grow at the oxygen-air interface (Kerber *et al.*, 1998). These opposing mechanisms were correlated to the adhesion of the oxide layer when the metal-ceramic bond was evaluated by the porcelain adherence test (Papazoglou *et al.*, 1993 and 1996). Several clinically important variables, such as casting remelted alloys, stripping the initially fired porcelain and bonding new porcelain to a re-prepared surface, and the use of a saliva-substitute test medium, had significant effects on porcelain adherence to high-palladium alloys (Papazoglou *et al.*, 1998).

### **1.2.5 Corrosion and Biocompatibility of High-Palladium Dental Alloys**

Biocompatibility is top priority among all dental materials properties for all manufacturers, patients and dentists. Pure palladium was believed to be nontoxic from previous local and systemic toxicity evaluations (Murdoch and Pepys, 1986; Bessing and Kallus, 1987), but contact dermatitis from palladium was observed as frequently occurring with other sensitizers, especially nickel (Van Loon *et al.*, 1984; Van Joost *et al.*, 1990; Hackle *et al.*, 1991). Several cases of health problems, mainly allergic contact dermatitis, have been reported as probably related to application of palladium alloys in dentistry (Cai *et al.*, 1995; Wataha *et al.*, 1995; Wataha and Hanks, 1996). However, it was concluded in comprehensive reviews on the biocompatibility of high-palladium alloys (Cai *et al.*, 1995; Wataha and Hanks, 1996) that the risk of using high-palladium dental alloys was extremely low due to the low dissolution rate of palladium ions from these alloys.

The biocompatibility of the high-palladium alloys is largely dependent on the biological activity of alloy corrosion resistance and corrosion products. Many studies on high-palladium alloys have shown that heat treatment, microstructures and compositions did not affect corrosion behavior (Mezger *et al.*, 1989a; Böning *et al.*, 1990). Recent research has also shown that *in vitro* corrosion of representative high-palladium alloys in the as-cast and simulated porcelain-firing heat-treated conditions is essentially equivalent (Cai *et al.*, 1999; Sun, 2004). The reason may be related to the very low palladium ion release from the alloys (Tufekci *et al.*, 2002).

The corrosion properties of high-palladium dental alloys have been studied extensively. In simulated body fluids and the oral environment, the corrosion resistance of high-palladium alloys is excellent and comparable to those of the gold-based alloys (Mezger *et al.*, 1985; Meyer and Reclaru, 1995; Cai *et al.*, 1999; Sun *et al.*, 2002a, 2002b, and 2002c).

The excellent corrosion resistance of the high-palladium alloys has been attributed to their passivity and inherent nobility of palladium (Cai *et al.*, 1999, Sun, 2004). Both Pd–Cu–Ga and Pd–Ga alloys, either as-cast or after simulated porcelain-firing cycles, exhibited spontaneous passive behavior for *in vitro* conditions (Cai *et al.*, 1999, Sun, 2004). Atomic absorption spectroscopy and XPS revealed that a palladium-enriched surface formed due to selective dissolution of Co and Cu in binary Pd–Co and Pd–Cu alloys (Goehlich and Marek, 1990). The selective dissolution of Cu and Ag in commercial high-palladium alloys was observed for the heat-treated condition but not the as-cast condition (Berzins *et al.*, 1999). It was shown that the *in vitro* corrosion differs considerably for silver-containing and silver-free high-palladium alloys, and the formation of silver-enriched surfaces and palladium-enriched surfaces, respectively, for these two types of alloys, has important implications for their biocompatibility (Berzins *et al.*, 2000a, 2000b; Sarkar *et al.*, 2000). The Pd-enriched surfaces can readily release allergic Pd<sup>2+</sup> ions into the oral environment, whereas the Ag-enriched surfaces may form insoluble AgCl surface films that minimize further release of elements *in vivo*.

The amounts of the elements released from high-palladium dental alloys into *in vitro* test media or cell culture media have been extensively studied (Craig and Hanks, 1990; Goehlich and Marek, 1990; Wataha *et al.* 1991; Tufekci *et al.*, 2002). Among the

29 alloys investigated by Craig and Hanks (1990), the *in vitro* cytotoxicity of high-palladium alloys was observed to be the least for the alloy types studied. Palladium was believed to be more effective in maintaining the biocompatibility of alloys containing Cu than was Au. After immersion in cell culture medium for 72 hours, release of Au, In and Pd ions from 10 dental casting alloys were not detected using the flame atomic absorption method, but the release of other elements such as Ag, Cd, Cu, Ga, Ni and Zn was detected (Wataha *et al.*, 1991). The relationship between the released element concentrations and microstructures was found to be complicated. It is interesting that in a study by Syverud *et al.* (2001) the combinations of  $\text{Cu}^{2+}$  and  $\text{Pd}^{2+}$  ions with a  $\text{Cu}^{2+}$  to  $\text{Pd}^{2+}$  ratio of 1:2 showed most severe cytotoxicity.

The difference in elemental release from one Pd–Cu–Ga alloy and one Pd–Ga alloy into an aqueous lactic acid/NaCl solution for up to 700 hours was found to be significantly different (Tufekci *et al.*, 2002), as shown in Table 1.9. The relative proportions of the released elements in the solutions were consistent with release of palladium and breakdown of microstructural phases found in the alloys. It was thus suggested that the Pd–Ga alloys would have less potential for palladium sensitivity than Pd–Cu–Ga alloys.

Syverud *et al.* (2001) also found that the oxide layer that formed during simulated porcelain-firing heat-treatment on a Pd–Cu–Ga alloy and a Pd–Ga alloy increased the release of Cu, Ga and Pd ions. In a recent study, Sun (2004) found that although removal of the oxide layer before the simulated porcelain-firing cycles reduced the release of elements in the alloy compositions, the differences in the amounts of released elements showed no significant effects on the proliferation and viability *in vitro* of human gingival

fibroblasts. Cell proliferation in cell culture medium containing extracts from one high-palladium and one palladium–silver alloy was dependent on the cell lines, and the differences in the eluted elements and their concentrations caused no significant differences in the proliferation and viability of the fibroblasts. In addition, in an animal model of evaluating the biocompatibility of the two alloys for four weeks, no abnormal tissue morphology was found, indicating that there is no biocompatibility concern for the alloys in the mice.

### **1.3 Palladium–Silver Dental Casting Alloys**

#### **1.3.1 Background**

Palladium–silver (Pd–Ag) dental casting alloys usually contain 50% to 60% Pd and 30% to 40% Ag (wt. %), with the balance as small amounts of low melting point metals, In, Sn and Zn. These alloys have high elastic modulus, high sag resistance during the porcelain firing cycles, excellent porcelain-metal bond strength, and favorable handling and soldering characteristics (Huget and Civjan, 1974; Walton and O'Brien, 1985; Goodacre, 1989; Papazoglou *et al.*, 1998; Bertolotti, 2002). Since their introduction in the early 1970s, these alloys have achieved widespread clinical popularity due to their economic advantage compared to gold and high-palladium alloys. These alloys are used for metal-ceramic restorations and the superstructures of dental implants. The first Pd–Ag dental alloy was Cameo-Lite (J.F. Jelenko & Co., Armonk, NY), marketed in 1973, and Will-Ceram W-1 was the first patented Pd–Ag dental alloy in 1974 (Goodacre, 1989).

During the early application of palladium–silver alloys in metal–ceramic restorations, porcelain discoloration was reported and varied among different brands of dental porcelain (Huget and Civjan, 1974; Bertolotti, 1984; Bertolotti, 1988; Goodacre, 1989). This problem has been alleviated or eliminated by proper alloy melting and casting, and selection of particular porcelain brands (Lacy *et al.*, 1977; Bertolotti, 1984; Bertolotti, 1988; Goodacre, 1989; Brantley and Laub, 200; Bertolotti, 2002). Other approaches have also been used to prevent porcelain discoloration, including use of coating agents and incorporation of certain elements in the alloy composition (Ringle *et al.*, 1986; Bertolotti, 1988; O’Brien *et al.*, 1998). In the molten state, palladium–silver alloys readily occlude and interact with atmospheric gases, which may result in porosity in the castings (Huget, 1974), since the solubility of these gases is much lower in the solidified alloy. Therefore, successful fabrication of Pd–Ag alloy castings requires strict adherence to dental laboratory procedures, including a well-designed sprue arrangement and proper selection of investment.

In recent years, there has been renewed interest in palladium–silver alloys for metal–ceramic restorations because of the palladium price volatility. Currently (March 2006), approximate prices per Troy ounce are \$540 for gold, \$290 for palladium, and \$10 for silver.

### ***1.3.2 Compositions, Microstructures and Mechanical Properties of Palladium–Silver Alloys***

The compositions of some commercial palladium–silver dental alloys manufactured by three major manufacturers in the United States are shown in Table 1.10. Palladium and silver are completely soluble with each other in the solid state and form a

continuous series of solid solution without phase transformation, as shown in the Pd–Ag binary alloy diagram in Figure 1.2 (Okamoto, 2000). The addition of minor low-melting temperature base metals, such as In, Sn, or Zn, by the alloy manufacturer is done to increase the fluidity of the molten alloys and thus improve their castability. In and Sn form intermetallic compounds with both palladium and silver, as shown in Figures 1.3 – 1.6 (Okamoto, 2000), which contribute to age hardening.

Due to rapid solidification during dental casting, microsegregation and various other microstructural features or phases generally exist in Pd–Ag dental alloys. In the as-cast condition, palladium–silver alloys exhibit heterogeneous microstructures or multiple phases. After porcelain-firing, simulated porcelain-firing heat treatment, or annealing heat treatment, the alloy microstructures change considerably, and age hardening or softening have been observed (Huget *et al.*, 1976; Payan *et al.*, 1986; Mezger *et al.*, 1989b; Hisatsune *et al.*, 1990; Vermilyea *et al.*, 1996; Pinasco *et al.*, 1999; Guo *et al.*, 2003b). During the initial oxidation procedure before porcelain firing, Pd–Ag nodules were observed on the surface of the Pd–Ag dental alloy W-1 (Ivoclar Vivadent, Amherst, NY) due to internal oxidation of Sn and In (Mackert *et al.*, 1983). When annealing between 400° and 1000°C, the hardness variation with a peak at 650°C in an experimental 59.3Pd–29.6Ag–8.8Sn–2.2In alloy was attributed to such internal oxidation (Payan *et al.*, 1986).

In a study on five commercial Pd–Ag alloys, three alloys without In and Zn were considered to consist of principally a single-phase fcc structure, and other microstructural features could be observed. For the other two alloys that contained In, additional peaks were observed, but could not be indexed (Mezger *et al.*, 1989b). Another study on one

Pd–Ag–Sn–In alloy (Pinasco *et al.*, 1999) confirmed by x-ray diffraction that the as-cast microstructure with segregation and interdendritic microstructural features appeared to consist of only a single phase; there was insufficient amount of the other phases for detection. Compared to the complex tweed microstructures of high-palladium alloys at the nanometer level, the microstructures of palladium–silver alloys are relatively simple.

The mechanism involved in the age hardening (prolonged up to  $10^5$  minutes) of a 55Pd–36Ag–5Sn–4In alloy (wt. %, Byron, Nippon Shiken Dental Co., Ltd., Tokyo, Japan), was thoroughly characterized by Hisatsune *et al.* (1990), using hardness tests, x-ray diffraction, scanning electron microscopy, and transmission electron microscopy. It was found that in the early stages of aging, a metastable ordered phase ( $\beta'$ ) with an fct structure based on Pd<sub>3</sub>In was formed within the grains, and the hardening was due to the coherency strain between the metastable fct structure and the fcc matrix. In the later aging stages, a lamellar structure, consisting of a stable ordered fct phase ( $\beta$ ) based on Pd<sub>3</sub>In and a stable fcc phase, grew from the grain boundaries. These lamellae finally covered the whole grain and resulted in softening. This  $\beta$  tetragonal phase was also identified by x-ray diffraction in the Pd – Ag alloy Gamma Cast (57.9Pd–29.7Ag–5.4Sn–3.7In, Puppo Iori, Genoa, Italy) by Pinasco *et al.*, 1999. These authors did not determine whether the  $\beta$  phase was ordered. Despite various microstructural features present in their photomicrographs, the authors stated that the alloy microstructure consisted of only two phases: the fcc matrix and a  $\beta$  fct phase with a variable composition within certain limits.

In a recent study by Guo *et al.* (2003b), the microstructures of as-cast and simulated porcelain-firing heat-treated Pd – Ag–In–Sn alloy Super Star (Heraeus Kulzer Jelenko, Armonk, NY) were investigated using TEM. Two distinct phases were observed

in the as-cast microstructure: the fcc Pd solid solution matrix and fct precipitates found both in a eutectic structure (with the fcc phase) and as precipitates in the matrix. After simulated porcelain-firing heat treatment, the as-cast microstructure with considerable microsegregation became uniform, and discontinuous fct precipitates appeared in the matrix (Figure 1.7). The presence of multiple electron diffraction spot patterns from the fct phase confirmed the ordered structure of the phase observed by Hisatsune *et al.* (1990). In addition, interfacial dislocations formed by the misfit of the fct precipitate phase and the fcc matrix (Figure 1.8) were observed in the alloy, which is consistent with the hardening mechanism of coherency strain proposed by Hisatsune *et al.* (1990).

The mechanical properties, melting range and density that are provided by three major US manufacturers for representative commercial Pd–Ag alloys (compositions given in Table 1.10) are summarized in Table 1.11.

Although Pd–Ag alloys have been widely used in dentistry for many years, the mechanical property data, especially fatigue data, are very scarce in the literature.

### **1.3.3 Corrosion and Biocompatibility of Palladium–Silver Dental Alloys**

In the oral environment, pure silver corrodes in saliva, which can cause localized tissue response or systemic side effects (Braemer, 2001; Geurtsen, 2002). For palladium–silver dental alloys, there is generally more than 20 wt. % of Ag, with the amounts of each base metal (Cu, Ga, In and Sn) less than 10 wt. %. Consequently, dealloying could be a major corrosion mechanism in palladium-based dental alloys (Sarkar *et al.*, 2000; Sun *et al.*, 2002a) due to the difference in corrosion potentials among these elements.

In a series of Pd–Ag binary model alloys, the palladium ennobling effect and passivation behavior was observed in Ringer’s solution. Tarnish occurred on several alloys and pure silver, and the attack was identified as initiating from grain boundaries and propagating into grains (Vaidynathan and Prasad, 1981). The Ag/AgCl reaction was considered to increase the anodic oxidation process, which was proposed later as the mechanism for blocking the palladium allergy (Berzins *et al.*, 2000b; Sarkar *et al.*, 2000). It was suggested that the biocompatibility of palladium–silver alloys could be better than high-palladium alloys, since the palladium content has been reduced in the Pd–Ag alloys and the AgCl deposit on the alloy surface in the oral environment could prevent the occurrence of palladium allergy (Berzins *et al.*, 2000b; Sarkar *et al.*, 2000).

Quantitative study on the tarnish and corrosion behavior of three commercial palladium–silver alloys and the entire Pd–Ag binary system showed that the corrosion resistance of these alloys depended on their nobility, while composition, nobility, microstructure and heat treatment affected the tarnish response (O’Brien and German, 1984). The open circuit potential and corrosion current of five commercial Pd–Ag alloys were similar in 0.9% saline solution and an artificial saliva, with about the same magnitude as high-palladium alloys, while in phosphate-buffered saline solution, the Pd–Ag alloys showed lower open circuit potential than high-palladium alloys, but with similar corrosion current densities (Mezger *et al.*, 1989c). In a recent study (Sun, 2004), one representative palladium–silver alloy exhibited high corrosion resistance in simulated body fluid and oral environments, equivalent to that of a high-noble gold–palladium alloy. Passivation and dealloying were observed and the process was generally under charge transfer and charge accumulation control. The similar corrosion characteristics were

attributed to similar alloy compositions, since microstructure variation does not cause significant differences in corrosion behavior. In addition, cell culture and animal studies showed that the biocompatibility of high-palladium and palladium–silver alloys is adequate.

#### **1.4 Purpose of This Study**

As an important member in the family of noble dental alloys, palladium-based casting alloys have advantages over other noble alloys, and have become increasingly popular in dentistry. As discussed above, the microstructures and properties of high-palladium alloys have been systematically investigated, and understanding of these alloys is comprehensive. However, the microstructures and properties of the important palladium–silver alloys, are less well understood. In recent years, palladium–silver alloys have become much more attractive than high-palladium alloys due to volatility in the price of palladium. There were four broad purposes of this study as follows:

1. To characterize the microstructures of palladium–silver alloys in various conditions.
2. To study the tensile mechanical properties and fracture behavior of Pd–Ag alloys.
3. To determine the fatigue limits and study the fatigue fracture of Pd–Ag alloys.
4. To explore the effects of porosity on tensile mechanical properties and fatigue behavior of Pd–Ag alloys.

Alloy Type	Total Noble Metal Content
High Noble (HN)	Must contain $\geq 40$ wt% Au and $\geq 60$ wt% of noble metal elements (Au, Pt, Pd, Rh, Ru, Ir, Os)
Noble (N)	Must contain $\geq 25$ wt% of noble metal elements (Au, Pt, Pd, Rh, Ru, Ir, Os)
Predominantly Base Metal (PB)	Contain $< 25$ wt% of noble metal elements

Table 1.1. Alloy classification of the American Dental Association (Anusavice, 1996).

Alloy Type	Description	Yield Strength (0.2% offset)			Elongation	
		Annealed		Hardened	Annealed	Hardened
		Minimum	Maximum	Minimum	Minimum	Minimum
I	Soft	80 MPa	180 MPa	-	18%	-
II	Medium	180 MPa	240 MPa	-	12%	-
III	Hard	240 MPa	-	-	12%	-
IV	Extra-hard	300 MPa	-	450 MPa	10%	3%

Table 1.2. Mechanical property requirements in ANSI/ADA Specification No. 5 for dental casting alloys (1997)

Alloy	Pd	Cu	Ga	In	Sn	Au	Ag	Other
Option <sup>*</sup>	78.8	10	†			2.0		B, Ir
Spartan <sup>**</sup>	78.7	10	9					B, Ir < 1
Spartan Plus <sup>**</sup>	78.8	10	9					Ge, Ir < 1
Protocol <sup>**</sup>	75.2		6	6			6.5	Ru, Li < 1
IS 85 <sup>**</sup>	81.6		6	3.5	3.5	2.5	2.5	Ru, Re < 1
Freedom <sup>***</sup>	75.9	10	6.5	7				Ru < 1
Freedom Plus <sup>***</sup>	78.4	8	5	6		2		Ru < 1
Legacy <sup>***</sup>	85.2		10	1.1		2	<1	Ru < 1
Accu-Star <sup>***</sup>	75.0		6	6		6	6.5	Ru < 1

\* Dentsply Ceramco, Burlington, NJ. [<http://www.ceramco.com>]

\*\* Ivoclar Vivadent, Amherst, NY. [<http://www.ivoclarvivadent.com>]

\*\*\* Heraeus Kulzer Jelenko, Armonk, NY. [<http://www.jelenko.com>]

† amount not given by the manufacturer.

Table 1.3. Compositions (wt.%) of high-palladium dental alloys (provided by manufacturers).

Alloy	Yield Strength (MPa)	Vickers Hardness	Elastic Modulus (GPa)	Percentage Elongation (%)	Melting Range (°C)	Density (g/cm <sup>3</sup> )
Option <sup>*</sup>	1229	425	94	23	1100-1190	10.6
Spartan <sup>**</sup>	945	360	†	19	1115-1160	10.6
Spartan Plus <sup>**</sup>	795	310	†	14.6	1180-1210	10.7
Protocol <sup>**</sup>	500	235	†	34	1270-1310	11.0
IS 85 <sup>**</sup>	430	240	†	41	1165-1335	11.4
Freedom <sup>***</sup>	758	365	131	7	1120-1240	10.5
Freedom Plus <sup>***</sup>	565	265	138	30	1170-1300	10.8
Legacy <sup>***</sup>	717	285	131	25	1150-1330	10.9
Accu-Star <sup>***</sup>	517	250	131	35	1130-1340	11.0

\* Dentsply Ceramco, Burlington, NJ. [<http://www.ceramco.com>]

\*\* Ivoclar Vivadent, Amherst, NY. [<http://www.ivoclarvivadent.com>]

\*\*\* Heraeus Kulzer Jelenko, Armonk, NY. [<http://www.jelenko.com>]

0.2% YS values are given for alloys (†), whereas 0.1% YS are given for (\*).

† amount not given by the manufacturer.

Table 1.4. Properties of the alloys in Table 1.3 after simulated porcelain firing heat treatment (provided by manufacturers).

Alloy/ Condition	0.1% YS (MPa)	0.2% YS (MPa)	UTS (MPa)	Elongation (%)	Modulus of Elasticity (GPa)	Strain- Hardening Exponent	Strength Coefficient (MPa)
Spartan Plus/AC	791±29 A	851±31 A	1075±71 A	8.7±4.8 CD	133±15 A	0.14±0.03 AB	1773±271 A
Spartan Plus/HT	700±13 B	725±9 B	1002±9 AB	24.1±1.5 B	141±28 A	0.11±0.00 B	1271±16 B
Liberty/AC	822±51 A	872±45 A	1078±95 A	6.0±2.8 D	131±22 A	0.15±0.003 A	1821±193 A
Liberty/HT	673±36 B	689±35 B	902±123 BC	16.0±10.0 BC	130±16 A	0.12±0.00 AB	1202±56 BC
Protocol/AC	534±5 C	552±4 C	770±145 C	35.2±2.9 A	123±18 A	0.14±0.01 AB	1085±53 BC
Protocol/HT	532±10 C	547±8 C	824±71 C	36.2±2.8 A	123±15 A	0.12±0.00 AB	996±21 C

Note: Property values in a given column with the same Ryan-Einot-Gabriel-Welsch (REGW) letter codes are not significantly different ( $p < 0.05$ ). AC: as-cast condition; HT: after simulated porcelain firing cycles.

Table 1.5. Mechanical properties of one dendritic and two equiaxed fine-grained high-palladium alloys (Papazoglou *et al.*, 2000).

Alloy/ Condition	0.1% YS (MPa)	0.2% YS (MPa)	UTS (MPa)	$\delta$ (%)	Modulus of Elasticity (GPa)	Strain- Hardening Exponent	Strength Coefficient (MPa)
Option/ AC	817±82 C	870±60 C	1072±26 C	6.9±2.5 CD	136±21 A	0.13±0.003 AB	1699±174 B
Option/ HT	679±21 D	706±22 D	957±23 D	25.1±2.1 A	119±16 A	0.11±0.00 B	1241±36 C
Spartan/ AC	1070±64 A	1120±50 A	1259±32 A	2.7±1.0 D	131±24 A	0.18±0.06 A	2552±517 A
Spartan/ HT	954±35 B	998±27 B	1161±18 B	14.9±3.5 B	127±17 A	0.11±0.01 B	1718±45 B
Spartan Plus/AC	791±29 C	851±31 C	1075±71 C	8.7±4.8 C	133±15 A	0.14±0.03 AB	1773±271 B
Spartan Plus/HT	700±13 D	725±9 D	1002±9 D	24.1±1.5 A	141±28 A	0.11±0.00 B	1271±16 C

Note: Property values in a given column with the same Ryan-Einot-Gabriel-Welsch (REGW) letter codes are not significantly different ( $p < 0.05$ ). AC: as-cast condition; HT: after simulated porcelain firing cycles.

Table 1.6. Mechanical properties of three dendritic Pd–Cu–Ga high-palladium alloys (Papazoglou *et al.*, 1999).

No.	Alloy	Stress (Load)	Fatigue Cycles
1	Spartan Plus	0.25 $\sigma_{0.1}$ (1237 N)	68,973
2		0.25 $\sigma_{0.1}$ (1237 N)	79,687
3		0.20 $\sigma_{0.1}$ (943 N)	1,908,825
4		0.20 $\sigma_{0.1}$ (943 N)	1,719,015
5	Protocol	0.25 $\sigma_{0.1}$ (943 N)	675,250
6		0.25 $\sigma_{0.1}$ (943 N)	439,822
7		0.20 $\sigma_{0.1}$ (752 N)	729,935
8		0.20 $\sigma_{0.1}$ (752 N)	1,117,735
9		0.25 $\sigma_{0.1}$ (564 N)	> 2,000,000
10		0.25 $\sigma_{0.1}$ (564 N)	> 2,000,000

Table 1.7. Number of cycles to failure of all-new metal Spartan Plus and Protocol tested at different stress amplitudes (loads) (Li *et al.*, 2002).

No.	Alloy	Stress	Failure Cycles
1	50/50% Spartan Plus	0.20 $\sigma_{0.1}$ (943 N)	> 2,000,000
2		0.20 $\sigma_{0.1}$ (943 N)	1,371,835
3	50/50% Protocol	0.15 $\sigma_{0.1}$ (564 N)	> 2,000,000
4		0.15 $\sigma_{0.1}$ (564 N)	> 2,000,000
5	All-Old Spartan Plus	0.20 $\sigma_{0.1}$ (943 N)	357,027
6		0.20 $\sigma_{0.1}$ (943 N)	362,594
7		0.15 $\sigma_{0.1}$ (742 N)	785,865
8		0.15 $\sigma_{0.1}$ (742 N)	> 2,000,000
9		0.20 $\sigma_{0.1}$ (495 N)	> 2,000,000
10		0.20 $\sigma_{0.1}$ (495 N)	> 2,000,000

Table 1.8. Number of cycles to failure for 50/50% Spartan Plus and Protocol and all-old metal Spartan Plus tested at different stress amplitudes (loads) (Li *et al.*, 2002).

Time	Alloy	Pd	Ga	Cu	Sn	Ag	In	Ru
7 hr	Liberty	.074 ± 0.03 A	.057 ± 0.42 A	1.5 ± 1.4 A	0.06 ± 0.03 A	<0.04	<0.04 A	<0.04
	Legacy	0.50 ± 0.11 A	1 ± 0.3 A	<0.04 A	<0.04 A	<0.04	0.12 ± 0.05 A	<0.04
70 hr	Liberty	18 ± 0.8 A	15 ± 12 A	12 ± 14 A	0.036 ± 0.13 A	<0.04	0.06 ± 0.03 A	<0.04
	Legacy	2.8 ± 13 A	4.8 ± 0.8 A	0.19 ± 0.21 A	0.36 ± 0.13 A	<0.04	0.55 ± 0.08 A	<0.04
700 hr	Liberty	97 ± 3 A	16 ± 5 A	24 ± 1 A	2.6 ± 0.1 A	<0.04	0.06 ± 0.03 A	0.04
	Legacy	4.8 ± 0.8B	18 ± 9 A	0.19 ± 0.06 B	<0.04 B	<0.04	0.57 ± 0.32 A	0.04

Table 1.9. Elemental release ( $\mu\text{g}/\text{cm}^2$ ) from Liberty and Legacy into corrosion medium (Tufekci *et al.*, 2002).

Alloy	Au	Pd	Ag	Pt	Zn	Sn	In	Ga	Ir	Li	Re	Ru
<b>Aries*</b>		63.7	26.0			7.0	1.5	1.8			<1.0	<1.0
<b>d.SIGN 67*</b>	4.0	62.7	20.0			10.0	1.5	1.7	<1.0	<1.0		<1.0
<b>IS 64*</b>	2.8	59.9	26.0	1.0		7.0	1.5	1.8			<1.0	<1.0
<b>d.SIGN 59*</b>		59.2	27.9	<1.0	1.3	8.2	2.7			<1.0	<1.0	<1.0
<b>d.SIGN 53*</b>		53.8	34.9	<1.0	1.2	7.7	1.7			<1.0	<1.0	<1.0
<b>W-1*</b>		53.3	37.7			8.5	<1.0			<1.0		<1.0
<b>Capricorn 15*</b>	15.0	51.9	23.0				8.0	2.0			<1.0	<1.0
<b>Lunar**</b>		60	29.5		†	†	†	†	†			
<b>Applause**</b>		54.9	35.0		†	†			†			
<b>Acclaim Lite**</b>		50	40				†	†				†
<b>Degustar GA-2**</b>	2	52	36		†	†	†					†
<b>Jelstar***</b>		59.8	28.0			6.0	6.0				<1.0	<1.0
<b>Super Star***</b>		59.8	28.1			6.0	5.0	<1.0			<1.0	<1.0
<b>Jel-5***</b>		53.4	38.9			7.0		<1.0			<1.0	<1.0
<b>Medslit***</b>		49.5	40.3			9.0		1.0			<1.0	<1.0

\* Ivoclar Vivadent, Amherst, NY. [<http://www.ivoclarvivadent.com>]

\*\* Dentsply Ceramco, Burlington, NJ. [<http://www.ceramco.com>]

\*\*\* Heraeus Kulzer Jelenko, Armonk, NY. [<http://www.jelenko.com>]

† amount not given by the manufacturer.

Table 1.10. Compositions (wt. %) of palladium–silver dental alloys (provided by manufacturers).

<b>Alloy</b>	<b>Yield Strength (MPa)</b>	<b>Vickers Hardness</b>	<b>Percentage Elongation (%)</b>	<b>Melting Range (°C)</b>	<b>Density (g/cm<sup>3</sup>)</b>
<b>Aries<sup>*</sup></b>	415	185	46.0	1165 - 1290	10.8
<b>d.SIGN 67<sup>*</sup></b>	545	240	15.0	1150 - 1270	10.8
<b>IS 64<sup>*</sup></b>	560	230	31.0	1150 - 1280	11.2
<b>d.SIGN 59<sup>*</sup></b>	490	230	14.0	1230 - 1310	10.7
<b>d.SIGN 53<sup>*</sup></b>	545	250	13.0	1180 - 1280	10.7
<b>W-1<sup>*</sup></b>	485	240	11.0	1185 - 1270	11.1
<b>Capricorn 15<sup>*</sup></b>	490	255	21.0	1230 - 1310	11.5
<b>Lunar<sup>**</sup></b>	440	244	35	1180-1290	11.0
<b>Applause<sup>**</sup></b>	590	240	10	1180-1260	10.8
<b>Acclaim Lite<sup>**</sup></b>	635	300	10	1150-1265	10.7
<b>Degustar GA-2<sup>**</sup></b>	560	250	10	1150-1230	11.3
<b>Jelstar<sup>***</sup></b>	441	220	18	1230-1300	10.7
<b>Super Star<sup>***</sup></b>	655	285	15	1190-1320	10.7
<b>Jel-5<sup>***</sup></b>	455	220	25	1190-1300	10.9
<b>Medlist<sup>***</sup></b>	669	300	7	1150-1270	10.7

\* Ivoclar Vivadent, Amherst, NY. [<http://www.ivoclarvivadent.com>]

\*\* Dentsply Ceramco, Burlington, NJ. [<http://www.ceramco.com>]

\*\*\* Heraeus Kulzer Jelenko, Armonk, NY. [<http://www.jelenko.com>]

Table 1.11. Properties of the alloys in Table 1.10 after simulated porcelain firing heat treatment (provided by manufactures).

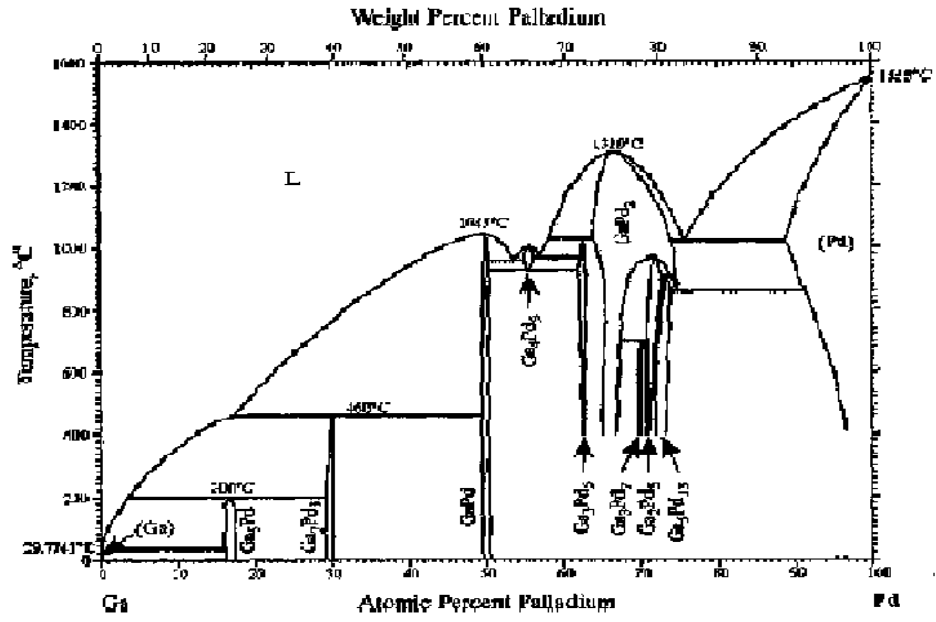


Figure 1.1. Pd-Ga phase diagram (Okamoto, 2000).

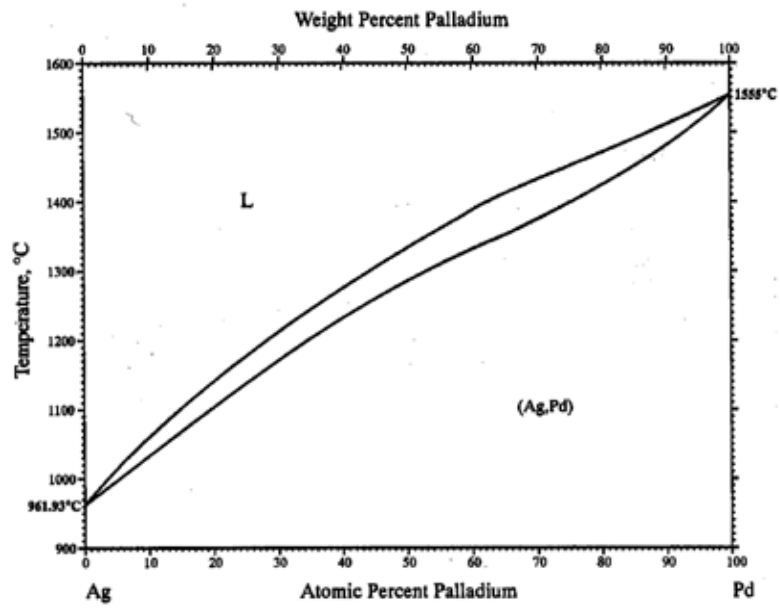


Figure 1.2. Pd-Ag phase diagram (Okamoto, 2000).

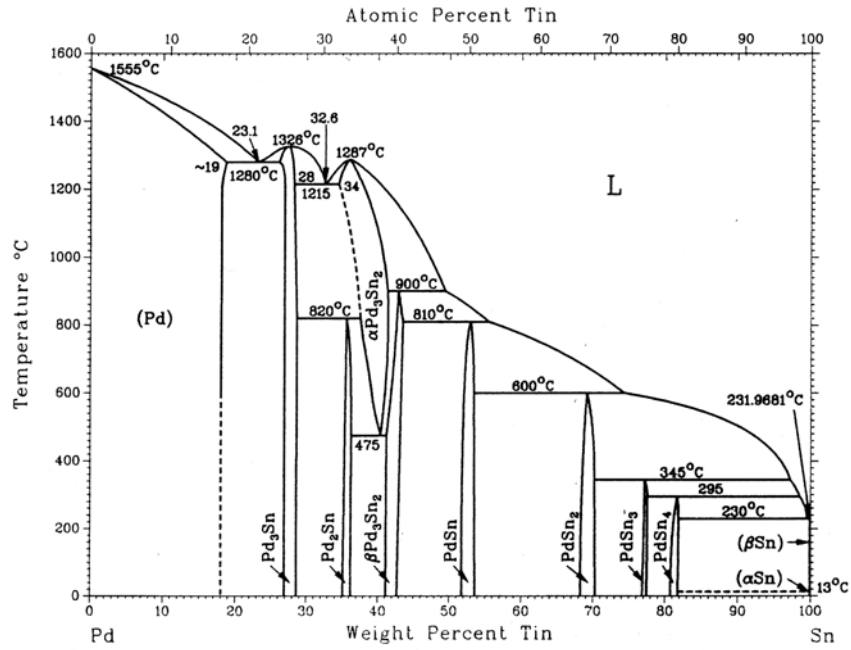


Figure 1.3. Pd-Sn phase diagram (Okamoto, 2000).

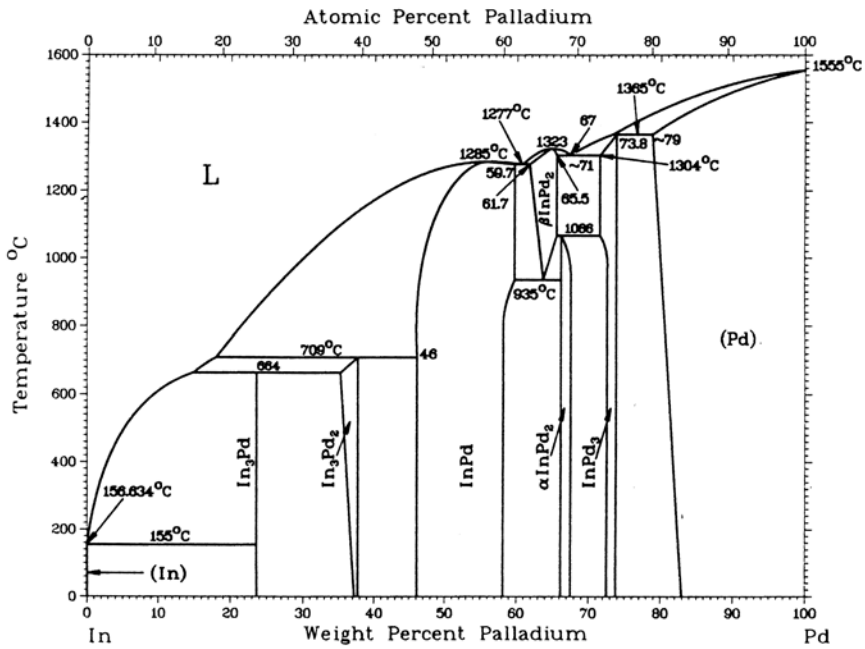


Figure 1.4. Pd-In phase diagram (Okamoto, 2000).



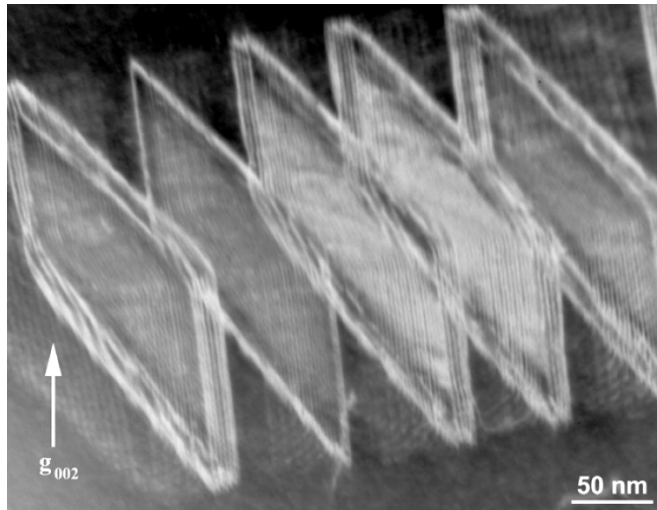


Figure 1.7. TEM dark-field micrograph of heat-treated Pd–Ag alloy Super Star, showing discontinuous fct precipitates (Guo *et al.*, 2003b).

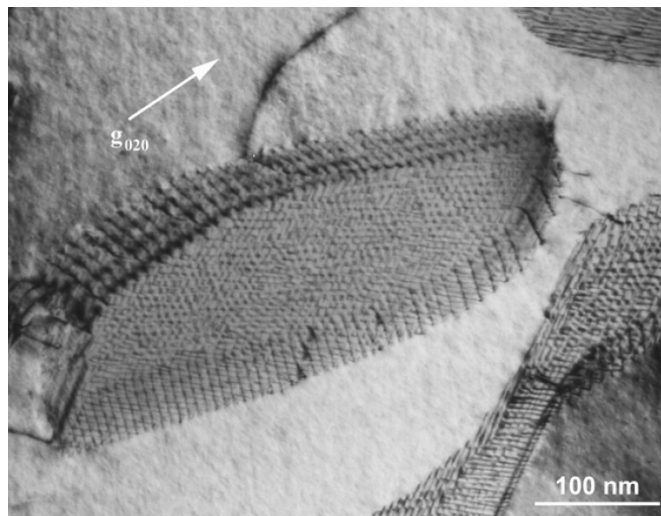


Figure 1.8. TEM dark-field micrograph showing interfacial dislocations formed by the misfit of the fct precipitate phase containing nanoscale striations and the fcc palladium solid solution matrix in heat-treated Pd–Ag alloy Super Star (Guo *et al.*, 2003b).

## CHAPTER 2

### MICROSTRUCTURES AND TENSILE PROPERTIES OF

### PALLADIUM–SILVER ALLOYS FOR METAL-CERAMIC RESTORATIONS

#### 2.1 Introduction

Since their introduction in 1973, palladium–silver (Pd–Ag) dental casting alloys, typically containing 50–60 wt. % Pd, 28–40 wt. % Ag, a small amount of lower melting point elements (Sn, and/or In and Zn) and trace elements, have been widely used for metal-ceramic restorations due to their favorable properties and satisfactory corrosion resistance (Huget *et al.*, 1976; Bertolotti, 1983; Compton *et al.*, 1985; Reel *et al.*, 1986; Mezger *et al.*, 1989c; Canay and Oktemer, 1992; Limkool and Sumii, 1995; Papazoglou and Brantley, 1998; Papazoglou *et al.*, 2001; Sun, 2004). In recent years, due to the volatility of palladium price, Pd–Ag alloys have become more attractive than high-palladium alloys for metal-ceramic restorations.

The microstructures of Pd–Ag dental casting alloys in as-cast condition and after heat treatment simulating the porcelain-firing cycles have been reported extensively in the literature (Huget *et al.*, 1976; Payan *et al.*, 1986; Mezger *et al.*, 1989b; Vermilyea *et al.*, 1996; Pinasco *et al.*, 1999; Guo *et al.*, 2003b). The as-cast microstructure was generally heterogeneous (Huget *et al.*, 1976; Payan *et al.*, 1986;

Mezger *et al.*, 1989b; Vermilyea *et al.*, 1996; Pinasco *et al.*, 1999; Guo *et al.*, 2003b). Simulated porcelain-firing heat treatment was presumably insufficient to fully homogenize the as-cast microstructure (Payan *et al.*, 1986; Mezger *et al.*, 1989b). Mezger *et al.* (1989b) examined five commercial Pd–Ag alloys in both the as-cast and simulated porcelain-firing heat-treated conditions using x-ray microanalysis and found that the alloys mainly consisted of a single phase, while two indium-containing alloys showed signs of a minor second phase which could not be identified due to its fine dispersion. Pinasco *et al.* (1999) confirmed in one Pd–Ag–Sn–In alloy using x-ray diffraction that the as-cast microstructure with segregation and interdendritic microstructural features appeared to be only single phase. In one Pd–Ag alloy Gamma Cast with a composition of 57.9Pd–29.7Ag–5.4Sn–3.7In (Puppo Iori, Genoa, Italy), Pinasco *et al.* (1999) considered that despite various microstructural features, the alloy microstructure was single-phase for the as-cast condition and contained only two phases after heat treatment: the fcc matrix and a face-centered tetragonal (fct) phase. Guo *et al.* (2003b) used the transmission electron microscope (TEM) to examine the microstructures of the Pd–Ag–In–Sn alloy Super Star (Heraeus Kulzer Jelenko, Armonk, NY), and also found two distinct phases in the as-cast microstructure: the fcc matrix and ordered fct precipitates (both in a eutectic structure and as precipitates in the matrix). After simulated porcelain-firing heat treatment, discontinuous fct precipitates also appeared in the matrix.

Although Pd–Ag alloys are popular for metal-ceramic restorations in dentistry, mechanical property data for these alloys is scarce in the literature (Huget *et al.*, 1976). The purpose of this investigation was to determine the mechanical properties of

representative Pd–Ag alloys under standard dental laboratory conditions. Additionally, the effects of heat treatment simulating porcelain-firing cycles on the mechanical properties and microstructures were also studied.

## **2.2 Materials and Methods**

Three commercial Pd–Ag alloys, Aries, IS 64 and IPS d.SIGN 59 (Ivoclar Vivadent, Amherst, NY), were selected. Nominal compositions of the alloys provided by the manufacturer are given in Table 2.1.

Following standard dental laboratory procedures and the dimensional requirements in ADA Specification Nos. 5 (1997) and 38 (2000), the alloys were melted with a multi-orifice gas-oxygen torch, centrifugally cast into tensile test bars with a gauge dimensions of 3 mm diameter  $\times$  15 mm length using a broken-arm casting machine, and bench-cooled to room temperature. Four specimens of each alloy were cast for each test condition. Specimens were divided into two groups, the as-cast group and the heat-treated group. Specimens in the heat-treated group were heat-treated simulating the entire porcelain firing cycles. The initial oxidation step followed the manufacturer instructions for each alloy, and subsequent firing cycles followed the recommendations for IPS Classic porcelain (Ivoclar Vivadent).

Tensile testing was conducted using a servohydraulic mechanical testing machine (Model 4204, Instron Corp., Canton, MA), with a crosshead speed of 2 mm/min. Test data were obtained following standard procedures. Fracture surfaces for each test

specimens were examined with a scanning electron microscope (SEM) (JSM-820, JEOL Ltd, Tokyo, Japan) to characterize the fracture and investigate the role of porosity and other casting defects for fracture.

The fractured specimens were sectioned both axially (about 3 mm from the fracture surface) and longitudinally (to about 10 mm in length), using a slow-speed water-cooled diamond saw, for microstructural and porosity observation. The sectioned specimens were mounted in metallographic epoxy resin, and polished using a standard sequence of metallographic abrasives. An optical microscope (Nikon Epiphot, Nippon Kogaku, Japan) was used to obtain low magnification porosity images. Image analysis was carried out on specimens with minimum and maximum yield strength data in each group, using ImageJ software (Version 1.34, National Institutes of Health, Bethesda, MD). An equivalent pore diameter  $D_e$  (Yi *et al.*, 2003; Gao *et al.*, 2004) was used to describe the size of near-spherical or irregular shape pores, which is defined here as  $D_e = 2[A_p/\pi]^{1/2}$ , where  $A_p$  is the pore area measured directly from metallographic samples. For microstructural observation, the samples were etched in aqua regia solution for appropriate times to reveal their microstructures. Analysis of variance (ANOVA,  $\alpha = 0.05$ ) and the REGW multiple range test were used for statistical analysis of the mechanical property data.

## **2.3 Results**

### **2.3.1 Mechanical Properties**

Results of the two-way ANOVA tests for tensile properties of the three alloys are provided in Table 2.2, and the property values (means with standard deviations) are summarized in Table 2.3. In Table 2.3, the yield strength data provided by the manufacturer (after simulated porcelain-firing heat treatment) is also shown. Compared to the as-cast condition, the 0.2% offset yield strength for d.SIGN 59 significantly decreased after heat treatment, while percentage elongation at fracture for Aries significantly increased. Significant changes occurred in the ultimate tensile strength for the alloys after heat treatment. The ultimate tensile strength was significantly lower for Aries than for IS 64 and d.SIGN 59. All alloys exceeded the minimum yield strength of 250 MPa and the minimum percentage elongation of 3% requirements in ADA Specification No. 38 (2000).

### **2.3.2 Porosity and Microstructures of Sectioned Specimens**

The area fraction of porosity for specimens with lowest and highest yield strength values in each group are given in Table 2.4. In this table, the maximum equivalent pore diameters are also shown. The pores were evenly distributed in all specimens, as shown in Figure 2.1. No correlation was found between the mechanical property data and the area fraction of porosity or the maximum equivalent pore diameter. Analysis of variance shows that there is no significant difference ( $P = 0.22$ ) among the mean values of porosity area fraction in the three alloys.

SEM examination of polished and etched fractured specimens shows that although the three alloys had a similar equiaxed as-cast microstructure with the first solidified grain region and the last solidified region (LSR), which had a dendritic character, the constituents of the LSR region exhibited different details, as shown in Figure 2.2. After simulated porcelain-firing heat treatment, the as-cast microstructural characteristics in Aries were completely eliminated, with the formation of many spherical precipitates and grain boundary phases (Figure 2.3a); the precipitates in IS 64 were the same as in Aries. In d.SIGN 59, the precipitates inside the grains were platelet-like; in addition, many discontinuous grain boundary precipitates occurred (Figure 2b). A localized inhomogeneous microstructure with obvious traces of the as-cast microstructure was observed in the longitudinally-sectioned specimens of both IS 64 and d.SIGN 59, as shown in Figure 2.3c, indicating the microstructures of heat-treated IS 64 and d.SIGN 59 specimens were not completely homogenized by the simulated porcelain-firing heat treatment.

### ***2.3.3 SEM Examination of Fracture Surfaces***

All specimens exhibited typical ductile fracture character with many dimples on the fracture surfaces, as shown in Figure 2.4a. Porosity was also observed on the fracture surfaces. Figure 2.4b shows an SEM micrograph of the porosity on the fracture surface and surrounding dimples. The platelet precipitates in as-cast and heat-treated d.SIGN 59 can be seen in both micrographs.

## 2.4 Discussion

Compared to the complex microstructures in high-Pd alloys (Brantley *et al.*, 1993; Carr *et al.*, 1993; Papazoglou *et al.*, 1999; Papazoglou *et al.*, 2000), the microstructures of as-cast and simulated porcelain-firing heat-treated Pd–Ag alloys are relatively simple. The difference first arises from the fundamental difference between the binary phase diagrams of major elements in the alloys. According to the equilibrium binary Pd–Ga diagram (Figure 1.1), many complicated phases may occur in high-Pd alloys, while in Pd–Ag alloys, Pd and Ag have unlimited mutual solid solubility without phase transformation (Figure 1.2). Intermetallic compounds based on Pd–Sn (Figure 1.3) and Pd–In phases (Figure 1.4) may exist in both alloy systems, and in Pd–Ag alloys, additional intermetallic phases on the basis of Ag–Sn (Figure 1.5) and Ag–In (Figure 1.6) may also occur. During the practical dental casting process, alloys are known to undergo rapid solidification (Anusavice, 1996), and therefore the microstructures may deviate far from the multi-component equilibrium state.

The as-cast microstructure of the currently studied three Pd–Ag alloys with as-cast dendritic character is different from the as-cast dendritic microstructure in the Pd–Ag alloy W-1 (to be discussed in Chapter 3) and in high-Pd alloys (Carr *et al.*, 1993; Brantley *et al.*, 1999; Papazoglou *et al.*, 1999). The presence of a dendritic as-cast microstructure means that the amount of grain-refining element incorporated in the alloy is insufficient. After the simulated porcelain-firing heat treatment, numerous precipitates formed in all three Pd–Ag alloys in the present study. However, the yield strength and ultimate strength (except for yield strength in d.SIGN 59 to be discussed later) did not change significantly, which is consistent with the results obtained for the Pd–Ag alloy

Cameo-Lite (Heraeus Kulzer Jelenko, Armonk, NY) (Huget *et al.*, 1976). This apparent paradox may be explained by the presence of fine-scale precipitates in the as-cast and heat-treated conditions that could not be resolved at the SEM level. Such precipitates have been observed in Pd–Ag with similar compositions using the transmission electron microscope (TEM) (Chapter 5). The very close ratio of 0.2% yield strength to ultimate tensile strength (except for as-cast d.SIGN 59 to be discussed later) for the as-cast and heat-treated three alloys indicates the same hardening/strengthening mechanisms, which involve dislocations. Further TEM investigations of the present alloys are necessary to completely understand the hardening mechanisms.

In high-Pd alloys, after simulated porcelain-firing heat treatment, the yield strength (and ultimate tensile strength except for Spartan Plus) significantly decreased for the Pd–Cu–Ga alloys Liberty, Spartan Plus, and Option, but not for the Pd–Ga alloy Protocol (Papazoglou *et al.*, 1999; Papazoglou *et al.*, 2000). The changes in mechanical properties are attributed to the transformation of the hard phase (Wu *et al.*, 1997; Brantley *et al.*, 1999). The yield strength and ultimate tensile strength values of the Pd–Cu–Ga alloys are much higher than those of the current three Pd–Ag alloys under study. In addition, the ratio of 0.2% yield strength to ultimate tensile strength for the Pd–Cu–Ga alloys (from 0.72 to 0.89) is also higher than the ratio for the Pd–Ag alloys in both the as-cast and heat-treated conditions (from 0.52 to 0.57), indicating that different strengthening mechanisms are involved in the high-Pd and Pd–Ag alloy systems.

Among the various casting defects, porosity is considered to be the most persistent and common problem (Monroe, 2005). In dental casting alloys, casting defects such as pores and microshrinkage cannot be completely eliminated (Anusavice, 1996;

Mizumoto *et al.*, 2003). In engineering casting alloys, both ultimate tensile strength and percentage elongation at fracture were sensitive to variations in porosity and decreased significantly with increase in porosity content, whereas yield strength was almost independent of porosity in casting aluminum alloys (Ashton *et al.*, 1975; Herrera and Kondic, 1979; Samuel AM and Samuel FH, 1995), casting magnesium alloys (Liu *et al.*, 2000), and casting superalloy (Chang *et al.*, 1989). Present results indicate that the ultimate tensile strength and elongation percentage variation in the three Pd–Ag alloys is much smaller than that for yield strength. It is probable that other factors in addition to porosity are attributable to the abnormal variation in mechanical properties.

Among the four specimens in the as-cast d.SIGN 59 group, the yield strength value for one specimen (No. 9 in Table 2.4) was far lower than the values of the other three specimens (470 MPa *vs.* 601 MPa, 610 MPa, and 614 MPa), while the ultimate tensile strength values were very close (800 MPa *vs.* 849 MPa, 835 MPa, and 835 MPa, respectively). The lowest yield strength value of this specimen is comparable to the yield strength data in the heat-treated group and for the other two Pd–Ag alloys. Microstructure examination revealed that there were far more precipitates in the LSR region of the three as-cast high yield strength specimens than were present in the lowest yield strength specimen (Figure 2.2d for the highest strength specimen *vs.* Figure 2.2c for the lowest strength specimen). The precipitates are also much more numerous than those in Aries and IS 64 (Figure 2.2d *vs.* Figures 2.2a and 2.2b). Moreover, porosity measurements (Table 2.4) and fracture surface examination did not reveal any abnormal defects in this low-strength specimen. It is plausible to attribute the high yield strength of as-cast d.SIGN 59 to the high content of precipitates that formed in the LSR region in the three

specimens. The reason for the high yield strength of these three d.SIGN 59 specimens needs further investigation. After simulated porcelain-firing heat treatment, the as-cast microstructures of IS 64 and d.SIGN 59 were not completely eliminated in the longitudinally sectioned specimens, and the inhomogeneous microstructure may contribute to the relatively larger variation of mechanical properties for IS 64 and d.SIGN 59 than for Aries. Similar microstructural effects on variation in mechanical properties was observed in cast aluminum alloys (Mugica *et al.*, 2004). It is also worth noting that the yield strength data obtained for each alloy after simulated porcelain-firing heat treatment is lower than the data provided by the manufacturer. This difference can be attributed mainly to the loss of effective cross-section area resisting stress during mechanical testing, which results from the presence of porosity.

## **2.5. Conclusions**

1. In the presence of porosity up to 4%, the three Pd–Ag alloys, Aries, IS 64, and d.SIGN 59, exhibited acceptable mechanical properties for clinical use.
2. After simulated porcelain-firing heat treatment, the microstructure of Aries was completely homogenized, although this did not occur in IS 64 and d.SIGN 59. Numerous precipitates occurred, and the spherical precipitates inside grains and at grain boundaries were similar in Aries and IS 64. In d.SIGN 59 the precipitates inside grains were platelet-like, and many discontinuous grain boundary precipitates were also observed.
3. Casting porosity and variation in microstructures were considered the causes of variation in mechanical properties among specimens of the same alloy.

Alloy	Au	Pd	Ag	Pt	Zn	Sn	In	Ga	Li	Re	Ru
<b>Aries</b>	-	63.7	26.0	-	-	7.0	1.5	1.8	-	< 1.0	< 1.0
<b>IS 64</b>	2.8	59.9	26.0	1.0	-	7.0	1.5	1.8	-	< 1.0	< 1.0
<b>d.SIGN 59</b>	-	59.2	27.9	< 1.0	1.3	8.2	2.7	-	< 1.0	< 1.0	< 1.0

Table 2.1. Nominal compositions (wt. %) of Aries, IS 64 and d.SIGN 59 (provided by Ivoclar Vivadent).

Independent Variable	$\sigma_{0.2}$	UTS	$\delta$
Alloy	P < 0.0001 Significant	<0.0001 Significant	<0.0001 Significant
Condition	0.0066 Significant	0.0002 Significant	0.0004 Significant
Alloy . Condition	0.0004 Significant	0.0925 Not significant	<0.0001 Significant

Table 2.2. Summary of two-way ANOVA results for comparison of mechanical property measurements.

Alloy	Condition	$\sigma_{0.2}$ (MPa)	$\sigma_{0.2}^*$ (MPa)	UTS (MPa)	$\sigma_{0.2}/\text{UTS}$	$\delta$ (%)
Aries	AC	410 (8)	-	731 (7)	0.56	32 (4)
		A		A		A
Aries	HT	388 (17)	415	690 (4)	0.56	46 (2)
		A		A		B
IS 64	AC	410 (34)	-	794 (19)	0.52	28 (4)
		A		B		AC
IS 64	HT	441 (26)	560	781 (16)	0.57	26 (2)
		A		B		C
d.SIGN 59	AC	574 (70)	-	830 (21)	0.69	16 (2)
		B		B		D
d.SIGN 59	HT	430 (24)	490	773 (33)	0.56	18 (1)
		A		B		D

AC: as-cast; HT: simulated porcelain-firing heat treatment.

$\sigma_{0.2}$ : yield strength for 0.2% offset permanent strain in tension.

$\delta$ : percentage elongation at fracture.

\*Values of yield strength reported on the website of the manufacturer. Except this data from the manufacturer, all data measured in this study are mean (standard deviation).

Table 2.3. Mechanical properties of Aries, IS 64 and d.SIGN 59. Groups in the same column with the same letters are not significantly different ( $P > 0.05$ ).

Alloy	Condition	No.	$\sigma_{0.2}$ (MPa)	$\Delta\sigma_{0.2}^1$ (MPa)	$\Delta\sigma_{0.2}^2$ (MPa)	UTS (MPa)	$\delta$ (%)	Porosity (%)	Max $D_e$ ( $\mu\text{m}$ )
Aries	AC	1	401	-9	†	738	31	1.7	54
		2	418	8	†	728	29	1.9	50
	HT	3	366	-22	-49	690	44	2.1	52
		4	408	20	-7	684	48	2.9	53
IS 64	AC	5	385	-15	†	818	33	2.7	43
		6	457	47	†	779	24	2.5	50
	HT	7	423	-18	-137	785	29	2.9	61
		8	480	39	-80	802	27	3.8	52
d.SIGN 59	AC	9	470	-104	†	800	18	3.9	65
		10	614	40	†	835	14	2.3	26
	HT	11	405	-25	-85	786	17	2.2	54
		12	459	29	-31	783	18	2.6	61

AC: as-cast; HT: simulated porcelain-firing heat treatment;  $\sigma_{0.2}$ : 0.2% yield strength (MPa);  $\Delta\sigma_{0.2}^1$ : the 0.2% yield strength difference between data for the specimen and mean value in the group;  $\Delta\sigma_{0.2}^2$ : the 0.2% yield strength difference between data for the specimen and the value provided by the manufacturer; †: as-cast yield strength value by the manufacturer not available.

Table 2.4. Mechanical properties, porosity area fraction and maximum equivalent pore diameter of specimens with the lowest and highest 0.2% yield strength in each testing group in Table 2.3.

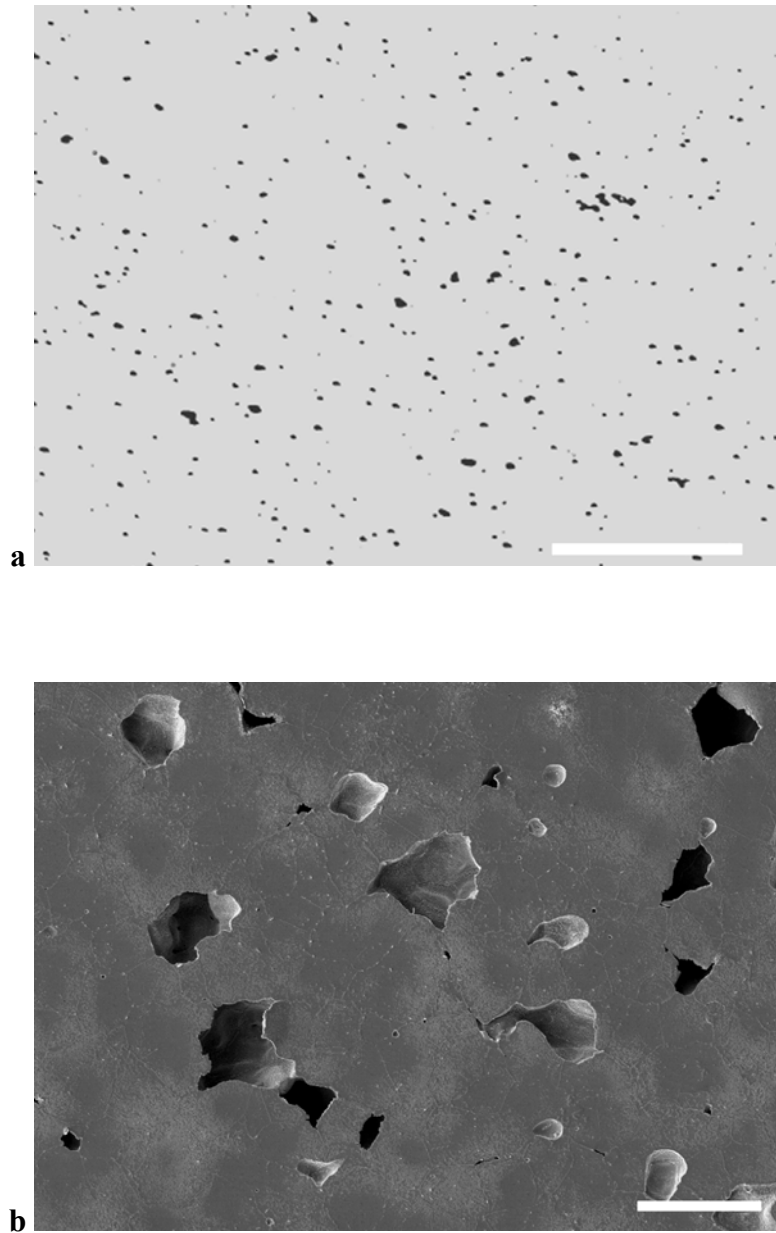
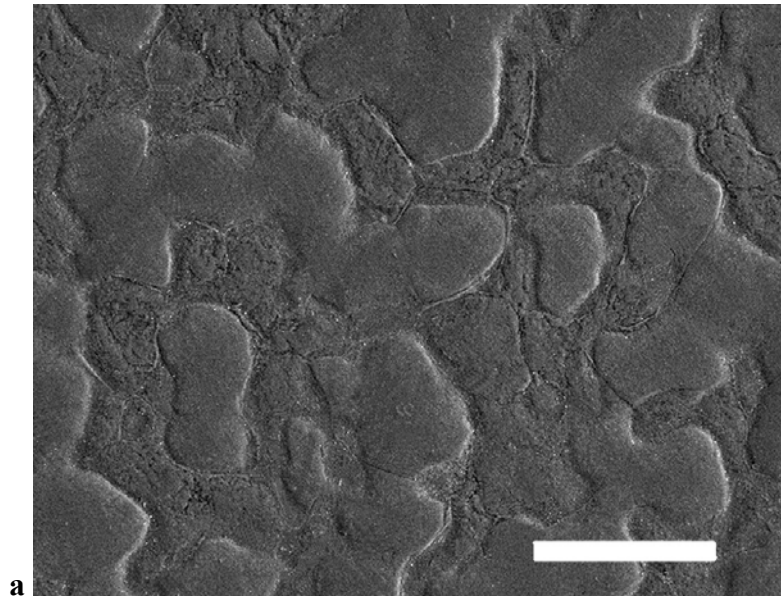
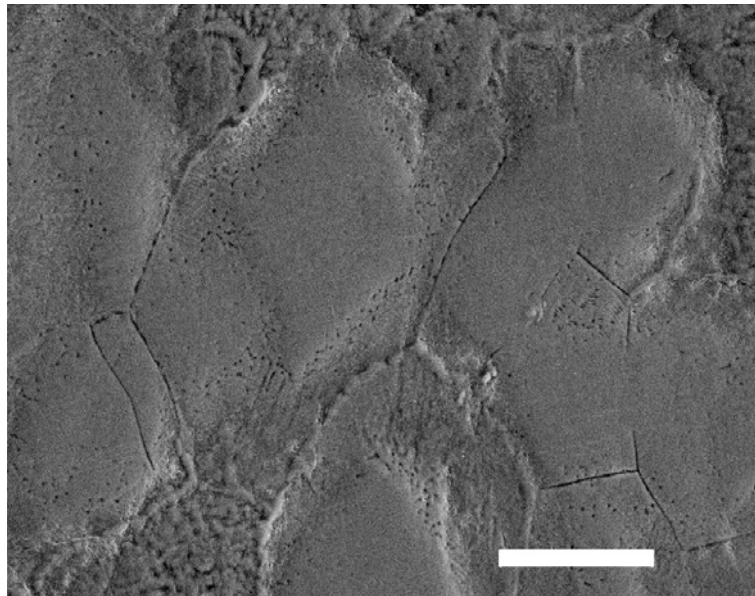


Figure 2.1. Porosity in the longitudinally sectioned fractured heat-treated Aries (a) and d.SIGN 59 (b) specimens. (a) Low-magnification optical microscope photograph showing evenly distributed pores. Bar = 400  $\mu\text{m}$ ; (b) SEM photomicrograph showing the morphology of the pores. Bar = 50  $\mu\text{m}$ .



**a**

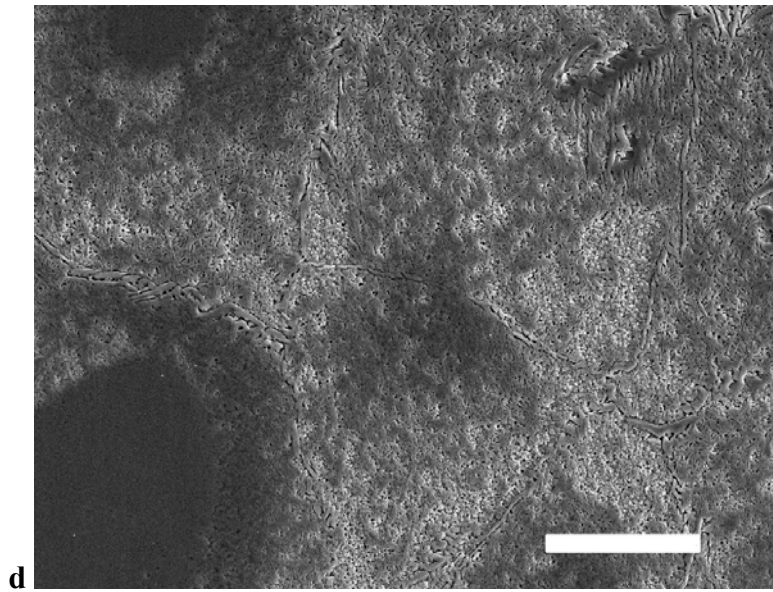
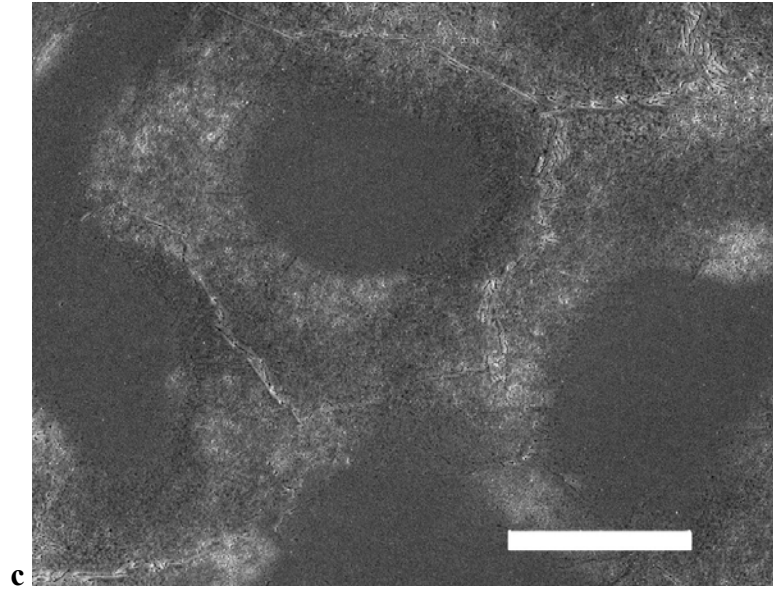


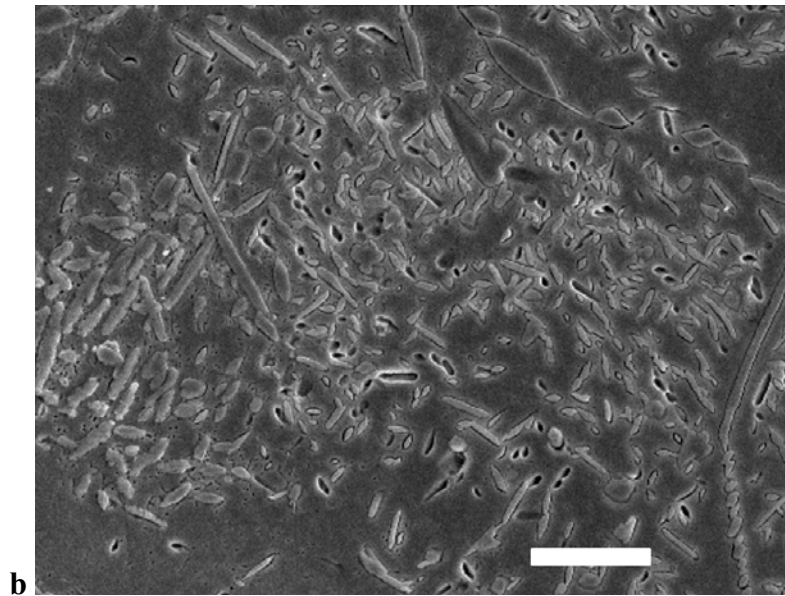
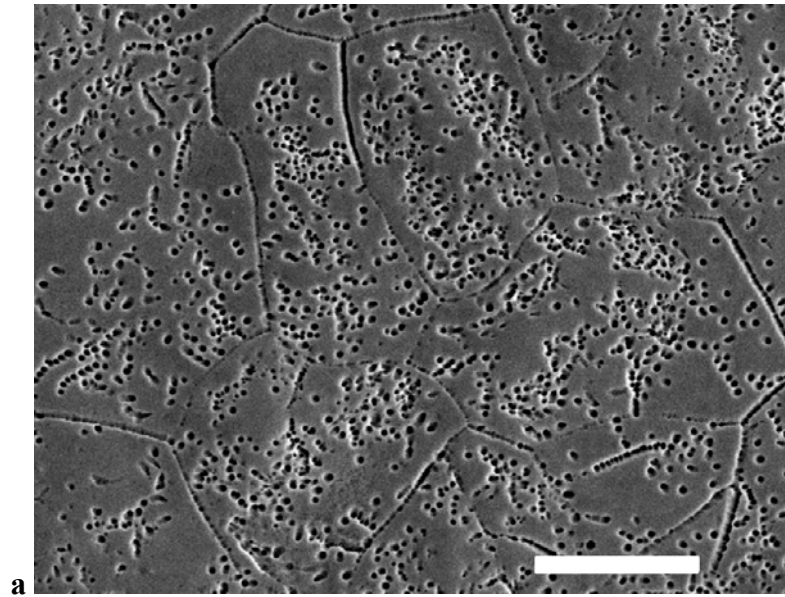
**b**

Continued

Figure 2.2. Scanning electron micrographs showing the as-cast microstructure of (a) Aries. Bar = 30  $\mu\text{m}$ ; (b) IS 64. Bar = 10  $\mu\text{m}$ ; (c) d.SIGN 59 specimen with the lowest yield strength in the group (Specimen No. 9 in Table 2.4). Bar = 15  $\mu\text{m}$ ; (d) d.SIGN 59 specimen with highest yield strength (Specimen No. 10 in Table 2.4). Bar = 10  $\mu\text{m}$ .

Figure 2.2 continued

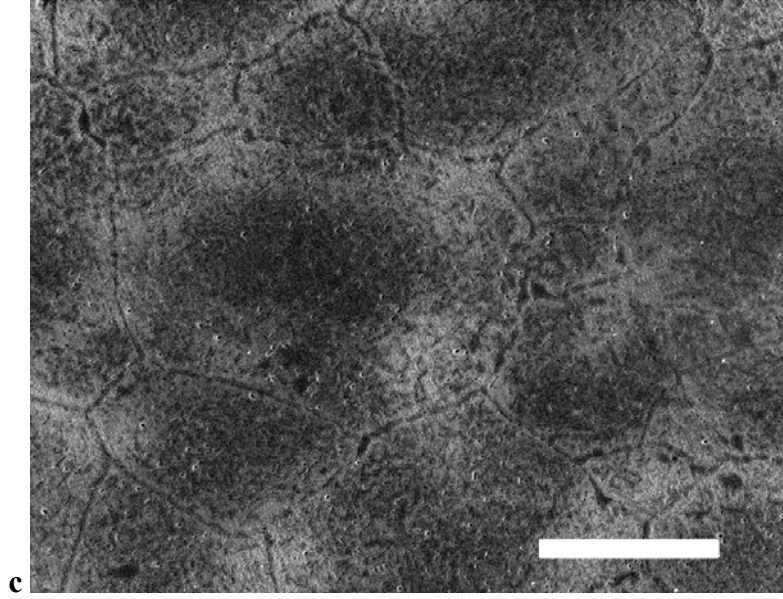




Continued

Figure 2.3. Scanning electron micrographs showing microstructures of specimens after simulated porcelain-firing heat treatment: (a) Aries. Bar = 10  $\mu\text{m}$ ; (b) d.SIGN 59. Bar = 5  $\mu\text{m}$ ; (c) longitudinally sectioned d.SIGN 59. Bar = 20  $\mu\text{m}$ . Specimens (a) and (b) were sectioned perpendicularly to the axis of the tensile test specimen.

Figure 2.3 continued



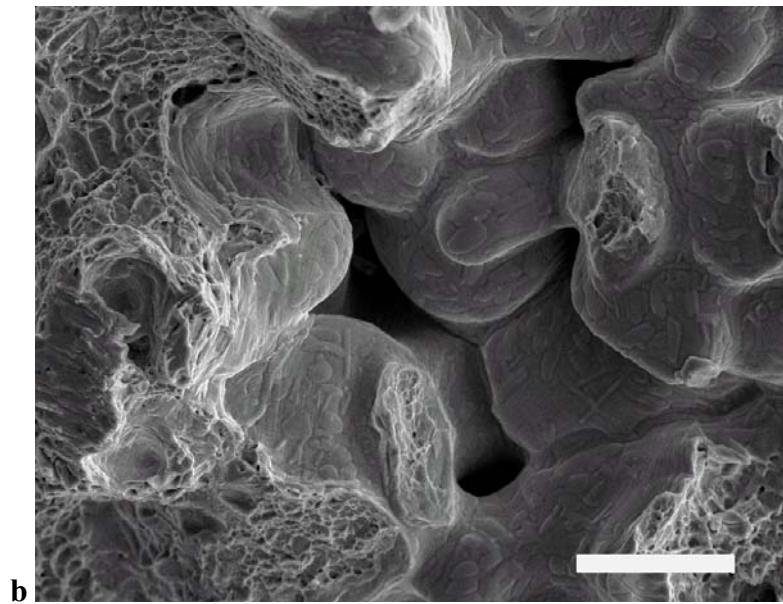
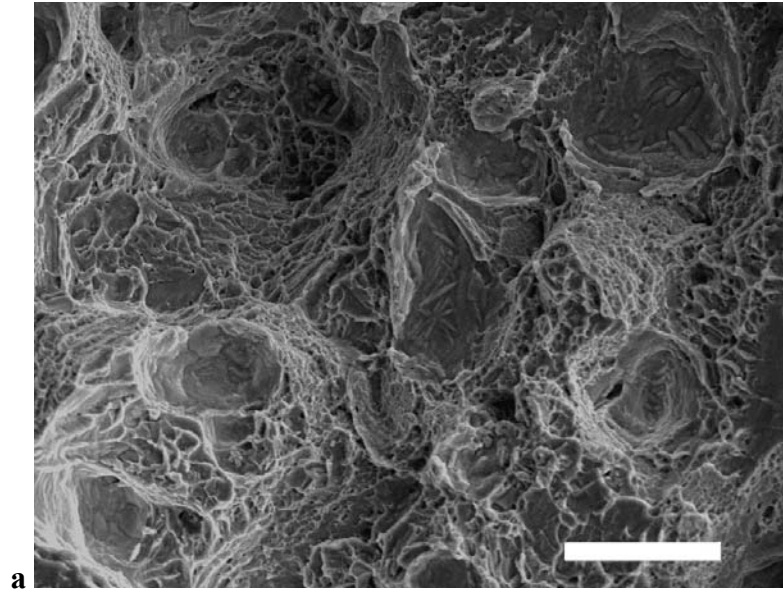


Figure 2.4. Scanning electron micrographs of fractured surfaces showing: (a) dimples and embedded platelets in as-cast d.SIGN 59. Bar = 10  $\mu\text{m}$ ; (b) porosity and embedded platelets in heat-treated d.SIGN 59. Bar = 10  $\mu\text{m}$ .

**CHAPTER 3**

**EFFECTS OF PORCELAIN-FIRING AND ISOTHERMAL TREATMENT**

**ON THE MICROSTRUCTURES AND HARDNESS**

**OF PALLADIUM–SILVER ALLOYS**

**3.1 Introduction**

In recent years, due to the palladium price volatility, Pd–Ag dental casting alloys have regained interest for metal-ceramic restorations in dentistry due to their favorable properties and unit metal cost compared to alternative gold alloys. In these Pd–Ag dental alloys, in addition to the major elements of Pd (50 – 60 wt. %) and Ag (28 – 40 wt. %), lower-melting point elements such as Sn, In and Zn are usually added to increase the fluidity to the molten metal and thereby improve castability. Tin and indium react easily with oxygen and thus enhance bonding with porcelain for metal-ceramic restorations. In addition, Sn and In form intermetallic compounds with both Pd and Ag, which contribute to the age-hardening of certain alloys (Huget and Civjan, 1974; Goodacre, 1989; Hisatsune *et al.*, 1990; Pinasco *et al.*, 1999; Guo *et al.*, 2003b). The two major elements Pd and Ag in these alloys are completely miscible in the solid state and form a continuous series of solid solutions. However, due to the minor elements in the compositions and the nonequilibrium dental casting conditions, several microstructural constituents or phases

have been observed in as-cast and heat-treated Pd–Ag alloys subjected to simulated porcelain-firing conditions (Mezger *et al.*, 1989b; Vermilyea *et al.*, 1996; Pinasco *et al.*, 1999; Guo *et al.*, 2003b).

The microstructural changes and age hardening for Pd–Ag alloys during annealing heat treatment have been studied by several investigators. Payan *et al.* (1986) observed hardness changes in an experimental 59.3Pd–29.6Ag–8.8Sn–2.2In (wt. %) dental alloy during annealing from 400° to 1000°C for 1 hour. The maximum hardness occurred for the annealing temperature of 650°C. Age hardening was attributed to the internal oxidation phenomenon that had been reported earlier by Mackert *et al.* (1983).

The mechanism involved in age-hardening of a 55Pd–36Ag–5Sn–4In alloy (wt. %) (Byron, Nippon Shiken Dental Co., Tokyo, Japan) was characterized by Hisatsune *et al.* (1990). They found that in the early aging stage, a metastable ordered face-centered tetragonal (fct) phase based on Pd<sub>3</sub>In formed within the grains, and hardening was due to the coherency strain between the metastable structure and the fcc matrix. In the later aging stage, a lamellar structure, consisting of a stable ordered fct phase based on Pd<sub>3</sub>In and a stable fcc phase, extended from the grain boundaries to the interiors of the grains. These lamellae finally covered the entire grains and resulted in softening.

The fct phase was also identified by Pinasco *et al.* (1999) in the 57.9Pd–29.7Ag–5.4Sn–3.7In alloy Gamma Cast (Puppo Iori, Genoa, Italy) using x-ray diffraction. They proposed that despite the presence of several microstructural constituents having different appearances, the alloy microstructure actually consisted of only two phases, the face-centered cubic (fcc) matrix and a tetragonal phase. These investigators did not determine whether the tetragonal phase was ordered.

In a recent transmission electron microscope (TEM) study of the as-cast and simulated porcelain-firing heat-treated Pd–Ag–In–Sn alloy Super Star (Heraeus Kulzer Jelenko, Armonk, NY) (Guo *et al.*, 2003b), two distinct phases were observed in the as-cast microstructure: the fcc Pd solid solution matrix and fct precipitates found both in a eutectic structure (with the fcc phase) and in the matrix. After simulated porcelain-firing heat treatment, discontinuous fct precipitates also appeared in the matrix. The fct phase was determined by electron diffraction to be ordered, which confirmed the ordered structure of the phase observed by Hisatsune *et al.* (1990). Interfacial dislocations resulting from the misfit between the fct precipitates and the matrix was also observed by Guo *et al.* (2003b), which was consistent with the coherency strain hardening mechanism proposed by Hisatsune *et al.* (1990).

Procedures involved in preparation of metal-ceramic restorations based on Pd–Ag alloys generally follow four main steps: initial alloy oxidation, opaque porcelain application, body porcelain application, and glazing. In Chapter 2, the microstructures and mechanical properties of three Pd–Ag alloys before and after simulated porcelain-firing heat treatment were reported. The purpose of this study was to examine the effects of each of the porcelain-firing steps and isothermal annealing heat treatment on the microstructures and hardness of the same Pd–Ag dental casting alloys whose tensile mechanical properties were reported in Chapter 2.

### 3.2 Materials and Methods

Three commercial Pd–Ag alloys, Aries, IS 64 and IPS d.SIGN 59 (Ivoclar Vivadent, Amherst, NY), were used in this study. The nominal compositions of the alloys provided by the manufacturer are given in Table 2.1 of Chapter 2.

All samples in this study were sectioned from the head region near the gauge section of as-cast tensile test bars using a slow-speed water-cooled diamond saw and had a thickness of 1 mm. The preparation of the tensile test bars was described in Chapter 2. Except for the as-cast samples, all other samples were subjected to either of two types of heat treatment (Vita Vacumat 500 Dental Porcelain Furnace, Vita Zahnfabrik, Bad Säckingen, Germany): (1) the simulated entire porcelain-firing process, including initial oxidation and subsequent porcelain-firing cycles recommended for IPS Classic dental porcelain (Ivoclar Vivadent). The processing temperatures and times are given in Table 3.1. Samples after completion of each step in the porcelain-firing process were named according to the specific step. For example, Opaque II (OP2) sample means that the sample that has completed initial oxidation, Opaque I (OP1) and Opaque II (OP2) processing steps. Isothermal heat treatments were also performed from 400° to 950°C for 30 minutes with step intervals of 50°C. After heat treatment, each sample was hot mounted using conductive bakelite, ground and polished using a standard sequence of metallographic abrasives. Final polishing was performed with 0.3 µm alumina slurries. The samples were then etched in aqua regia solutions, and examined with a scanning electron microscope (SEM) (JSM-820, JEOL, Tokyo, Japan).

The bulk Vickers hardness of each sample was measured with an indenting force of 1 kg and a dwell time of 30 seconds. Five indentations were generally utilized to obtain the mean hardness. Indentation measurements were made using a measuring microscope (Measurescope, Model MM-11, Nikon Corporation, Tokyo, Japan).

### **3.3 Results**

#### ***3.3.1 Hardness Variation during Porcelain Firing Process***

The variation of Vickers hardness for the three alloys during entire porcelain firing process is shown in Figure 3.1. The hardness values of the as-cast samples are also presented in this figure. Compared to the as-cast condition and all other porcelain firing steps, the Vickers hardness of the initial oxidation samples for all three alloys reached the highest values. After each step in the subsequent porcelain-firing cycles, the Vickers hardness did not change substantially (less than 6%).

#### ***3.3.2 Hardness vs. Annealing Temperatures***

Figure 3.2 shows the change of Vickers hardness as a function of annealing temperature in the three alloys. The bulk hardness peaks occurred approximately at 550°, 600°, and 650°C for Aries, IS 64, and d.SIGN 59, respectively. During annealing heat treatment, the overall hardness variation of the first solidified grain region and the LSR region was quite close.

#### ***3.3.3 Microstructural Changes during Porcelain Firing Process***

In the as-cast condition, all three alloys exhibited a nearly equiaxed grain structure (Figure 2.2 in Chapter 2), with dendritic character in the LSR region. After initial oxidation, the as-cast microstructure of three alloys changed dramatically. For

example, many nearly spherical particles formed in Aries, as shown in Figure 3.3a. The microstructures of oxidized IS 64 and d.SIGN 59 were similar, retaining a faint trace of the original as-cast character (Figure 3.3b), without apparent precipitates as observed in Aries.

The microstructures after each of the subsequent porcelain firing steps were similar in Aries and IS 64. Other than after the Body I (BD1) step in Aries, the microstructures after all other heat treatment steps in both alloys consisted of spherical precipitates and discontinuous grain boundary precipitates. The spherical precipitates were similar to those in oxidized Aries (Figure 3.3a), even though the precipitates were smaller and their area fraction was different after the heat treatment steps. After the Body I step, new lath-like precipitates were observed in Aries, as shown in Figure 3.3c. In d.SIGN 59, the microstructures after each of porcelain firing steps consisted of numerous lamellar precipitates (Figure 3.3d), which were apparently different from the nearly spherical precipitates in Aries and IS 64. Discontinuous grain boundary precipitates also formed, with some connected in a ribbon-like manner.

### ***3.3.4 Microstructural Variation during Annealing Heat Treatment***

During the annealing heat treatment, no distinct microstructure change could be observed below 700°C in both Aries and IS 64, whereas the LSR region appeared to decrease at 750°C and spherical precipitates formed in the vicinity of the LSR region, as shown in Figure 3.4a. Clear compositional differences between the grain region and the LSR region could be observed using the SEM backscattering image mode (Figure 3.4b). At temperatures above 800°C, the width of the LSR region decreased apparently, and many spherical particles formed around the original LSR region. In IS 64, many needle-

like precipitates formed in the LSR region at 800° and 850°C (Figure 3.4c). In both alloys, a trace of the LSR region was still observed at 900° and 950°C (Figure 3.4d). In d.SIGN 59, there was no apparent microstructure change below 700°C. Figure 3.4e shows the microstructure of d.SIGN 59 after annealing at 650°C, which exhibited the highest hardness value for a specific annealing temperature. However, at 700°C, lamellar precipitates began to form in the LSR region and extended to the grain region. Figure 3.4f shows the typical microstructure consisting of the lamellar precipitates around the remaining LSR region. The lamellae still existed at 950°C and covered most areas in the microstructure. A few nearly spherical precipitates could be observed among the lamellar precipitates. Discontinuous grain boundary precipitates were also observed in d.SIGN 59 after annealing at higher temperatures, and their shape was nearly the same as that observed in Aries and IS 64.

### **3.4 Discussion**

Under the present experimental conditions, for the different porcelain-firing steps and for annealing at different temperatures, the nearly spherical precipitates that formed in Aries and IS 64 were different in shape from the lamellar precipitates in d.SIGN 59. In the Pd–Ag alloys Rx 91 and W-1, which have similar low In contents (less than 1 wt.%), similar nearly spherical fcc ordered precipitates were present (to be discussed in Chapter 4 and Chapter 5). The lamellar precipitates were also observed in Pd–Ag alloys with higher In content, such as 55Pd–36Ag–5Sn–4In (Hisatsune *et al.*, 1990), Super Star 60Pd–28Ag–5Sn–6In (Vermilyea *et al.*, 1996), and 57.9Pd–29.7Ag–5.4Sn–3.7In (Pinasco *et al.*, 1999). In Super Star, the two-phase lamellar precipitates were found to

contain an fct phase (Guo *et al.*, 2003b). It is therefore reasonable to attribute the morphology difference of the two types of precipitates to the effect of the element indium, and both precipitates probably were involved in different phase transformation mechanisms.

It is interesting that after the initial oxidation process, the as-cast microstructure disappeared and numerous precipitates formed in Aries, while in IS 64 and d.SIGN 59, the microstructure mainly exhibited the as-cast character. In addition, in the relatively large tensile test specimens after the simulated porcelain-firing heat-treatment, the as-cast microstructures were completely eliminated in Aries but not in IS 64 and d.SIGN 59 (Chapter 2). This means that the elemental redistribution and phase transformation rate in Aries is much higher than that in IS 64 and d.SIGN 59, and the related mechanisms need further study.

After each porcelain-firing step following the initial oxidation process, although the high temperature for each step varied from 910° (BD2) to 980°C (OP1), the microstructures exhibited no substantial change (mainly variation in the area fraction of the precipitates), and the Vickers hardness did not change significantly. This result has practical importance since, even when additional steps are needed (such as glazing), the Vickers hardness of the alloy (and corresponding yield strength) will not change significantly.

For annealing heat treatment, the Vickers hardness measurements presented in Figure 3.2 indicate that the bulk hardness of the three Pd–Ag alloys varied substantially. Although the highest Vickers hardness occurred at 550°, 600°, and 650°C for Aries, IS 64 and d.SIGN 59, respectively, no substantial microstructural changes could be detected

with the SEM for this annealing temperature range. The change in Vickers hardness with temperature for the bulk grain region and the LSR region is quite similar for all three alloys, and no individual region appeared to dominate the variation of bulk hardness. At higher annealing temperatures, the microstructure change in d.SIGN 59 is quite close to that observed by Hisatsune *et al.* (1990) in the Pd–Ag alloy 55Pd–36Ag–5Sn–4In, and to that in the Pd–Ag alloy Super Star (60Pd–28Ag–5Sn–6In, to be discussed in Chapter 4). The age hardening in these Pd–Ag alloys with higher In content can be explained by the coherency strain-hardening mechanism proposed by Hisatsune *et al.* (1990) and confirmed by Guo *et al.* (2003b). However, the microstructure variation at higher annealing temperatures in Aries and IS 64 seems different. The hardening can be attributed to the formation of the ordered fcc precipitates observed by TEM in the Pd–Ag alloys Rx 91 and W-1 (to be discussed in Chapter 5), which have similar lower In content. Further investigation of these precipitates using TEM is necessary in order to fully understand the hardening mechanisms in Aries and IS 64.

### **3.5 Conclusions**

Under the conditions of this study, the following conclusions can be drawn:

1. During the simulated porcelain-firing process after the initial alloy oxidation, the Vickers hardness reached its highest values in all three alloys. The microstructure in Aries was homogenized with numerous nearly spherical precipitates, whereas the as-cast microstructure character was retained in IS 64 and d.SIGN 59. After each of the subsequent porcelain-firing steps, the Vickers hardness in three alloys had no substantial change. The microstructure in Aries and IS 64 was similar and consisted

- of nearly spherical precipitates, while in d.SIGN 59, the microstructure was made up of lamellar precipitates. In all three alloys, in addition to the precipitates, discontinuous grain boundary precipitates were also observed.
2. During annealing heat-treatment, the highest hardness for Aries, IS 64 and d.SIGN 59 appeared at 550°, 600°, and 650°C, respectively. At temperatures below 700°C, no substantial microstructure change was observed at the SEM level. However, at higher temperatures, the microstructure changes were different. In Aries and IS 64, the LSR region started to decrease in width at 750°C with the occurrence of some spherical precipitates. In IS 64, many needle-like precipitates formed in the LSR region at 800° and 850°C. In d.SIGN 59, lamellar precipitates began to form in the LSR region and extended to the bulk grain region at 700°C, and these lamellae still existed at 950°C. In all three alloys a trace of the as-cast microstructure character was retained throughout the entire annealing temperature range.

Step	Low T (°C)	High T (°C)	Heating Rate (°C / min)	Time at High T
Initial Oxidation (OXD)	—	1010	—	5 min
1st Opaque Porcelain (OP1)	403	980	80	1 min
2nd Opaque Porcelain (OP2)	403	970	80	1 min
1st Body Porcelain (BD1)	403	920	60	1 min
2nd Body Porcelain (BD2)	403	910	60	1 min
1st Glazing (GZ1)	403	930	60	1 min
2nd Glazing (GZ2)	403	930	60	1 min

Table 3.1. Initial alloy oxidation procedure and porcelain-firing process for IPS Classic.

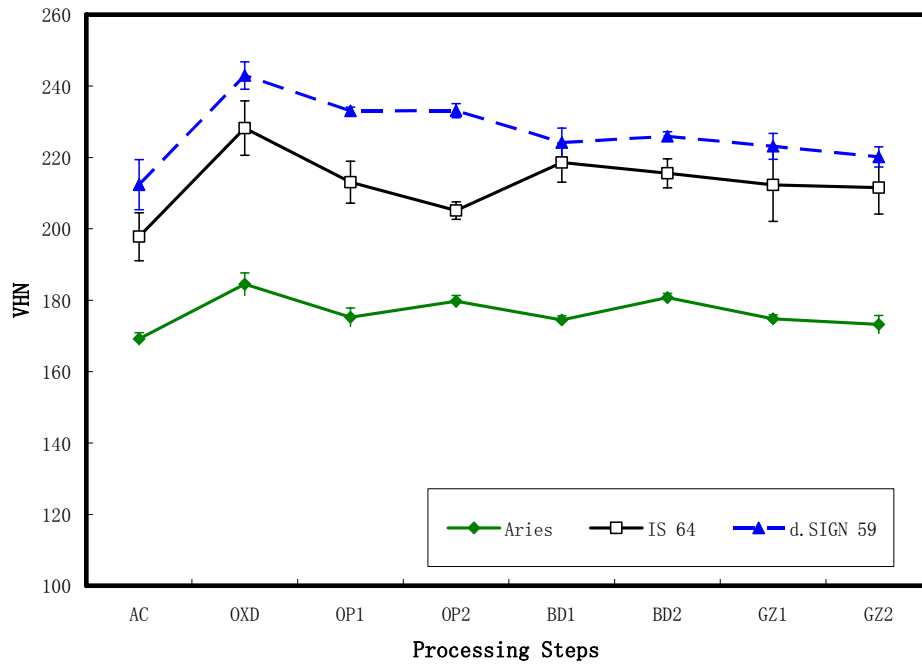


Figure 3.1. Variation of Vickers hardness after each step in the entire simulated porcelain-firing process. AC: as-cast; OXD: oxidation; OP1: opaque I; OP2: opaque II; BD1: body I; BD2: body II; GZ1: glazing I; GZ2: glazing II.

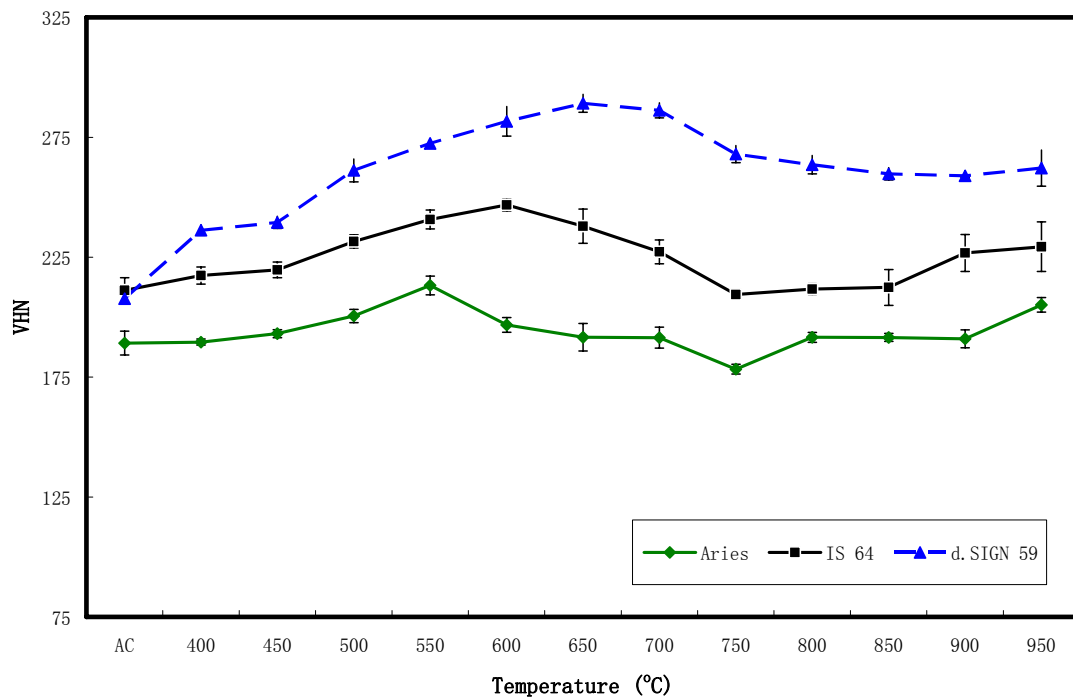
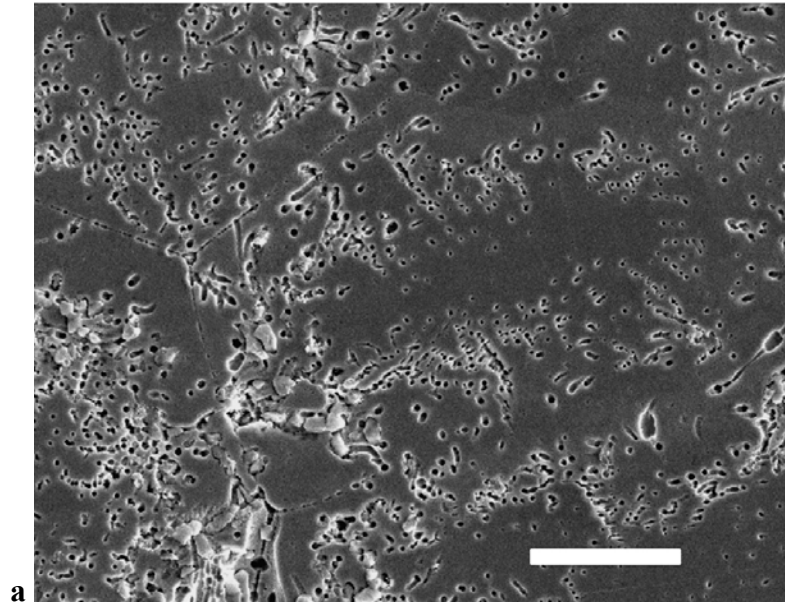
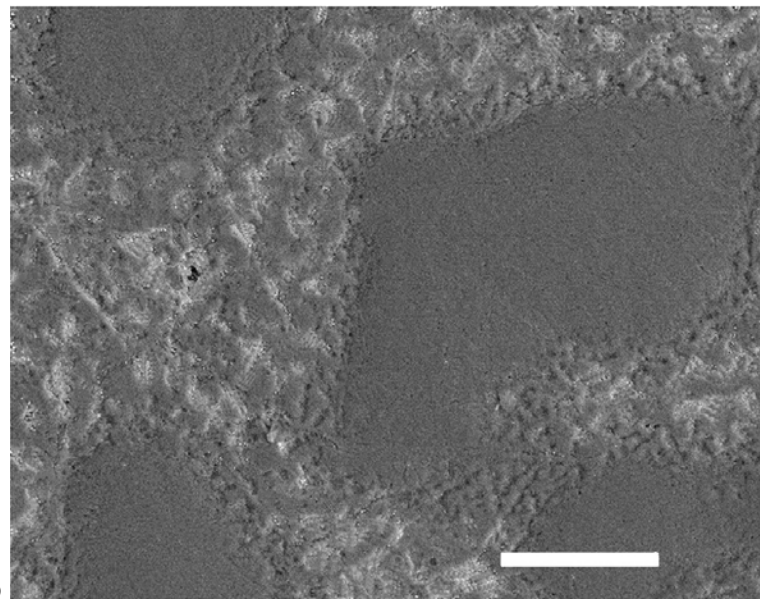


Figure 3.2. Vickers hardness as a function of annealing temperature for Aries, IS 64, and d.SIGN 59.



**a**

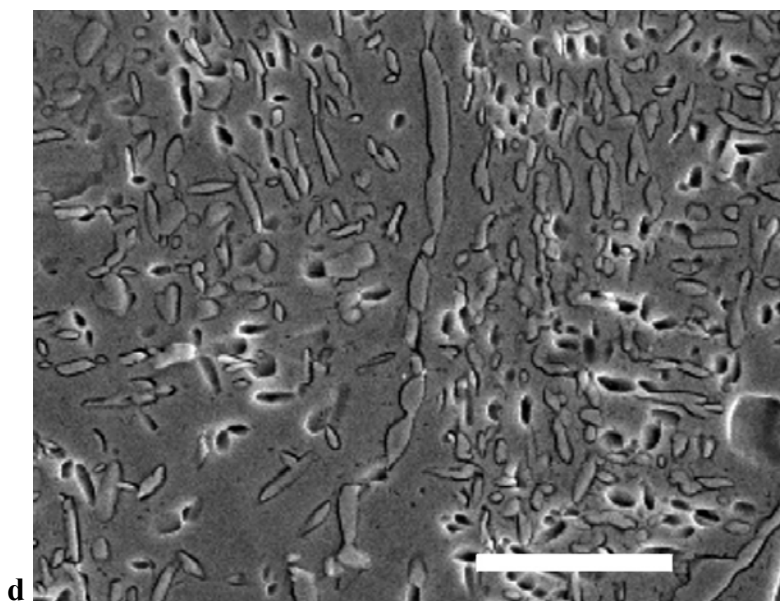
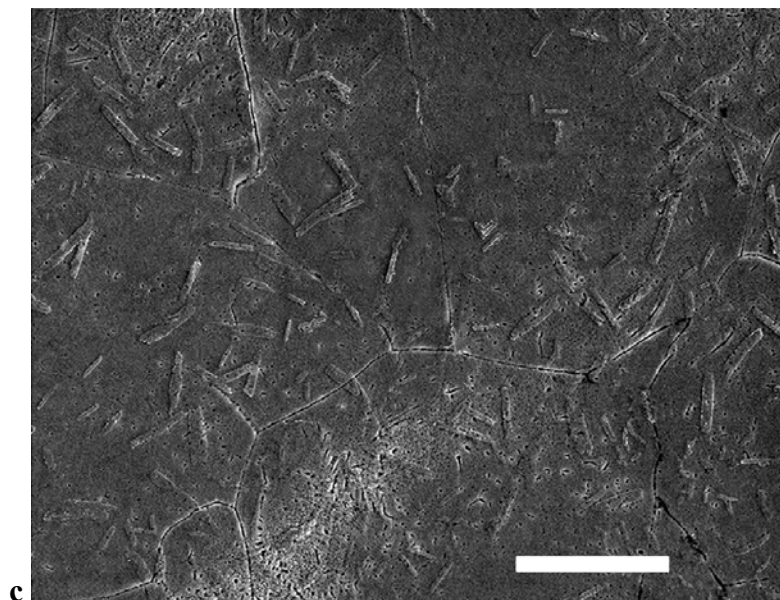


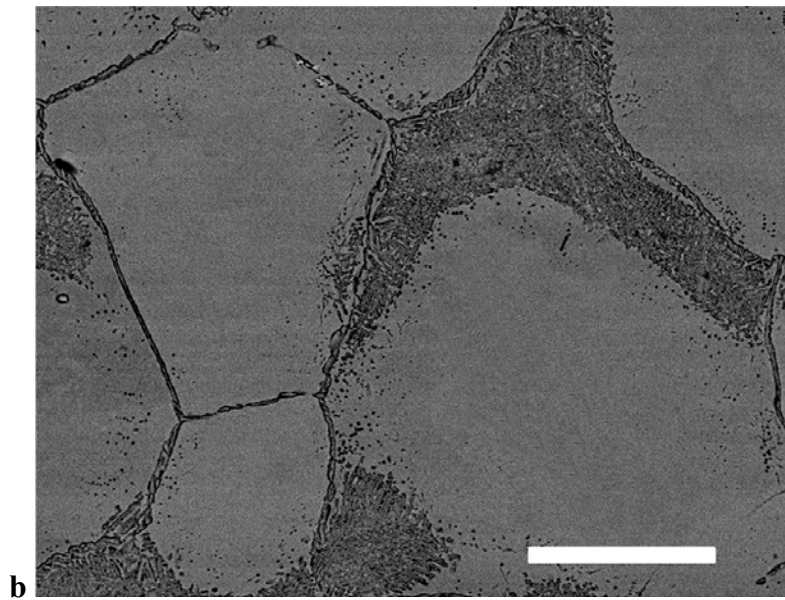
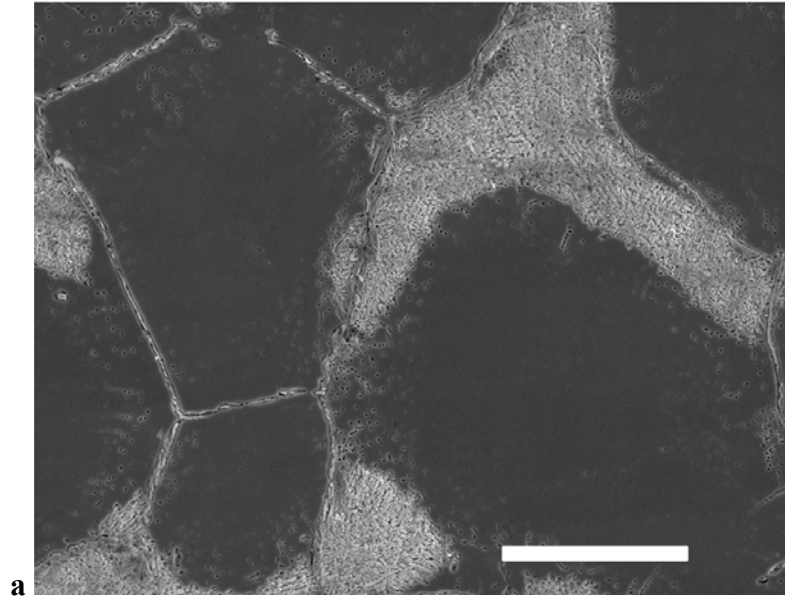
**b**

Continued

Figure 3.3. SEM micrographs showing the microstructures after different steps in the porcelain firing simulation process: (a) Aries after initial oxidation (length of scale bar = 10  $\mu\text{m}$ ); (b) IS 64 after initial oxidation (length of scale bar = 10  $\mu\text{m}$ ); (c) Aries after body I (length of scale bar = 10  $\mu\text{m}$ ); (d) d.SIGN 59 after glazing I (length of scale bar = 5  $\mu\text{m}$ ).

Figure 3.3 continued

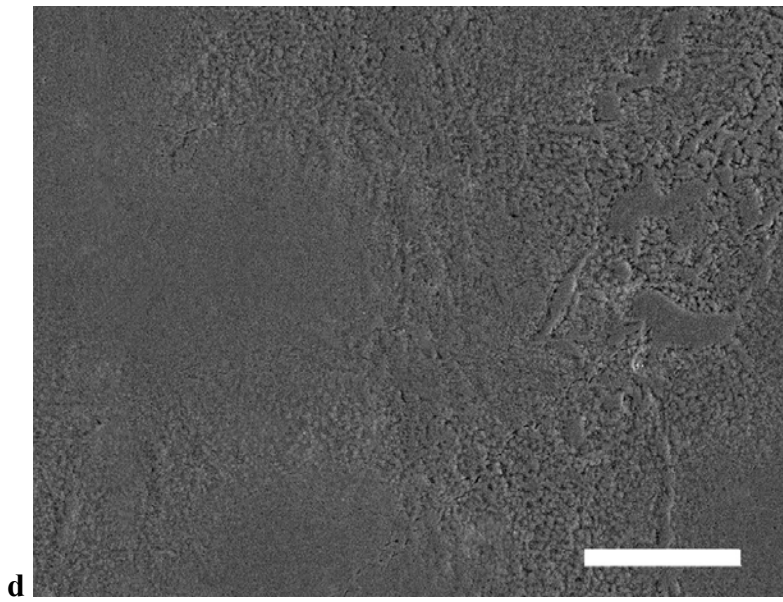
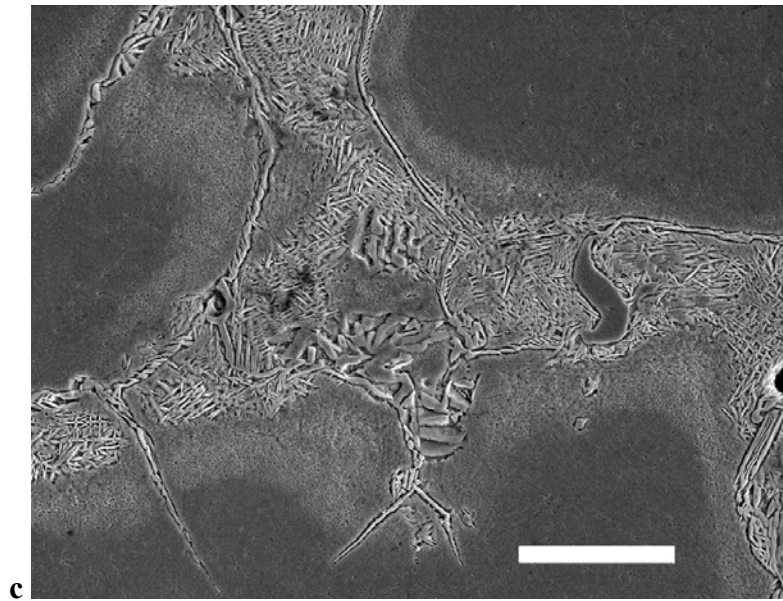




Continued

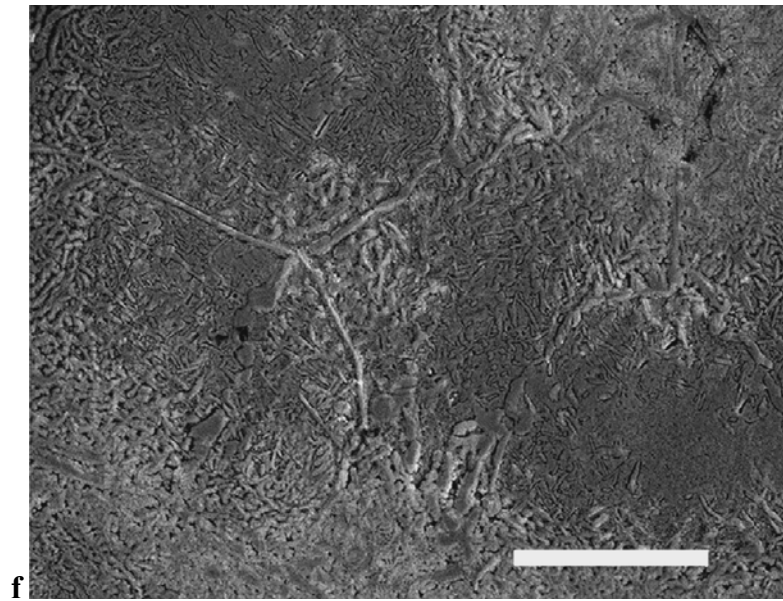
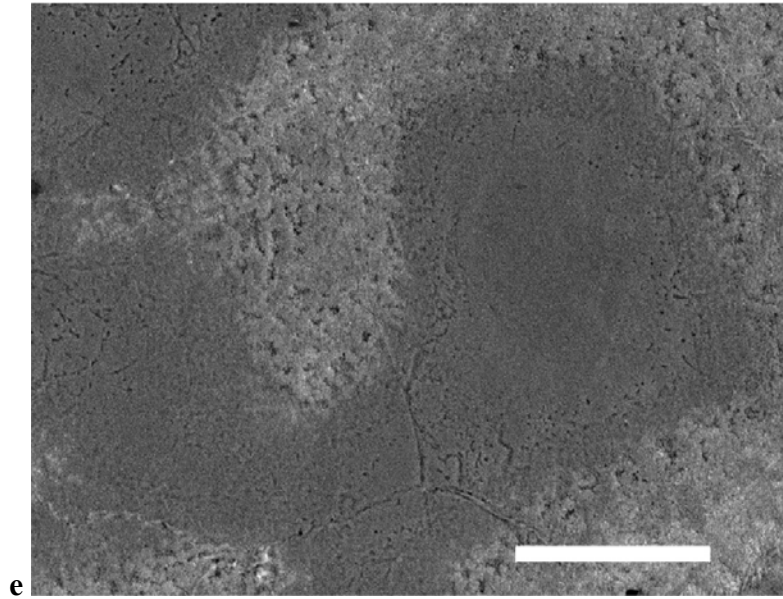
Figure 3.4. SEM micrographs showing the microstructures annealed at different temperatures: (a) Aries at 700 °C (length of scale bar = 15  $\mu\text{m}$ ); (b) back scattering image of (a) (length of scale bar = 15  $\mu\text{m}$ ); (c) IS 64 at 800 °C (length of scale bar = 10  $\mu\text{m}$ ); (d) IS 64 at 900 °C (length of scale bar = 10  $\mu\text{m}$ ); (e) d.SIGN 59 at 650 °C (length of scale bar = 15  $\mu\text{m}$ ); (f) d.SIGN 59 at 900 °C (length of scale bar = 15  $\mu\text{m}$ ).

Figure 3.4 continued



Continued

Figure 3.4 continued



## CHAPTER 4

### ANNEALING STUDY, VICKERS HARDNESS MEASUREMENTS AND MICROSTRUCTURAL OBSERVATIONS OF PALLADIUM–SILVER DENTAL ALLOYS

#### 4.1 Introduction

Palladium–silver alloys were first introduced for dental restorations in the 1970's as an alternative to costly gold-based dental alloys (Huget and Civjan, 1974; Goodacre, 1989). The Pd–Ag alloys have the highest elastic modulus and sag resistance during porcelain firing of all noble metal dental casting alloys, excellent porcelain-metal bonding, favorable handling characteristics, ease of soldering, and satisfactory tarnish and corrosion resistance (Walton and O'Brien, 1985; Mezger *et al.*, 1989c; Papazoglou and Brantley, 1998; Bertolotti, 2002). The commercially important alloys have a relatively narrow composition range, generally containing approximately 50% – 60% Pd, 30% – 40% Ag, and small amounts of Sn and In for porcelain bonding. The latter lower-melting point elements may also provide improved fluidity to the molten alloy and thus enhance castability. Because the original problem of porcelain greening

discoloration by these alloys has been largely eliminated (Blanco-Dalmau, 1983; O'Brien *et al.*, 1998; Bertolotti, 2002), the Pd–Ag alloys have become more popular than high-palladium alloys for metal–ceramic restorations, due to the recent price volatility of palladium.

Although palladium and silver form a solid solution system, non-equilibrium phases and microsegregation exist in the rapidly solidified as-cast dental Pd–Ag alloys, and precipitates are found after the porcelain-firing heat-treatment because of the Sn and In components in the alloy composition (Mackert *et al.*, 1983; Vermilyea *et al.*, 1996; Guo *et al.*, 2003b) investigated the behavior of the W-1 Pd–Ag dental alloy (Ivoclar Vivadent, Amherst, NY) during the initial oxidation procedure before porcelain firing and found that Pd–Ag nodules formed on the surface due to the internal oxidation of Sn and In. Payan *et al.* (1986) subsequently found that the hardness of an experimental 59.3Pd–29.6Ag–8.8Sn–2.2In (wt. %) dental alloy varied with annealing from 400° to 1000°C, attaining a maximum value at 650°C. Since the alloy was annealed in air, they concluded that the hardness variations resulted from the internal oxidation of Sn and In that had been reported by Mackert *et al.* (1983).

Our previous investigation of the Super Star Pd–Ag dental alloy (Heraeus Kulzer, Armonk, NY) (Guo *et al.*, 2003b) revealed that discontinuous precipitates occurred in the matrix phase during porcelain-firing heat treatment. The aim of this study was to investigate hardness variations and microstructures for three clinically popular Pd–Ag dental alloys subjected to annealing heat treatments over a wide temperature range, and gain insight into the relationships between precipitation processes and hardness changes.

## 4.2. Materials and Methods

Three representative Pd–Ag dental alloys (W-1, Rx 91, and Super Star) were selected for study. Nominal alloy compositions and nominal values of 0.2% yield strength (YS) (also termed proof stress) and percentage elongation at fracture for tensile loading and the simulated porcelain-firing heat-treated condition are listed in Table 4.1. A minimum value of 250 MPa for the latter is required in the current version of American Dental Association Specification No. 38 for casting alloys used in metal-ceramic restorations.

Preparation of cast specimens followed previously described procedures (Carr and Brantley, 1991). Wax patterns simulated a coping for a maxillary central incisor restoration, and castings were obtained with the use of a fine-grained, carbon-free, phosphate-bonded investment (Cera-Fina, Whip Mix Corp., Louisville, KY). The alloys were melted with a multi-orifice gas-oxygen torch, centrifugally cast in a broken-arm casting machine (Sybron/Kerr, Romulus, MI), and bench cooled. After divesting, castings were cross-sectioned into specimens having approximate dimensions 1.5 mm × 4 mm × 5 mm, using a low-speed, water-cooled diamond saw (Leco, St. Joseph, MI).

Isothermal annealing was performed on individual specimens for 30-minute time periods at temperatures from 400° to 950°C (with 50°C step intervals), using a nitrogen atmosphere. These temperatures encompass the normal range for the dental porcelain firing cycles. Subsequent to the annealing experiments, the furnace temperatures were corrected with a thermocouple to yield the actual annealing temperatures given in the figures to follow. After annealing, each specimen was resin-mounted, ground and polished using a standard sequence of metallographic abrasives. Following final

polishing with 0.05  $\mu\text{m}$  alumina slurries, specimens were etched in aqua regia solutions having the composition of  $1\text{HNO}_3 : 3\text{HCl} : 5\text{H}_2\text{O}$  (volume ratio). After sputter-coating with a thin Au-Pd film, etched microstructures were examined with an SEM (JSM-820, JEOL, Tokyo, Japan) at a range of magnifications.

The bulk Vickers hardness of each alloy after each annealing step was measured with an indenting force of 1 kg and loading time of 30 seconds. A lighter indenting force was used to obtain microhardness measurements of individual single-phase and multi-phase regions. The force magnitude was dependent on dimensions of the microstructural constituents, and a loading time of 30 seconds was again used. For Super Star and Rx 91, the small dimensions of the multi-phase regions necessitated an indenting force of 10 g, and lengths of the diagonals of the indentations were measured with the SEM. For W-1, the multi-phase and single-phase regions were sufficiently large that 25 g was used, and the lengths of the diagonals of the indentations were measured with the optical microscope attached to the hardness tester. Generally, 10 indentations were utilized to obtain values of bulk hardness and hardness of the separate microstructural constituents for each alloy at each annealing temperature.

## **4.3 Results**

### **4.3.1 *Hardness vs. Annealing Temperatures***

The bulk Vickers hardness and the hardness of individual microstructural regions as a function of annealing temperature are presented in Figure 4.1 for the three Pd–Ag alloys, where mean values and standard deviations are provided.

Figure 4.1a shows that the bulk hardness of W-1 reached its highest value at an annealing temperature of approximately 700°C. Hardness variations with annealing temperature for the single-phase palladium solid solution matrix were consistent with those for the bulk alloy. The annealing heat treatments had minimal effect on the hardness of the multi-phase interdendritic regions, showing that the bulk hardness changes for this alloy after annealing were mainly controlled by changes in the matrix phase. It can also be seen in Figure 4.1a that the bulk hardness for the W-1 alloy was greater than individual values of hardness for the matrix and the interdendritic regions.

The Rx 91 alloy had the same trend in hardness variations as W-1, which would be expected from their nearly identical compositions (Table 4.1), although bulk hardness values were higher for Rx 91. Figure 4.1b shows that the bulk hardness of Rx 91 had a maximum value at an annealing temperature of approximately 650°C. As with W-1, values of hardness for the palladium solid solution matrix in Rx 91 varied with annealing temperature in the same manner as the bulk hardness, and no meaningful variations in hardness caused by annealing were detected for the grain boundary regions. However, in contrast to W-1, the bulk hardness of Rx 91 was less than the individual hardness values for the matrix and the grain boundary regions.

For Super Star, two peaks in hardness were observed at annealing temperatures of approximately 500° and 650°C, as shown in Figure 4.1c. The lower-temperature peak was associated with the grain boundary regions, and the higher-temperature peak was associated with the matrix phase. The bulk alloy hardness was generally almost the same as the matrix phase and much less than the hardness of the grain boundary regions.

### 4.3.2 Microstructural Observations

No obvious microstructural differences were observed for the W-1 specimens annealed at the different temperatures. Typical microstructures are shown in Figure 4.2 for a specimen annealed at 922°C. Figure 4.2a shows the dendritic microstructure of this alloy, with a small amount of porosity in the white-appearing interdendritic regions that are the last portions of the alloy to undergo solidification. The complex multi-phase structure of an interdendritic region is shown in Figure 4.2b.

Figure 4.3a shows the microstructure of Rx 91 after annealing at 409°C. Equiaxed palladium solid solution grains can be seen, some of which appear to have a fine-scale etched substructure, but there is no general pattern of large precipitates within these grains. Elongated, narrow precipitates exist at the grain boundaries and are more evident at higher SEM magnification. Porosity can be seen at triple-point grain boundary junctions, as well as along a grain boundary and within one grain. Figure 4.3b shows the microstructure after annealing at 652°C, where the highest bulk hardness was found. Very small precipitates can be observed in both the matrix and grain boundary regions, along with submicron porosity in the center of the figure. Figure 4.3c shows that after annealing at 947°C, discontinuous precipitates appeared at the grain boundaries, and the fine-scale precipitates in the matrix have grown. The cube-shaped morphology of these precipitates is shown more clearly in Figure 4.3d. Using our previously described procedures for the study of ordered phases in Super Star (Guo *et al.*, 2003b), transmission electron microscopic (TEM) examination has shown that these cube-shaped precipitates

in Rx 91 are also ordered. Figure 4.3c shows that denuded regions exist near the discontinuous precipitates at the grain boundaries, within which the cube-shaped precipitates in the matrix are absent.

Figures 4.4 – 4.6 present photomicrographs of Super Star annealed at several temperatures based upon Figure 4.1c. Figure 4.4a is a secondary electron image of the microstructures after annealing at 417°C where the bulk alloy hardness was less than its maximum value. Wide multi-phase regions adjacent to the grain boundaries and grain boundary precipitates are evident. The corresponding backscattered electron image in Figure 4.4b shows the lower mean atomic number of the multi-phase regions adjacent to the grain boundaries, compared to the palladium solid solution matrix in the central portions of the grains. Figure 4.5a and b show microstructures after annealing at 512°C where the first hardness peak in Figure 4.1c appeared. The matrix phase has more distinct boundaries, and the grain boundary structure appears to be more complex. The multi-phase regions adjacent to the palladium solid solution in the centers of grains have also become more uniform. Figure 4.6a presents the microstructure after annealing at 561°C, where the bulk alloy hardness has decreased. The regions containing the grain boundary precipitates have become narrower, and the widths of adjacent multi-phase regions have increased. The microstructure after annealing at 662°C, where the bulk hardness is a maximum, is presented in Figure 4.6b and shows further increase in the complexity and width of the multi-phase regions adjacent to the grain boundaries, along with evidence of fine-scale precipitation in the matrix. After annealing at 947°C, which causes a decrease in bulk hardness, the microstructure shown in Figure 4.6c contains

needle-like (acicular) precipitates, as well as discontinuous precipitates in both the matrix and grain boundaries. Residual dendrites in the microstructure, which can be observed in photomicrographs obtained after annealing at lower temperatures, have disappeared.

#### **4.4 Discussion**

Annealing investigations (Niemi and Herø, 1984; Tani *et al.* 1991; Watanabe *et al.*, 2001) have been performed on noble dental alloys other than Pd–Ag alloys because phase transformations exist that cause substantial strengthening and potentially result in improved clinical performance. Since Pd–Ag binary alloys form a simple solid solution system without further solid state reactions (Okamoto, 2000), any phase transformations during annealing would necessarily involve the solute elements, Sn and In, which have important roles in Pd–Ag dental alloys for porcelain adherence and contribute to alloy castability (Bertolotti, 2002). The roles of Sn and In for formation of secondary microstructural phases were evident in our recent TEM study of the Super Star alloy (Guo *et al.*, 2003b).

Vickers hardness measurements presented in Figure 1 indicate that the bulk hardness of the W-1, Rx 91, and Super Star Pd–Ag alloys varied substantially during isothermal annealing. Comparison of the hardness changes of each bulk alloy, with hardness changes in the palladium solid solution matrix and in the other major microstructural constituent has shown that the dominant precipitation process occurs in the matrix phase. While SEM observations of the annealed Pd–Ag alloys (Figures 4.2 – 4.6) provide considerable detail about their microstructures, study of the fundamental nature of relevant strengthening mechanisms requires TEM examination of deformed

alloys that have been loaded in both uniaxial tension and cyclic fatigue. Such studies have been performed on high-palladium dental alloys (Guo *et al.*, 2002; Guo *et al.*, 2003a), and will be reported in a future article for the three Pd–Ag alloys selected for this study.

Although Table 4.1 shows that there are no large compositional differences for these three Pd–Ag alloys, their microstructures have notable differences. As-cast Super Star has a nearly equiaxed grain structure with extensive microsegregation, some residual dendrites and a fine-scale grain-boundary eutectic structure. This multi-phase microstructure becomes substantially homogenized after the firing cycles for dental porcelain (Vermilyea *et al.*, 1996; Guo *et al.*, 2003b). As-cast Rx 91 has an equiaxed grain structure with minimal microsegregation and no residual dendrites while as-cast W-1, which has a very similar composition (Table 4.1) has a dendritic microstructure. (The value of 0.2% yield strength reported by the manufacturer is much higher for Rx 91 compared to W-1.) Microstructural differences for these two alloys are attributed to the proportions of In and Sn, the amounts or absence of refractory grain refinement elements such as Ru and Re (Nielsen and Tuccillo, 1966; Brantley *et al.*, 1993), and other proprietary alloying strategies such as the use of Li (Table 4.1).

The precipitation processes that caused hardness changes in the three commercial Pd–Ag alloys (Figure 4.1) were not due to formation of internal In and Sn oxides, as suggested by Payan *et al.* (1986) for their air-annealing of an experimental Pd–Ag alloy of similar composition, since the present annealing was performed in a nitrogen

atmosphere. Both the present and Payan *et al.* (1986) studies found that the major precipitation process for increased hardening of the Pd–Ag alloys studied occurs at approximately 650°C.

For W-1, high-temperature annealing at 922°C (approximate upper-temperature limit of porcelain firing cycles) could not convert the dendrites in the as-cast alloy to equiaxed grains. The fine-scale microstructure did not permit identification at the SEM level of precipitates in the matrix phase that were responsible for hardness changes during annealing. For Rx 91, the cube-shaped precipitates in the matrix that were responsible for the hardening were readily observed with the SEM, and growth of these precipitates at higher temperatures (overaging) accounts for the decrease in hardness. Growth of discontinuous precipitates in the grain boundaries at the highest annealing temperature required solute elements that were needed for formation of the cube-shaped precipitates, accounting for the adjacent regions that were denuded of the latter precipitates. For Super Star, comparison of microstructures of specimens annealed at 407° and 512°C, where the first hardening peak occurred, reveals the occurrence of some elemental diffusion to improve the microstructural homogeneity, but no obvious precipitation processes in the multi-phase regions outside of the matrix phase could be identified because of the limited SEM resolution. These precipitation processes have been studied by TEM and will be reported in our subsequent publication.

## 4.5 Conclusions

Based upon Vickers hardness measurements and SEM observations of three commercial Pd–Ag alloys (W-1, Rx 91 and Super Star), the following conclusions can be drawn:

1. For all three alloys, the dominant change in bulk hardness during annealing between temperatures of approximately 400° to 950°C was due to precipitation in the palladium solid solution matrix phase. The highest Vickers hardness occurred at approximately 700°C for W-1 and 650°C for Rx 91. For Super Star, there were two peaks at approximately 500° and 650°C, with the lower-temperature peak controlled by multi-phase regions adjacent to the matrix grains and the higher-temperature peak by the matrix phase.
2. Although the W-1 and Rx 91 alloys have very similar compositions, the former has a dendritic as-cast microstructure and the latter has an as-cast microstructure with equiaxed grains. Possible reasons for these different microstructures are the proportions of In and Sn in the alloy compositions, the absence or presence of grain refinement elements, and the use of other proprietary strategies by the manufacturers.
3. The needle-like precipitates and the discontinuous precipitates that form in Super Star at the highest annealing temperature cause a reduction in hardness. This annealing temperature and the 30 minute annealing time are sufficient to eliminate the residual dendrites present in the as-cast alloy.
4. Detailed understanding of the precipitation processes that occur during annealing these Pd–Ag alloys requires the use of transmission electron microscopy.

Alloy	Pd	Ag	Sn	In	Balance	$\sigma_{0.2}$ (MPa)	Vickers Hardness	Elongation (%)
W-1*	53.3	37.7	8.5	< 1%	Ru, Li each < 1%	485	240	11
Rx 91 <sup>†</sup>	53.5	37.5	8.5	< 1%	Ru < 1%	660	235	14
Super Star <sup>‡</sup>	59.8	28.1	5.0	6.0	Ga, Ru, Re each < 1%	655	285	15

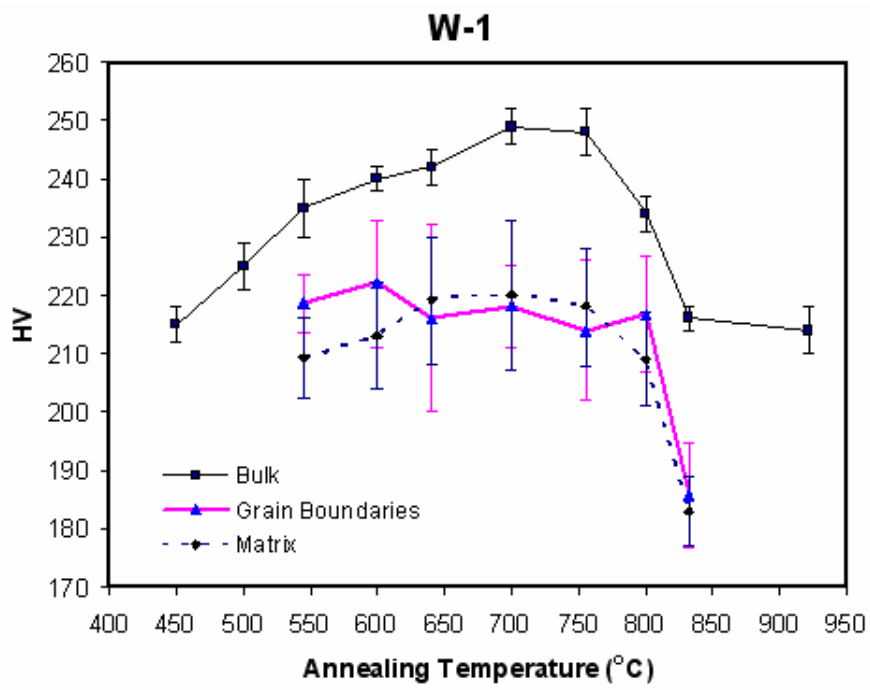
Note: Values for 0.2% yield strength, Vickers hardness and percentage elongation correspond to the simulated porcelain-firing heat-treated condition.

\*Ivoclar Vivadent, Amherst, NY, USA. (Website: [www.ivoclarvivadent.us.com](http://www.ivoclarvivadent.us.com))

<sup>†</sup>Pentron, Wallingford, CT, USA. (Website: [www.pentron.com/pentron](http://www.pentron.com/pentron))

<sup>‡</sup>Heraeus Kulzer, Armonk, NY, USA. (Website: [www.heraeus-kulzer-us.com](http://www.heraeus-kulzer-us.com))

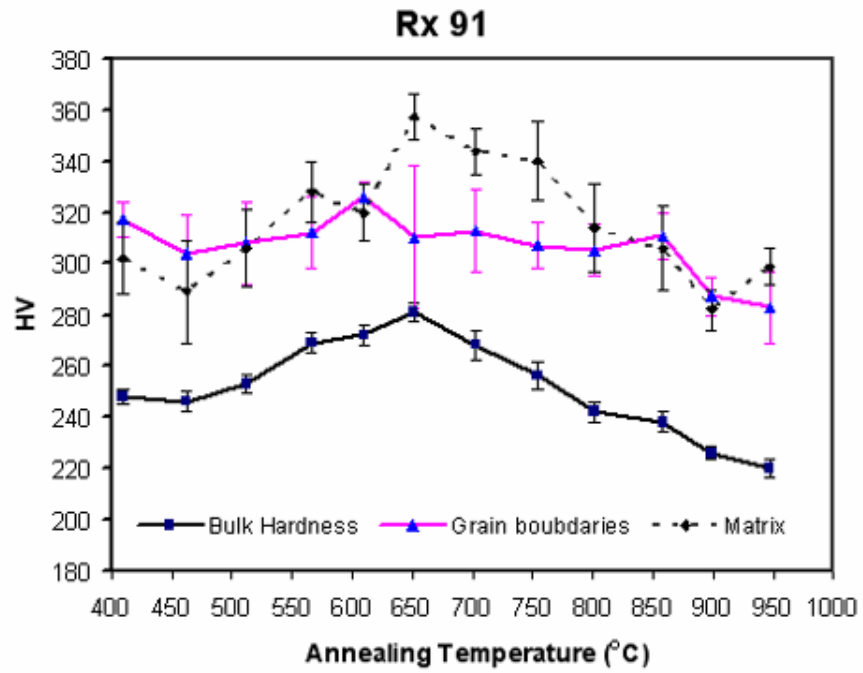
Table 4.1. Nominal compositions (wt. %) and mechanical properties reported by the manufacturers for the three Pd–Ag dental alloys studied.



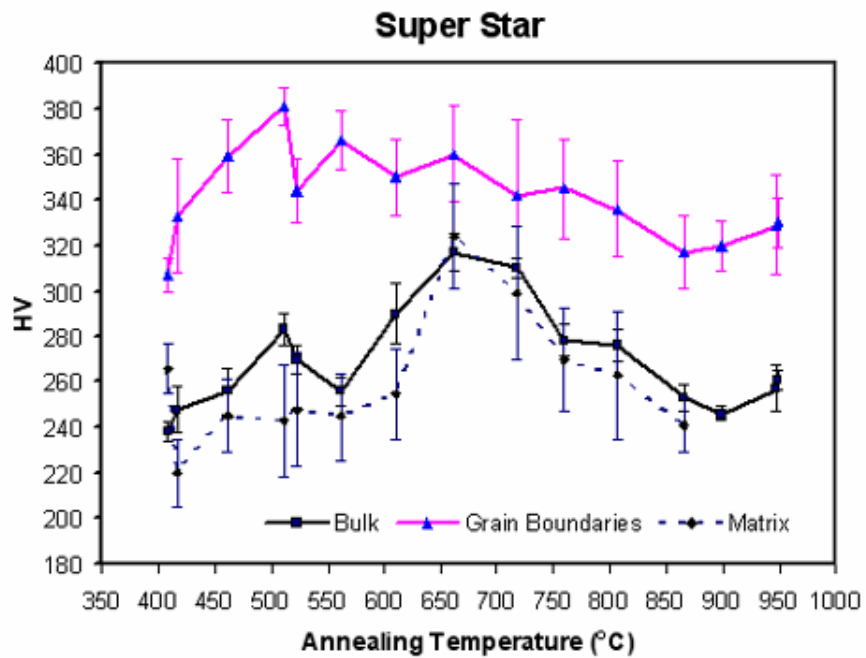
Continued

Figure 4.1. Vickers hardness as function of annealing temperature for (a) W-1, (b) Rx 91, and (c) Super Star.

Figure 4.1 continued



b



c

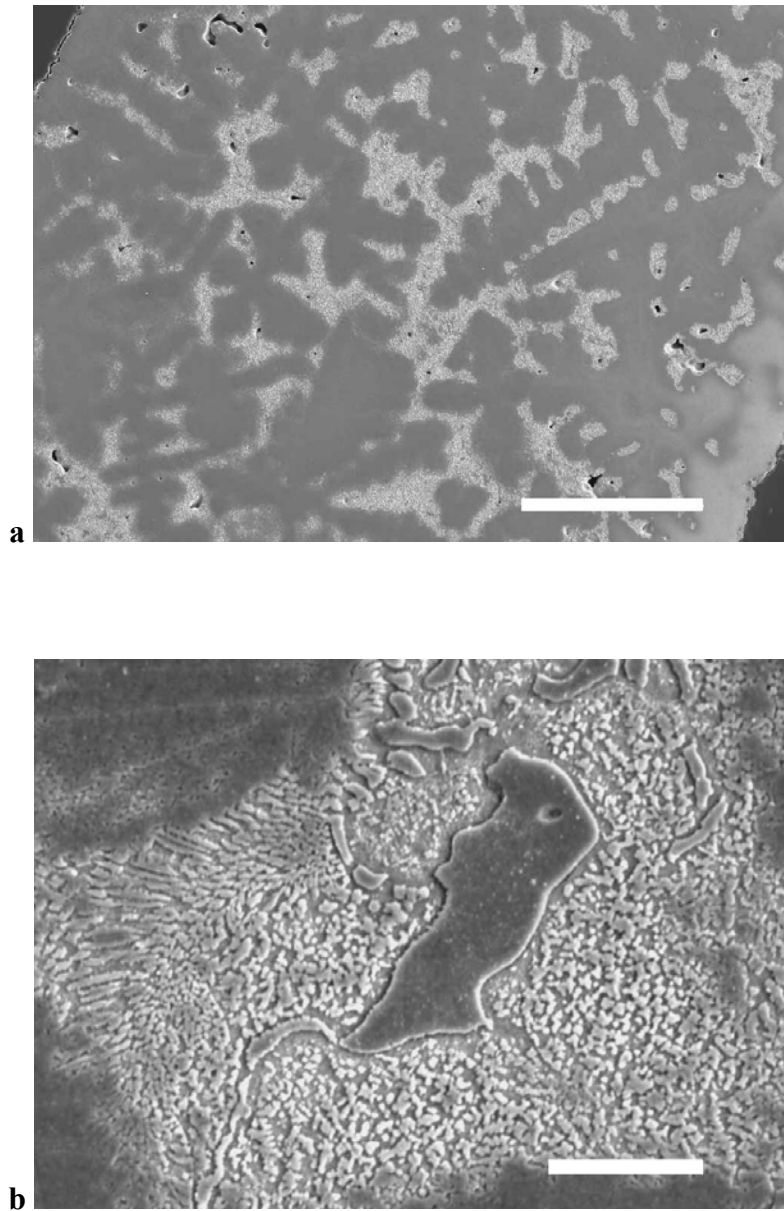
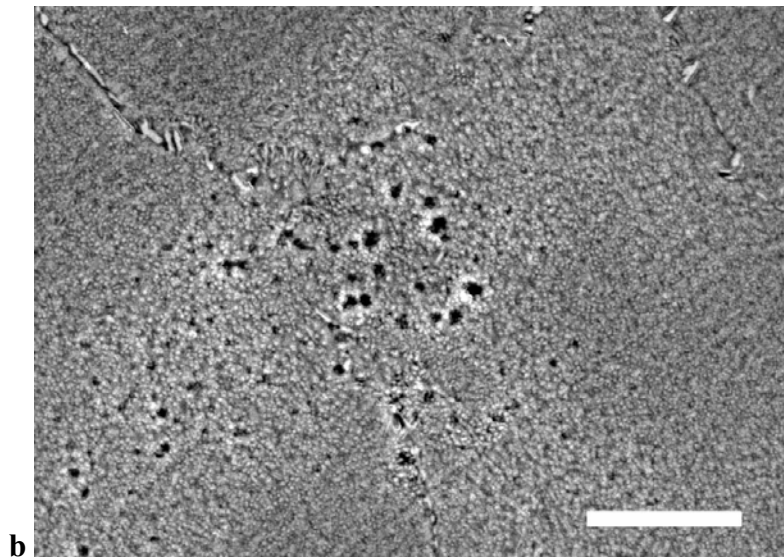
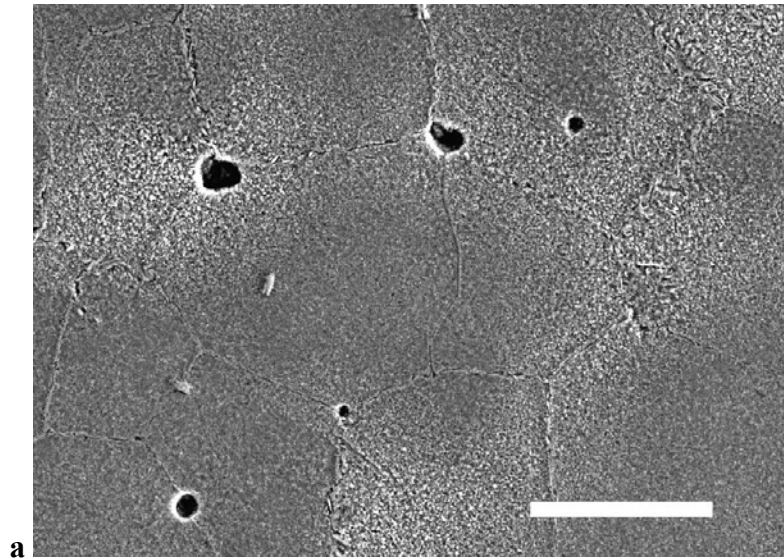


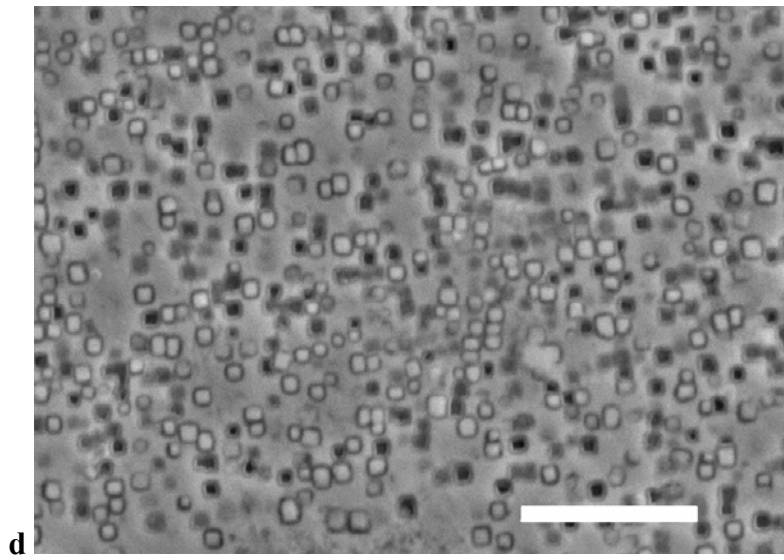
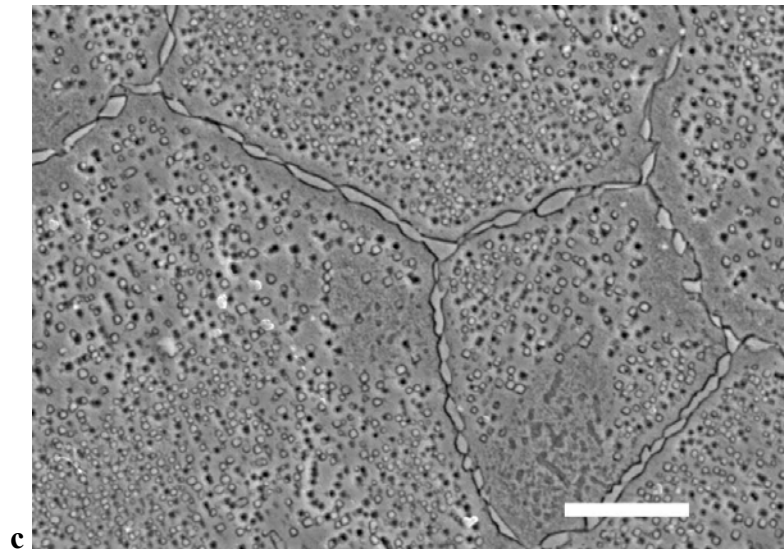
Figure 4.2. (a) SEM photomicrograph (secondary electron image) showing the dendritic structure of W-1 annealed at 922°C. (b) Higher-magnification photomicrograph of an interdendritic region, showing a multi-phase structure. Length of scale bar = 150  $\mu\text{m}$  for (a), and 5  $\mu\text{m}$  for (b).



Continued

Figure 4.3. Secondary electron images of Rx 91: (a) Annealed at 409°C, showing equiaxed grains with substructure, grain boundary precipitates, and casting porosity. (b) Annealed at 652°C, showing fine-scale porosity and precipitates in matrix and grain boundaries. (c) Annealed at 947°C, showing discontinuous precipitates in grain boundaries and adjacent matrix regions denuded of precipitates. (d) Higher-magnification photomicrograph of cube-shaped precipitates in matrix. Length of scale bar = 15  $\mu\text{m}$  for (a), 5  $\mu\text{m}$  for (b) and (c), and 3  $\mu\text{m}$  for (d).

Figure 4.3 continued



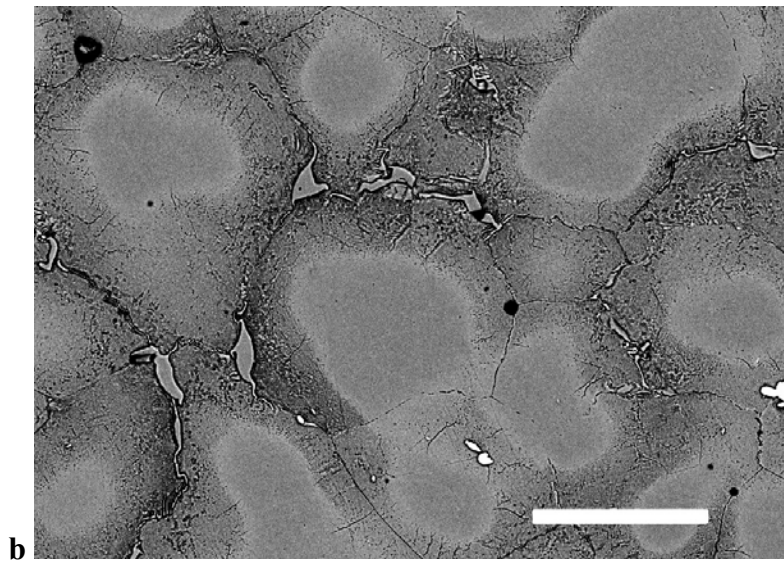
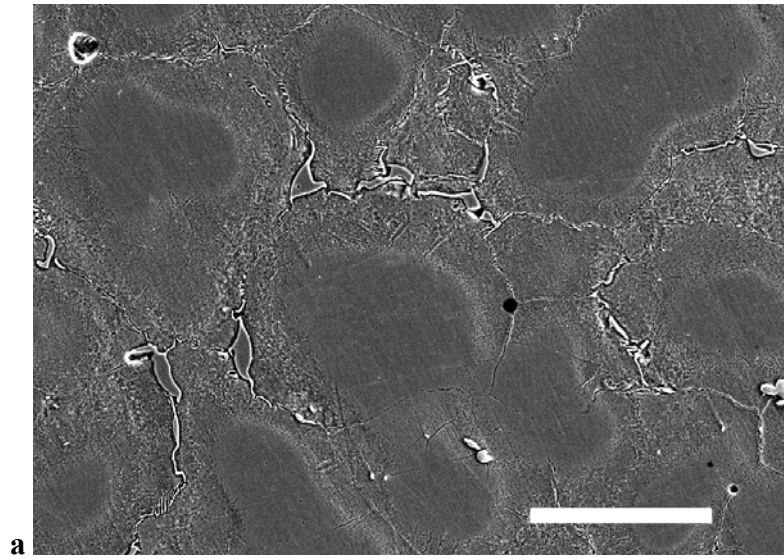


Figure 4.4. SEM photomicrographs of Super Star annealed at 417°C, showing highly segregated microstructures: (a) secondary electron image; (b) backscattered electron image. Length of scale bar = 30  $\mu\text{m}$ .

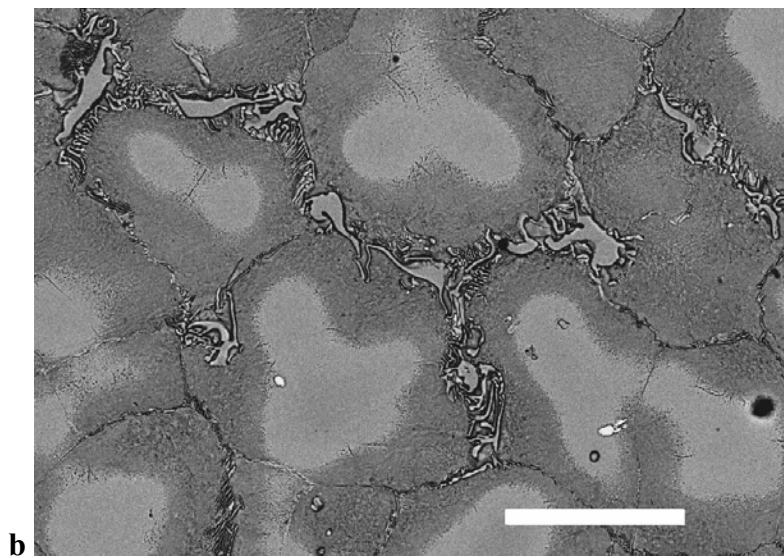
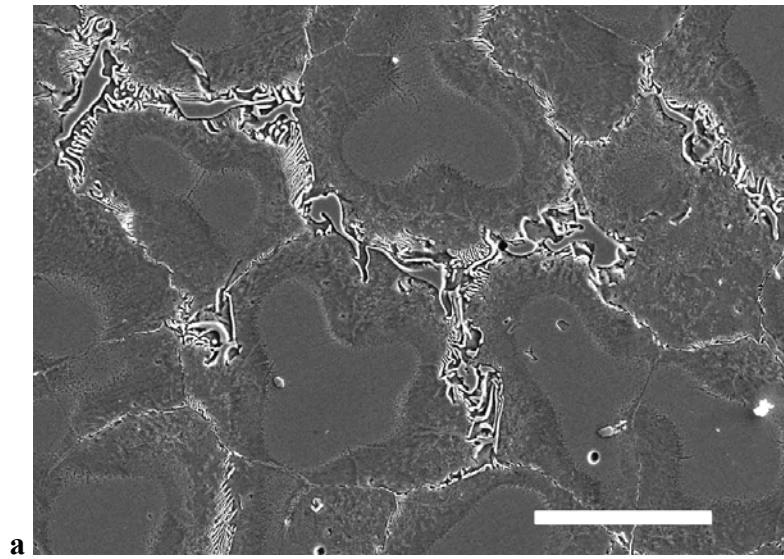
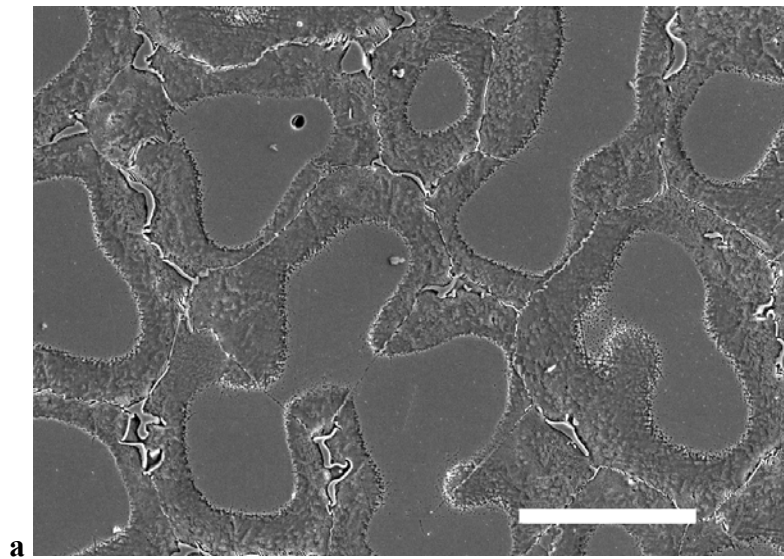


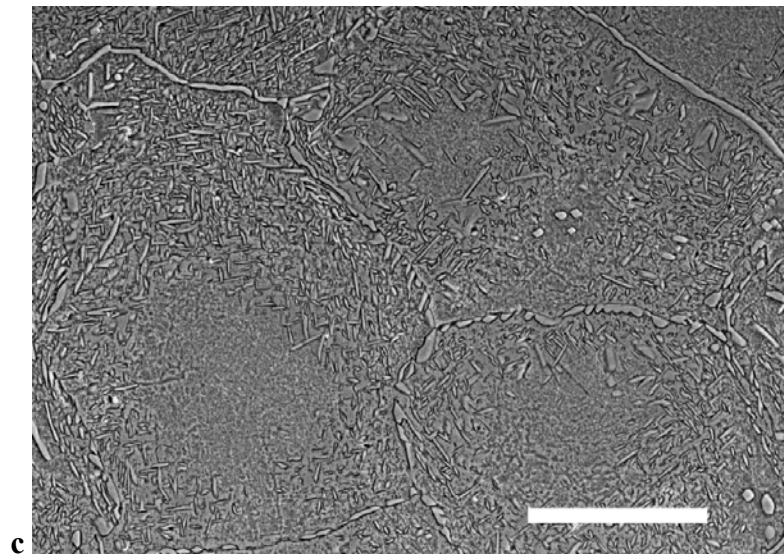
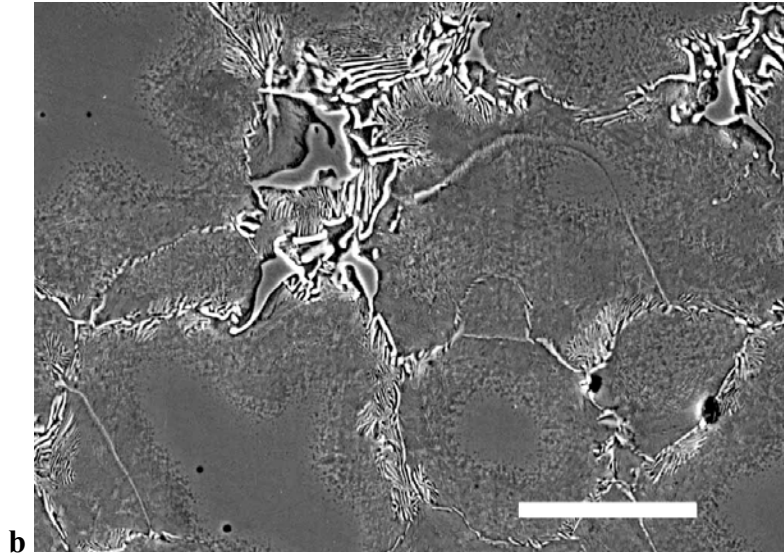
Figure 4.5. SEM photomicrographs of Super Star annealed at 512°C: (a) secondary electron image; (b) backscattered electron image. Some redistribution of component elements has taken place, compared to the Figure 4.4. Length of scale bar = 30  $\mu\text{m}$ .



Continued

Figure 4.6. SEM photomicrographs of Super Star annealed at higher temperatures: (a) 561°C; (b) 662°C; (c) 947°C. Needle-like precipitates and discontinuous precipitates appeared after annealing at 947°C. Length of scale bar = 30  $\mu\text{m}$  for (a), 10  $\mu\text{m}$  for (b), and 15  $\mu\text{m}$  for (c).

Figure 4.6 continued



## CHAPTER 5

### TRANSMISSION ELECTRON MICROSCOPIC STUDY OF PALLADIUM–SILVER DENTAL CASTING ALLOYS

#### 5.1 Introduction

The Pd–Ag dental casting alloys were introduced in 1973 as an alternative to the costly gold-based dental alloys for metal-ceramic restorations (Huget and Civjan, 1974; Goodacre, 1989). The potential problem of porcelain discoloration as a result of high silver content cited in early literature has been eliminated (Blanco-Dalmau, 1983; O'Brien *et al.*, 1998; Bertolotti, 2002). These alloys have superior mechanical properties, excellent porcelain-metal bond strength, favorable handling and soldering characteristics, and satisfactory tarnish and corrosion resistance (Bertolotti, 1983; Walton and O'Brien, 1985; Papazoglou and Brantley, 1998; Mezger *et al.*, 1989c; Bertolotti, 2002). In recent years due to the palladium price volatility, Pd–Ag alloys have attracted more interest than high-Pd alloys and become increasingly popular for metal–ceramic restorations.

The microstructures (Huget *et al.*, 1976; Payan *et al.*, 1986; Mezger *et al.*, 1989b; Vermilyea *et al.*, 1996; Pinasco *et al.*, 1999; Guo *et al.*, 2003b) and age hardening (Payan *et al.*, 1986; Hisatsune *et al.*, 1990) of Pd – Ag alloys have been studied by several investigators. When annealing between 400° and 1000°C for 1 hour, the highest hardness

of an experimental 59.3Pd–29.6Ag–8.8Sn–2.2In alloy occurred at 650°C (Payan *et al.*, 1986), and the age hardening was attributed to the internal oxidation of Sn and In previously observed by Mackert *et al.* (1983). The mechanism involved in the age hardening (prolonged up to 10<sup>5</sup> minutes) of a 55Pd–36Ag–5Sn–4In alloy (Byron; Nippon Shiken, Tokyo, Japan) was characterized by Hisatsune *et al.* (1990). They found that in the early stages of aging, a metastable ordered phase ( $\beta'$ ) with a face-centered tetragonal (fct) structure formed within the grains, and the hardening was due to the coherency strain between the metastable structure and the face-centered cubic (fcc) matrix. In the later aging stages, a lamellar structure, consisting of a stable ordered fct phase ( $\beta$ ) and a stable fcc phase, grew from the grain boundaries. These lamellae finally covered the whole grain and resulted in softening. Such a tetragonal phase was also identified by x-ray diffraction in the Pd–Ag alloy 57.9Pd–29.7Ag–5.4Sn–3.7In (Puppo Iori, Genoa, Italy) (Pinasco *et al.*, 1999), and subsequently confirmed as ordered by Guo *et al.* (2003b). In this latter study by Guo *et al.* (2003b), the microstructures of as-cast and simulated porcelain-firing heat-treated Pd–Ag alloy Super Star were characterized by transmission electron microscopy (TEM).

In the previous chapter, the annealing behavior and microstructures of W-1, Rx 91 and Super Star were described, and the highest Vickers hardness occurred at approximately 700° for W-1 and 650°C for Rx 91, while for Super Star, there were two hardness peaks at approximately 500° and 650°C. The purpose of this study was to use TEM to characterize the microstructures of these three alloys for the as-cast condition and different heat-treatment conditions.

## 5.2 Materials and Methods

Three commercial Pd–Ag alloys, W-1 (Ivoclar Vivadent, Amherst, NY), Rx 91 (Pentron, Wallingford, CT), and Super Star (Heraeus Kulzer, Armonk, NY) were used in this study. The nominal compositions of the alloys provided by the manufacturers were previously given in Table 4.1 (Chapter 4).

Sliced samples with dimensions of about 1.5 mm × 4 mm × 5mm were sectioned from simulated cast copings for a maxillary central incisor restoration, using a slow-speed water-cooled diamond saw. Preparation of the copings was previously described in Chapter 4. Heat treatment simulating the porcelain-firing cycles followed the recommendations for IPS Classic porcelain (Ivoclar Vivadent) (Guo *et al.*, 2003b), and annealing heat treatments were described in detail in Chapter 4. The slices were first ground and polished to foils with a thickness of 80 – 100 μm; then punched into disks of 3 mm diameter (suitable for the TEM specimen holder), further mechanically polished to approximately 50 μm thick, and finally ion milled (Dual Ion Mill, Model 600, Gatan, Warrendale, PA) to obtain electron transparency. Prior to TEM examination, the foils were plasma-cleaned in order to prevent possible contamination caused by ion milling. TEM examination was completed in the double-tilt stage of a Phillips CM200 TEM operating at 200 keV. Diffraction contrast imaging and both selected-area and convergent-beam electron diffraction were used to characterize the microstructures (Guo *et al.*, 2003b).

## 5.3 Results

### 5.3.1 *Microstructures of As-Cast and Simulated Porcelain-Firing Heat-Treated W-1 and Rx 91 Alloys*

TEM examination revealed that the microstructures of as-cast W-1 and Rx 91 were similar, and three different phases were observed: the solid solution matrix, granular precipitates shown in Figure 5.1a, and fine-scale fct precipitates shown in Figure 5.1b. The granular precipitates had an ordered fcc structure, as described in the next section. The size of these granular precipitates was approximately uniform. The fine-scale fct precipitates were the same as those previously observed in the Super Star Pd–Ag alloy (Guo *et al.*, 2003b), which had an ordered fct structure. After the simulated porcelain-firing heat-treatment, the fct precipitates were still present, while some smaller granular precipitates appeared, mixing with larger precipitates having a size close to that in as-cast alloys (Figure 5.2a). In W-1, many dislocations were observed inside the granular precipitates (Figure 5.2b).

### 5.3.2 *Microstructures in Rx 91 and Super Star after Annealing Heat Treatment*

In the annealing temperature range, three phases were observed in Rx 91: the matrix, the fct precipitates and the granular precipitates, which were the same as those observed in as-cast Rx 91 specimens. Figures 5.3a and 5.3c show the ordered granular fcc precipitate phase and the corresponding convergent-beam electron diffraction (CBED) diffraction image, respectively, which were taken from the Rx 91 specimen annealed at 947°C. The orientation relationship between the matrix and the ordered granular

precipitate phase was determined to be a cubic-to-cubic relation by using a series of electron diffraction patterns acquired from the matrix and an individual precipitate, as shown in Figures 5.3b and 5.3c, respectively.

The microstructure at the TEM level in Super Star after annealing is complicated. At 417°C there are two distinct phases: the solid solution matrix and the fct phase, which exist both in a eutectic structure with the matrix phase and as precipitates in the matrix, which are the same as in the as-cast microstructure (Guo *et al.*, 2003b). For annealing at 512°C, where Super Star exhibited the first hardness peak (Chapter 4), besides the same two phases as in as-cast Super Star (Guo *et al.*, 2003b) and in a specimen annealed at 417°C, new elliptical precipitates formed in the grain boundary area, as shown in Figure 5.4a. For annealing at 662°C, where Super Star showed the second hardness peak (Chapter 4), another kind of new ordered precipitates were abundant inside the grain matrix (Figure 5.4b), while the elliptical precipitates disappeared. After annealing at 947°C, although the TEM microstructure was complicated (corresponding to the SEM microstructure in Figure 4.6c), the fine-scale fct precipitates and the fct phase in grain boundary regions could be observed, as shown in Figures 5.4c and 5.4d.

## 5.4 Discussion

Although multicomponent phase diagrams relating to the Pd–Ag alloys are not available, binary phase diagrams (Okamoto, 2000) for Pd–Ag, Pd–Sn, Pd–In, Ag–Sn, and Ag–In can provide helpful hints for understanding the microstructures of Pd–Ag alloys. According to these binary phase diagrams, the microstructures of Pd–Ag alloys should be single-phase since Pd and Ag can form a continuous series of solid solutions, and the Sn

and In solubility in Pd and Ag is no less than 10%, which is higher than the Sn or In content in most commercial Pd–Ag alloys. However, as discussed in the previous chapters and in the dental materials literature, the alloys exhibited nonequilibrium or inhomogeneous microstructures even after simulated porcelain-firing heat treatment.

The Rx 91 alloy had an equiaxed microstructure while the W-1 alloy exhibited a dendritic microstructure, in which the dendrites persisted even after heat treatment (Chapter 4). Despite these differences, phases detected with the TEM for the Rx 91 and W-1 alloys were identical. This is reasonable as the two alloys have the same nominal compositions (Table 4.1) and thereby form identical phases, even though Rx 91 contains the grain-refining element ruthenium (Ru) thus has an equiaxed microstructure. The nearly spherical precipitates observed with the SEM in W-1, Rx 91 Aries and IS 64 can be considered as the result of the growth of the granular precipitates observed with the TEM. All of these alloys contain relatively less In than Super Star, d.SIGN 59, and the Pd–Ag alloys studied by Hisatsune *et al.* (1990) and Pinasco *et al.* (1999), which exhibited lamellar precipitates rather than spherical precipitates after heat treatment. It is therefore reasonable to propose that the presence of the spherical precipitates pertains to Pd–Ag alloys with lower or no indium, and that indium tends to restrain formation of this phase. Super Star showed a quite different microstructure when observed with both the SEM (Chapter 4; Vermilyea *et al.*, 1996) and TEM (Guo *et al.*, 2003b). The elliptical precipitates (Figure 5.4a) and the ordered precipitates (Figure 5.4b) in Super Star were not observed in W-1 and Rx 91, whereas the ordered fcc granular precipitates in W-1 and Rx 91 were not present in Super Star. It thus appears that these two new precipitates

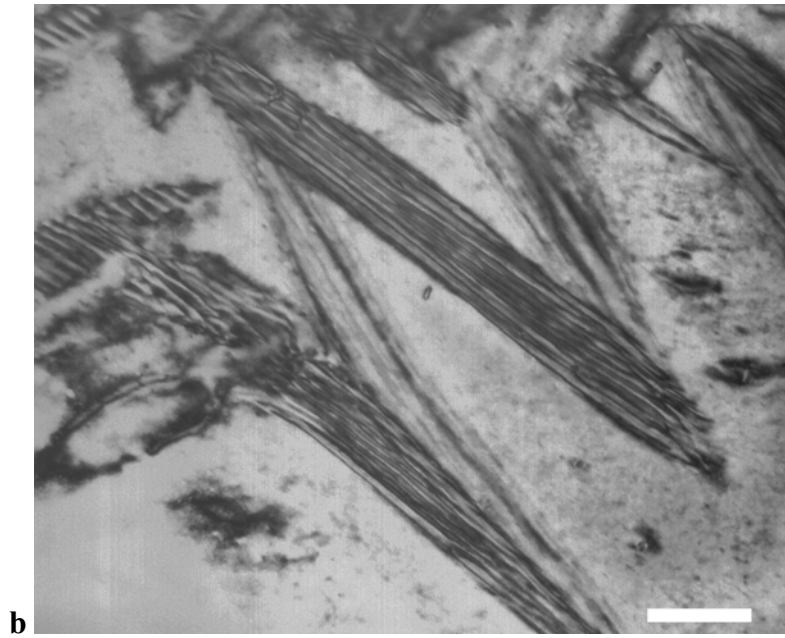
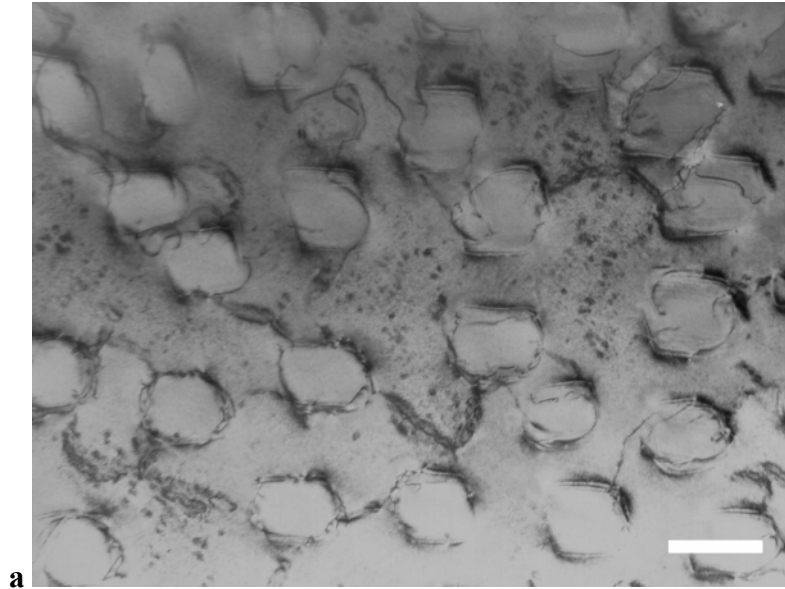
observed with the TEM and the lamellar precipitates observed with the SEM tend to form in Pd–Ag alloys with higher indium. Further study is needed to characterize the two new precipitates.

It is interesting that the tweed structure (Cai *et al.*, 1997; Nitta *et al.*, 1999) observed in high-Pd alloys were not observed in Pd–Ag alloys, whereas the fine-scale ordered fct precipitates occurred in all three Pd–Ag alloys in both as-cast and heat-treated conditions. The occurrence of ordered fine scale granular precipitates in Pd–Ag alloys with lower indium content in both the as-cast and heat-treated microstructures contribute to the hardness and mechanical properties and to the occurrence of peak age hardening for the alloys. The presence of the elliptical precipitates (Figure 5.4a) and the ordered precipitates (Figure 5.4b) in Super Star directly account for the two hardness peaks around 500° and 650°C (Figure 4.1c), respectively. The elliptical precipitates are similar in appearance to the fct phase that was associated with the age hardening peak in the Pd–Ag alloy 55Pd–36Ag–5Sn–4In investigated by Hisatsune *et al.* (1990). During plastic deformation, all such fine-scale precipitates interact with dislocations and provide precipitation hardening to the alloys. Further TEM study on the alloys after plastic deformation is necessary to investigate the detailed dislocation-precipitate interactions.

## 5.5 Conclusions

Under the conditions of this study, the following conclusions can be drawn:

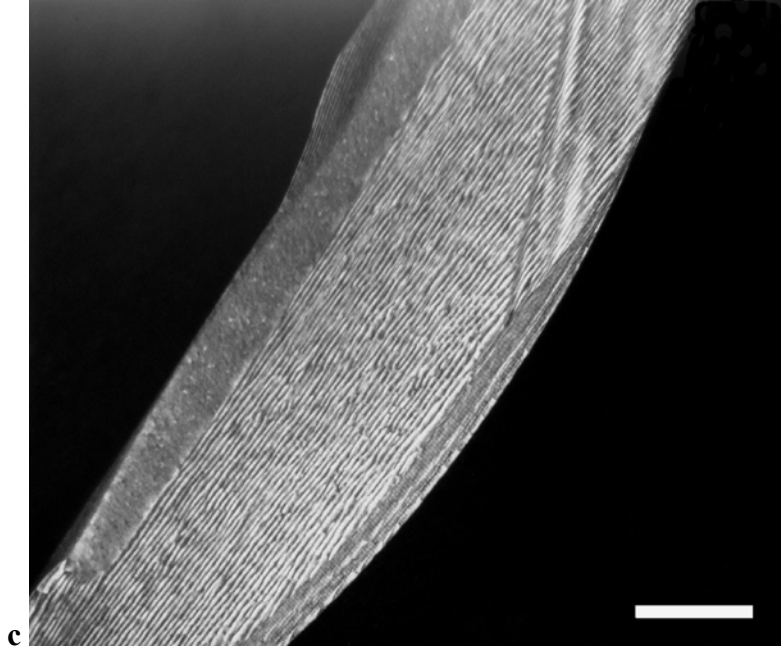
1. The TEM microstructures of the as-cast Pd–Ag alloys W-1 and Rx 91 were similar. Three different phases were observed: the solid solution matrix, granular precipitates, and fine-scale precipitates. The granular precipitates had an ordered fcc structure with a cubic-cubic orientation with the fcc solid solution matrix. The fine-scale fct precipitates had an ordered fct structure. After simulated porcelain-firing heat-treatment, besides the fct precipitates and granular precipitates with a similar size as in the as-cast condition, some smaller granular precipitates also appeared. Many dislocations were observed inside the granular precipitates in heat-treated W-1.
2. In the annealing temperature range, Rx 91 exhibited the same TEM microstructure as in the as-cast condition. Super Star, however, has a complicated TEM microstructure. At 417°C, the microstructure for Super Star consisted of two distinct phases as in the as-cast condition: the matrix and the fct phase. With increased annealing temperature, besides these two phases, new elliptical precipitates formed in the grain boundary region after annealing at 512°C, causing the first age hardening peak of the alloy. Other new ordered precipitates were abundant inside the matrix after annealing at 662°C, which accounted for the second age hardening peak, while the elliptical precipitates disappeared. The TEM microstructure after annealing at 947°C was complicated, and the fine-scale fct precipitates still persisted as well.



Continued

Figure 5.1. TEM micrographs of as-cast Rx 91: (a) granular precipitates (length of scale bar = 200 nm); (b) fine-scale fct precipitates (length of scale bar = 50 nm); (c) dark-field image showing striations in grain boundary fct phase (length of scale bar = 100 nm).

Figure 5.1 continued



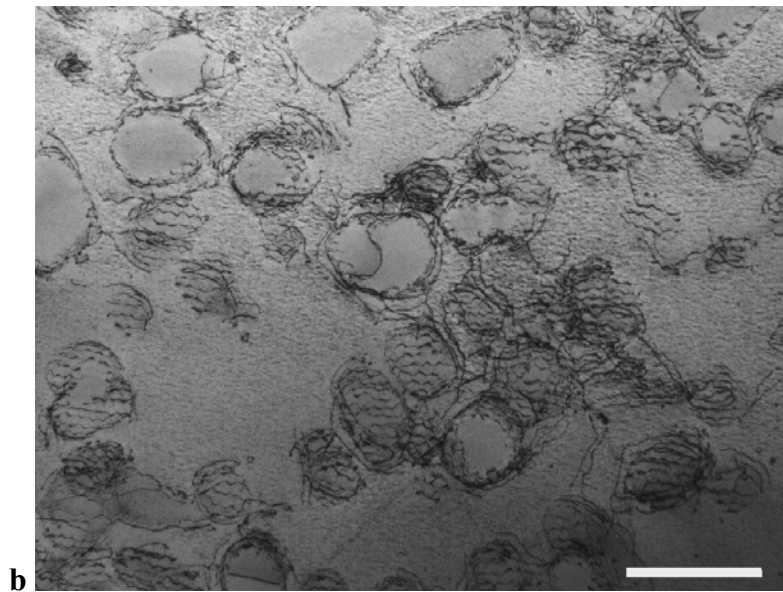
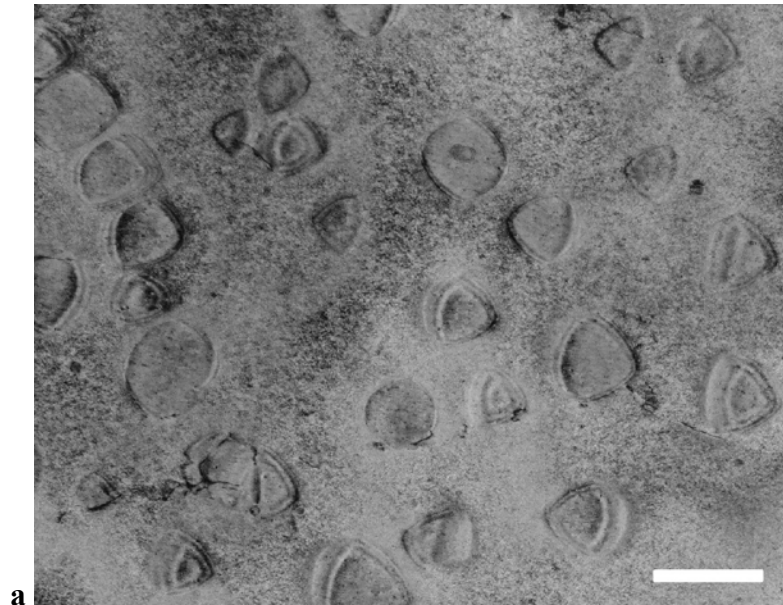
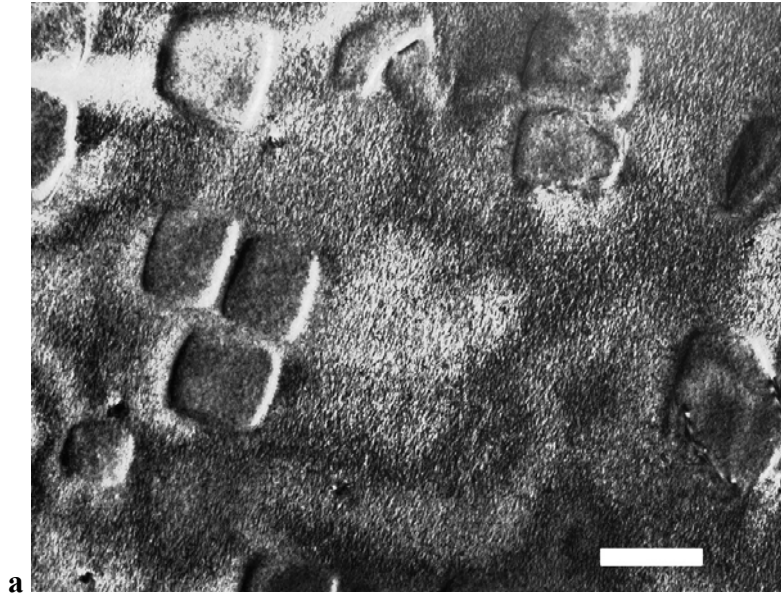


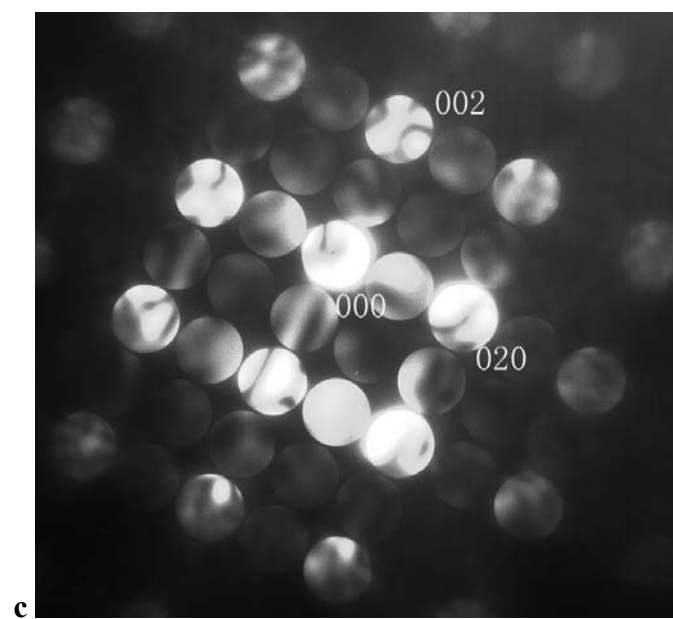
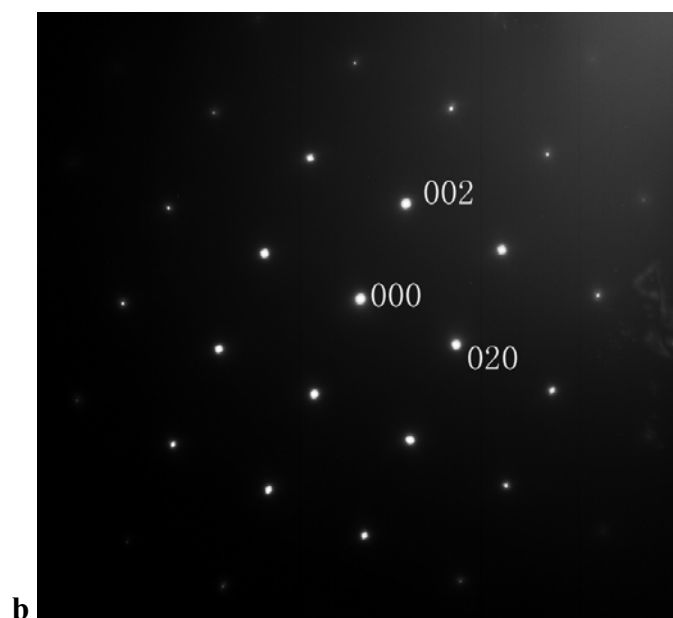
Figure 5.2. TEM micrographs in simulated porcelain firing heat-treated W-1: (a) granular precipitates with different sizes (length of scale bar = 200 nm); (b) dislocations inside granular precipitates (length of scale bar = 500 nm).

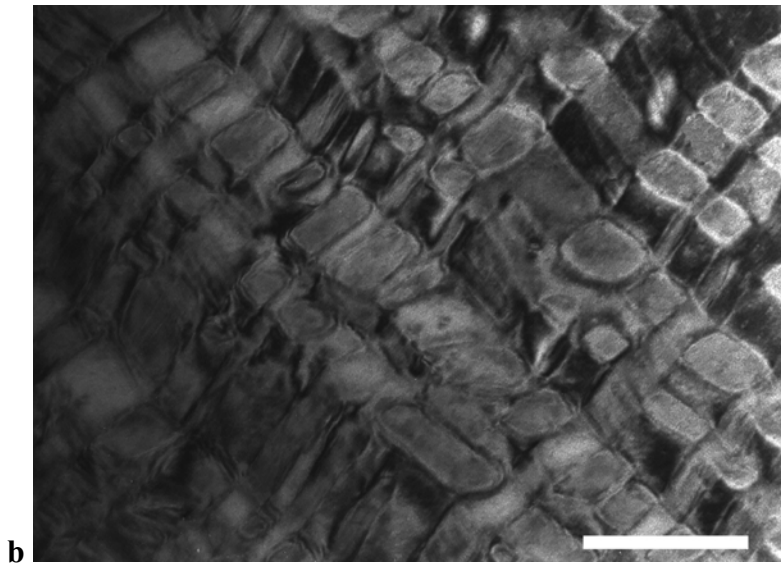
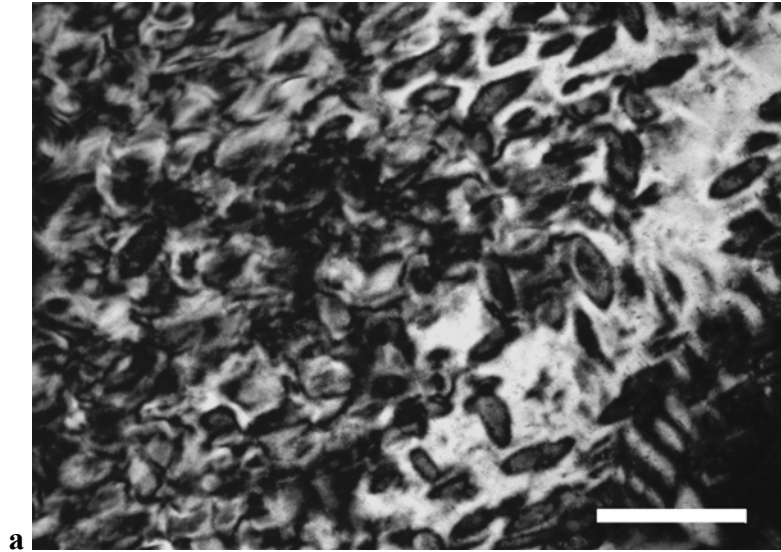


Continued

Figure 5.3. TEM micrograph and electron diffraction patterns showing cubic-cubic orientation between the matrix and the granular precipitate phase in Rx 91 after annealing at 947°C: (a) dark-field image of the granular precipitates (length of scale bar = 200 nm); (b) selected-area electron diffraction pattern (SADP) of palladium solid solution matrix,  $\mathbf{B} = [100]$ ; (c) Convergent-beam electron diffraction pattern of a granular precipitate with the same condition as in (b).  $\mathbf{B} = [100]$ .

Figure 5.3 continued

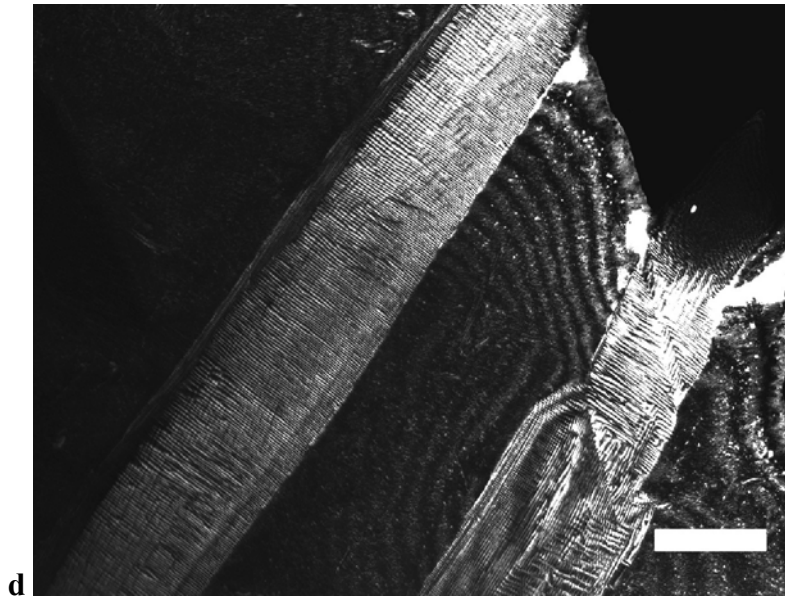
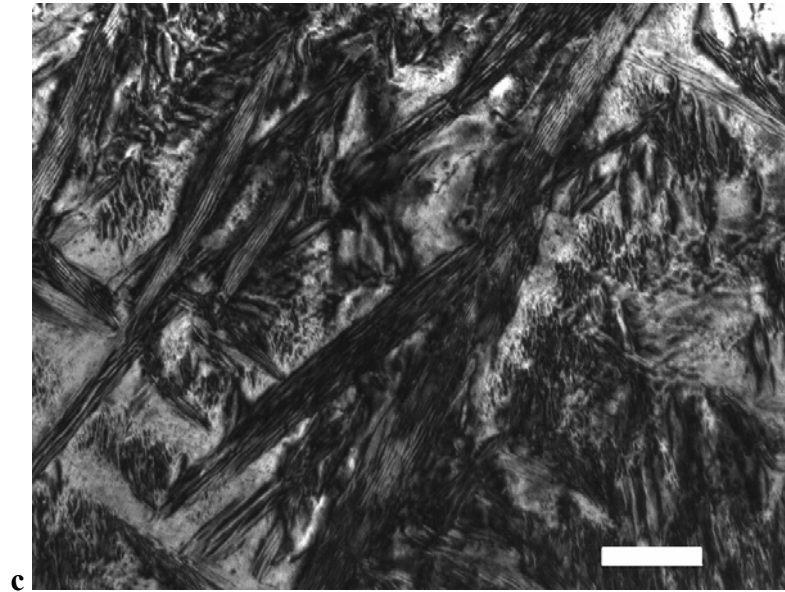




Continued

Figure 5.4. TEM micrographs showing the microstructures in Super Star after annealing at different temperatures: (a) elliptical precipitates after annealing at 512°C (length of scale bar = 200 nm); (b) ordered precipitates after annealing at 662°C (length of scale bar = 100 nm); (c) fine-scale fct precipitates in grains after annealing at 947°C (length of scale bar = 100 nm); (d) fct phase in grain boundary region after annealing at 947°C (length of scale bar = 200 nm).

Figure 5.4 continued



## CHAPTER 6

### FATIGUE LIMITS AND SEM/TEM OBSERVATIONS OF FRACTURE CHARACTERISTICS FOR Pd–Ag ALLOYS

#### 6.1 Introduction

Palladium–silver (Pd–Ag) dental casting alloys were introduced in the early 1970s as an economic alternative to gold casting alloys for metal-ceramic restorations (Huget and Civjan, 1974; Bertolotti, 1984; Goodacre, 1989) and have achieved widespread clinical popularity. These alloys are also used for the superstructures of dental implants. The Pd–Ag alloys usually contain between 50% and 60% Pd and 30% to 40% Ag (wt. %), with small amounts of low melting point metals, In and Sn, which promote strong bonding to dental porcelain and may improve castability by increasing molten metal fluidity. These alloys have a high elastic modulus which provides rigidity for multi-unit castings, high sag resistance during the porcelain firing cycles, excellent porcelain-metal bond strength, favorable handling and soldering characteristics, and satisfactory tarnish and corrosion resistance (Huget and Civjan, 1974; Huget *et al.*, 1976; Myers and Cruickshanks-boyd, 1982; Bertolotti, 1984; Mezger *et al.*, 1986; Reel *et al.*, 1986; Goodacre, 1989; Mezger *et al.*, 1989a; Papazoglou and Brantley, 1998; Pinasco *et al.*,

2000; Brantley and Laub, 2001; Bertolotti, 2002). The Pd content is much lower in the Pd–Ag alloys than in the high-Pd dental alloys, and the former have become more attractive for clinical selection because of the recent Pd price volatility.

The main problem for clinical selection of Pd–Ag alloys has been their tendency to cause porcelain discoloration, which varies among different brands of dental porcelain. This problem has been alleviated or eliminated by proper melting and casting of these alloys, and selection of particular brands of porcelain (Lacy *et al.*, 1977; Bertolotti, 1984; Bertolotti, 1988; Goodacre, 1989; O’Brien *et al.*, 1998; Brantley and Laub, 2001). Other approaches to prevent porcelain discoloration have included the use of coating agents and the incorporation of certain elements in the alloy composition (Ringle *et al.*, 1986; Bertolotti, 1988).

Fatigue is a fracture mode in which a metallic component fails after being subjected to repeated stresses that are substantially below its yield strength (Dieter, 1986; Dowling, 1993). While there appears to be some clinical evidence that the failures of cast dental alloys *in vivo* can be related to cyclic fatigue rather than to an episode of acute overload (Anselm *et al.*, 1995), little published information is available on their fatigue properties. In previous studies, the fatigue limits and fracture characteristics for two high-Pd alloys, a Pd–Cu–Ga alloy and a Pd–Ga alloy not containing copper, were reported (Li *et al.*, 2002; Guo *et al.*, 2002). The purpose of the present study was to investigate the fatigue behavior of three commercial Pd–Ag dental alloys; such information has not been previously reported.

## 6.2 Materials and Methods

The Pd–Ag dental alloys selected for study were Super Star (Heraeus Kulzer, Armonk, NY), Rx 91 (Pentron, Wallingford, CT) and W-1 (Ivoclar Vivadent, Amherst, NY). The nominal compositions and mechanical properties provided by the manufacturers are given in Tables 4.1 and 6.1.

Procedures for preparing the cast specimens, performing the fatigue experiments, and examining the fractured specimens with the scanning electron microscope (SEM) and transmission electron microscope (TEM) were the same as in recent studies (Li *et al.*, 2002; Guo *et al.*, 2002). The alloys were melted using a gas-air torch and cast into tensile test bars having gauge diameter of 3 mm and gauge length of 15 mm (ANSI/ADA, 1997; ANSI/ADA, 2000). Polystyrene patterns (Salco, Romeoville, IL) (Bridgeport *et al.*, 1993) conforming to these dimensions were invested in a carbon-free phosphate-bonded investment (Cera-Fina, Whip-Mix, Louisville, KY). Two specimens of each alloy were cast for each fatigue stress amplitude and bench-cooled to room temperature, as recommended by the manufacturer. Sprues were cut from the cast specimens with a carborundum disk, and any visible nodules were removed.

Specimens in the as-cast surface condition, without subsequent air-abrasion or polishing, were subjected to heat treatment in a conventional dental porcelain furnace (Ultra-Mat CDF, 3M Unitek, Monrovia, CA) that simulated the porcelain-firing cycles. The initial oxidation step followed the instructions of each alloy manufacturer, and the subsequent firing cycles followed the recommendations for IPS Classic porcelain (Ivoclar

Vivadent). For the W-1 alloy only, a special hardening heat treatment at 650°C indicated by the manufacturer was performed before the simulated heat treatment cycles for porcelain application.

Calculations of loads required to produce the desired stress amplitudes for fatigue testing were based on the values of yield strength (YS) for 0.2% permanent tensile strain ( $\sigma_{0.2}$ ) provided by the manufacturers for the alloys in the heat-treated condition for porcelain bonding (Table 6.1): 655 MPa for Super Star, 660 MPa for Rx 91, and 605 MPa for W-1 (hardening heat treatment). Measurement of the 0.2% YS is stipulated in the specification for metal-ceramic systems (ANSI/ADA, 2000), in which a minimum value of 250 MPa is required for a ceramic alloy.

Fatigue tests were carried out in air at room temperature using uniaxial sinusoidal tension-compression loading (Model 1322, Instron Corp., Canton, MA). The ratio (R-ratio) between the compressive and tensile stress amplitudes was  $-1$ , and the frequency was 10 Hz. Selection of the starting stress amplitude ( $0.20\sigma_{0.2}$ ) was based on previous experience with dental high-Pd casting alloys (Li *et al.*, 2002), which resulted in considerably fewer specimens than with the conventional staircase method (ASTM, 1963; Collins, 1993). Two replicate specimens were tested at each stress amplitude, and the amplitude at which fracture did not occur after  $2 \times 10^6$  cycles was designated as the fatigue limit. This number of cycles provided clinical relevance (Anselm *et al.*, 1995), without unduly prolonging the testing period.

After ultrasonic cleaning in ethanol, the surfaces of the fatigued specimens were examined with an SEM (JSM-820, JEOL Ltd, Tokyo, Japan) over a range of magnifications. Microstructural observations were carried out with the same SEM on flat

samples sectioned from the fractured bars by a slow-speed water-cooled diamond saw, and mounted in transparent metallographic epoxy resin (Leco, St. Joseph, MI). After grinding with 320, 400, and 600 grit silicon carbide papers and polishing with a series of Al<sub>2</sub>O<sub>3</sub> slurries ending with 0.05 μm particles, specimens were etched in aqua regia solutions to reveal their microstructures.

Specimens that fractured during the fatigue test were also examined by TEM (Philips CM 200, Eindhoven, The Netherlands). Regions near the fracture surface were cut from the fatigued specimen using the same low-speed, water-cooled diamond saw. These slices were mechanically ground to a thickness of about 100 μm and punched to form approximately 3 mm diameter disks, which were dimpled using 1 μm and 0.5 μm diamond gels to a thickness of 30 – 40 μm. These resulting foils were further thinned to electron transparency using an argon ion miller, and their surfaces were plasma-cleaned to eliminate any preparation artifacts. The TEM observations were performed over a range of magnifications at an operating voltage of 200 keV.

## **6.3. Results**

### **6.3.1 *Microstructures and Fatigue Limits of Pd - Ag Alloys***

As-cast Rx 91 had an equiaxed fine-grain microstructure, while as-cast W-1 had a dendritic microstructure. As-cast Super Star had inhomogeneous, equiaxed, grain-like regions with a dendritic character that was previously reported (Vermilyea *et al.*, 1986). These general microstructures were maintained after simulated porcelain-firing heat treatment, as shown in Figure 6.1a, b and c, and spherical precipitates were observed in the Pd solid solution matrix of all three alloys. Discontinuous precipitates also appeared

in the grain boundaries of Super Star and Rx 91 and in the dendritic structure of W-1 after the heat treatment. Little porosity was observed in the three Pd–Ag alloys, which was similar to previous results for cast high-Pd dental alloys (Li *et al.*, 2002; Papazoglou *et al.*, 1999; Papazoglou *et al.*, 2000), although there were areas of each specimen with more substantial porosity. Table 6.2 shows the number of cycles for failure at different stress amplitudes and that the fatigue strength of Super Star, Rx 91 and W-1 for the heat-treated condition is approximately 15% of the 0.2% offset yield strength ( $\sigma_{0.2}$ ).

### **6.3.2 Fracture and Microstructural Characteristics of Fatigued Pd – Ag Alloys**

#### **6.3.2.1 SEM Characterization of the Fatigue Fracture Surface**

SEM observations showed that the fatigue crack responsible for failure initiated either at the surface or inside the specimens, although it was usually impossible to determine unambiguously the actual site of initiation. Figure 6.2 shows an apparent dendritic structure, within which incomplete solidification resulted in an absence of interdendritic regions, around the crack initiation region on the surface of one fatigued Super Star specimen.

Fine-scale fatigue striations similar to those for high-Pd dental alloys (Li *et al.*, 2002) were observed on the fracture surfaces of all three Pd–Ag alloys, as shown in Figure 6.3a, b and c, and many secondary cracks were also observed along these striations. For Super Star, some variation in the orientation of these striations was observed, as shown in Figure 6.3a. Terraced patterns of striations were observed for all three Pd–Ag alloys, with the striations superimposed on coarser features; these features and the fatigue striations were approximately perpendicular to each other, as shown in Figure 6.4a and b.

### **6.3.2.2 TEM Characterization of Fatigued Pd–Ag Alloys**

TEM observation revealed networks of tangled dislocations and stress-induced slip bands in fatigued specimens of all three alloys (Figure 6.5), indicating the role of dislocation motion in the cyclic deformation process. Interactions between dislocations and the spherical precipitates, and dislocation networks in the interfaces between the precipitates and the surrounding matrix, were also observed (Figure 6.6) and attributed to the effect of cyclic deformation. Twinning was also observed in the palladium solid solution matrix of Rx 91 (Figure 6.6), and in the discontinuous precipitates in Super Star and Rx 91 (Figure 6.7).

## **6.4 Discussion**

The fatigue limit, which provides quantitative information about resistance of an alloy to failure by cyclic loading, is dependent upon the composition, microstructure, and numerous testing variables. These include the nature of the cyclic loading (*e.g.*, axial as in the present investigation, bending, or torsion), the stress amplitude, R-ratio, specimen size and shape, and the designated number of loading cycles corresponding to use conditions (Dieter, 1986; Dowling, 1993). A fatigue limit is meaningful only when all of these testing variables are specified, and comparisons of fatigue limits for different alloys are usually applicable only when the data are acquired under the same testing conditions. At present there are no American National Standards Institute/American Dental Association or ISO (International Office for Standardization) specifications or widely accepted protocols for fatigue testing of dental casting alloys.

The fatigue limit to yield strength ( $\sigma_{0.2}$ ) ratio for the three Pd–Ag alloys (Table 6.2) is similar to that for two high-Pd alloys tested under the same conditions (Li *et al.*, 2002). In this previous study, the ratio of fatigue limit to yield strength of approximately 0.15 – 0.20 for two high-Pd alloys was calculated for the value of YS at 0.1% permanent tensile strain ( $\sigma_{0.1}$ ). Recalculation of this ratio for the two high-Pd alloys using the  $\sigma_{0.2}$  value for yield strength only causes a minor change in the ratio to a new range of 0.15 – 0.20, which has little meaning given the accuracy of the experimental measurements involved. For example, the values of stress amplitude in Table 6.2 have rounded to the nearest  $0.05\sigma_{0.2}$ , which is consistent with the approximate  $\sigma_{0.2}$  values reported by the manufacturers to the nearest 5 MPa (Table 6.1). Table 6.2 shows that there is a steep dependence of the number of fatigue cycles to failure on the stress amplitude ( $\sigma_{0.2}$ ), and the results for Rx 91 suggest that its fatigue limit may be closer to  $0.15\sigma_{0.2}$  than  $0.10\sigma_{0.2}$ . Consequently, the fatigue limit for the three Pd–Ag alloys is approximately  $0.15\sigma_{0.2}$  for cast test specimens of the dimensions used in this study.

In a previous study on fatigue of high-Pd alloys (Li *et al.*, 2002), it was noted that the low ratio of fatigue limit to yield strength might be attributed to casting or microstructural defects in the cast specimens. Since casting defects cannot be completely eliminated from practical casting processes (Anusavice, 1996; Mizumoto *et al.*, 2003), characterization of these defects (bulk porosity and surface flaws) and in the fatigue test specimens and their effects on fatigue properties are important areas for further investigation. In addition, the fatigue performances of castings with dimensions closer to those of single-tooth metal-ceramic restorations need to be determined. For such smaller

test specimens and for the metal components of single-tooth metal-ceramic restorations, the results in Table 6.2 should be considered as conservative, lower-limit values of the fatigue limit for these alloys.

After the simulated porcelain-firing heat treatment, values of the nominal yield strength ( $\sigma_{0.2}$ ) for Super Star, Rx 91 and W-1 are similar, using the value for W-1 after the hardening heat treatment (Table 6.1), and values for percentage elongation and Vickers hardness for these three Pd–Ag alloys are also similar. Small differences in these mechanical properties arise from differences in the alloy compositions (Table 4.1) and microstructures. For example, the lower percentage elongation for W-1, compared to Super Star and Rx 91, might be associated with differences in the dendritic structures of the three alloys, which would result in differences in the general paths for crack propagation through the interdendritic regions. In a previous study, a high-Pd alloy with a dendritic as-cast microstructure (Spartan Plus, Ivoclar Vivadent) had considerably greater percentage elongation after heat treatment simulating the porcelain firing cycles, which eliminated the as-cast dendritic microstructure (Papazoglou *et al.*, 2000).

The results in Table 6.2 thus suggest that under the conditions of the present study the fatigue limit is not greatly affected by whether the alloy has a dendritic or equiaxed fine-grained microstructure, or a combination of both types of microstructural constituents. The major factor for the maximum load at which fatigue failure does not occur for the Pd–Ag alloys (Table 6.2) is the yield strength, which is dependent upon the strengthening mechanisms for these alloys. Studies of these mechanisms will be reported in separate manuscripts that describe TEM observations of the annealed alloys.

Since dislocations tangles and stress-induced slip bands were observed by TEM in all three fatigued alloys (Figure 6.5), slip was a common mode of permanent deformation. In addition, twinning was observed in the Pd solid solution matrix of fatigued Rx 91 (Figure 6.6), and in the discontinuous precipitates (Figure 6.6) in fatigued Super Star and Rx 91, indicating that twinning was an additional mode of permanent deformation for these alloys. In previous studies (Li *et al.*, 2002; Guo *et al.*, 2002), the Pd–Cu–Ga alloy in which twinning was the main permanent deformation mode had superior fatigue resistance to the Pd–Ga alloy where such twinning was not observed. Therefore, the occurrence of twinning to relieve local stress concentrations during fatigue deformation may be beneficial to fatigue performance.

## **6.5 Conclusions**

The fatigue limits of three Pd–Ag alloys, Super Star, Rx 91 and W-1, were investigated using uniaxial tension-compression loading with a stress amplitude ratio of  $R = -1$ . The microstructural and fracture characteristics of the fatigued specimens were analyzed by SEM and TEM. The following conclusions can be drawn from this study:

1. The fatigue limit (for  $2 \times 10^6$  cycles) of the Super Star, Rx 91 and W-1 alloys was approximately 15% of the 0.2% offset yield strength in tension. The specimens had the original as-cast surface condition and were heat-treated to simulate the clinical firing cycles for dental porcelain.
2. The fatigue properties of the W-1 and Super Star alloys were not adversely affected by their dendritic microstructures, which had distinctly different character in the two alloys, that existed after the simulated porcelain-firing heat treatment.

3. During fatigue, slip in the Pd solid solution matrix is a common permanent deformation mechanism for all the three Pd–Ag alloys. Twinning provides an additional permanent deformation mode for Super Star and Rx 91.

Alloy	Elastic Modulus (GPa)	$\sigma_{0.2}$ (MPa)	Percentage Elongation (%)	Vickers Hardness
Super Star*	130	655	15	285
Rx 91 <sup>†</sup>	130	660	14	235
W-1 <sup>‡</sup>	— <sup>¶</sup>	485	11	240

605 (hardening heat treatment)

\* Heraeus Kulzer, Armonk, NY, USA. [Website: [www.heraeus-kulzer-us.com](http://www.heraeus-kulzer-us.com)]

<sup>†</sup> Pentron, Wallingford, CT, USA. [Website: [www.pentron.com](http://www.pentron.com)]

<sup>‡</sup> Ivoclar Vivadent, Amherst, NY, USA. [Website: [www.ivoclarvivadent.us.com](http://www.ivoclarvivadent.us.com)]

<sup>¶</sup> Not reported.

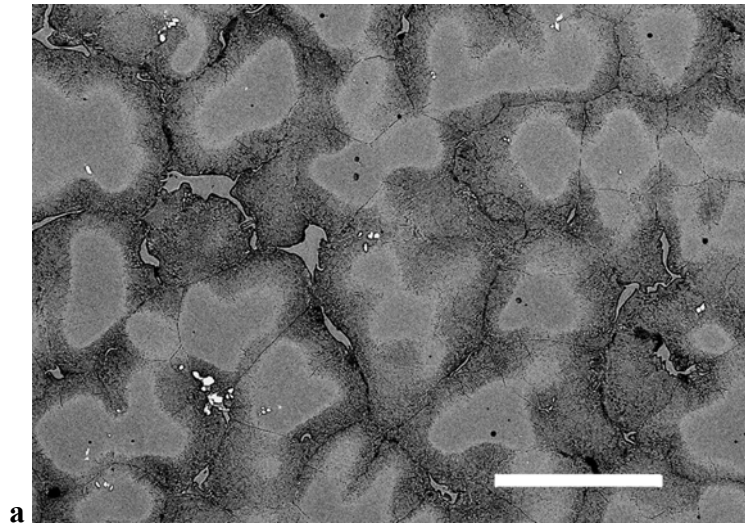
Table 6.1. Nominal mechanical properties for Super Star, Rx 91, and W-1 Pd–Ag dental alloys provided by manufacturers (after heat treatment for porcelain application).

Specimen No.	Alloy	Stress* (Load, N)	Fatigue Cycles
1	Super Star	$0.20\sigma_{0.2}$ (926)	350,292
2		$0.20\sigma_{0.2}$ (926)	715,875
3		$0.15\sigma_{0.2}$ (695)	1,516,640
4		$0.15\sigma_{0.2}$ (695)	>2,000,000
5	Rx 91	$0.15\sigma_{0.2}$ (700)	983,905
6		$0.15\sigma_{0.2}$ (700)	1,226,010
7		$0.10\sigma_{0.2}$ (467)	>2,000,000
8		$0.10\sigma_{0.2}$ (467)	>2,000,000
9	W-1 <sup>†</sup>	$0.20\sigma_{0.2}$ (855)	907,330
10		$0.20\sigma_{0.2}$ (855)	183,210
11		$0.15\sigma_{0.2}$ (642)	659,555
12		$0.15\sigma_{0.2}$ (642)	>2,000,000

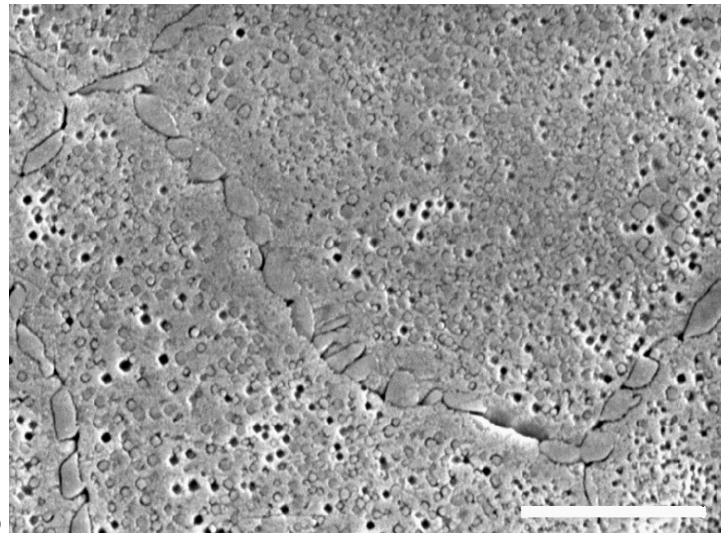
\* Values of stress have been rounded to the nearest  $0.05\sigma_{0.2}$ .

<sup>†</sup> Values of stress are based upon a value of 605 MPa for  $\sigma_{0.2}$  (Table 6.1).

Table 6.2. Fatigue cycles to failure for Super Star, Rx 91, and W-1



**a**

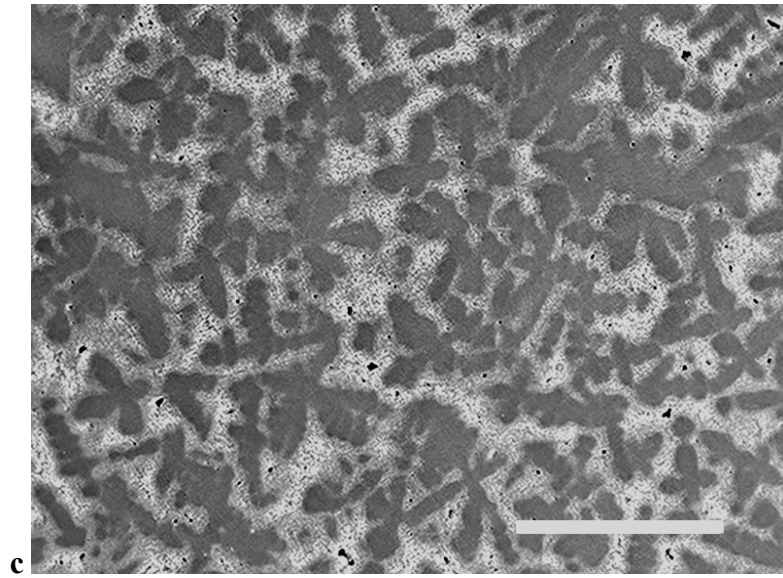


**b**

Continued

Figure 6.1. SEM images of heat-treated (a) Super Star (scale bar length = 50  $\mu\text{m}$ ), (b) Rx 91 (scale bar length = 4  $\mu\text{m}$ ), and (c) W-1 (scale bar length = 300  $\mu\text{m}$ ). (a) is a backscattered electron image, and (b) and (c) are secondary electron images. The as-cast dendritic character of W-1 is maintained after the porcelain-firing heat treatment. The inhomogeneous compositions of the equiaxed regions with dendritic character in Super Star are evident in the backscattered electron image. The higher-magnification photomicrograph of Rx 91 shows the discontinuous grain boundary precipitates and the etching pattern within grains.

Figure 6.1 continued



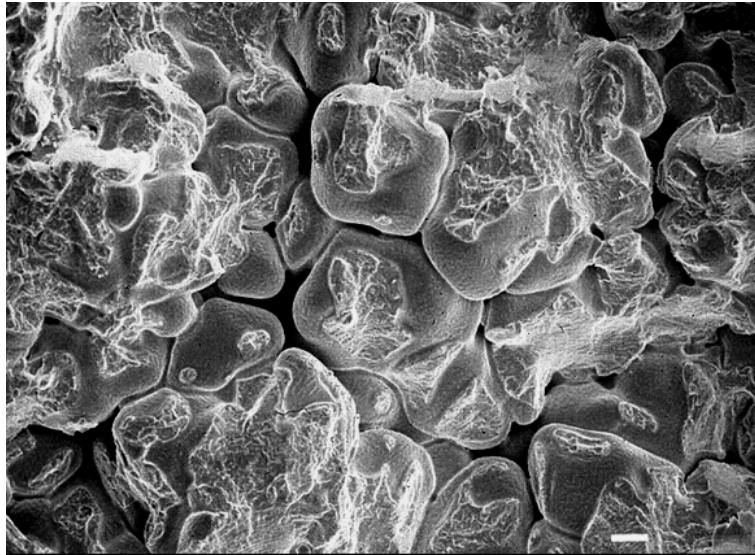
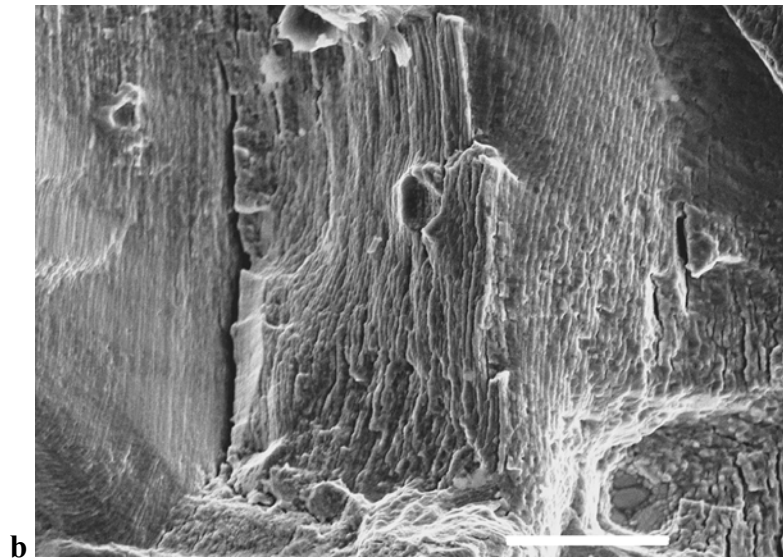
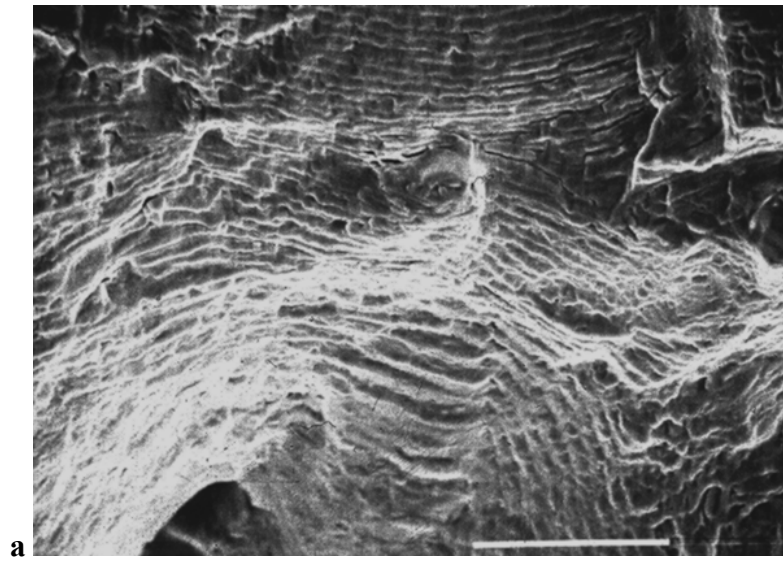


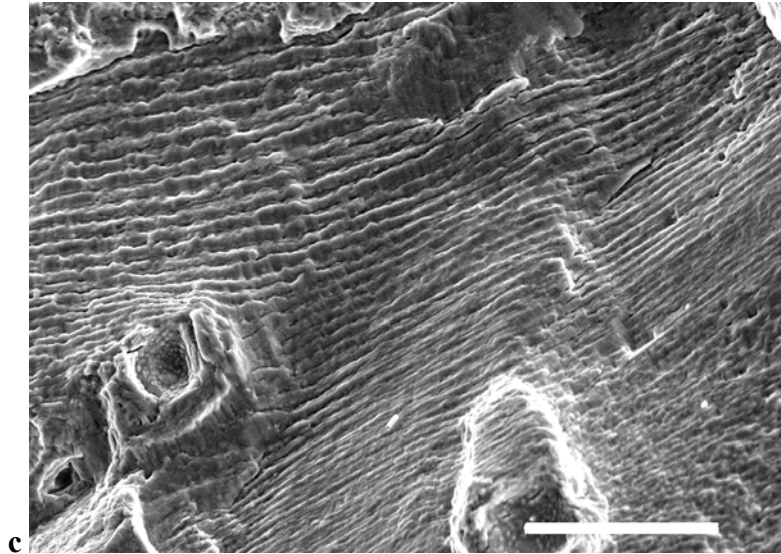
Figure 6.2. Secondary electron SEM image showing the incomplete solidification (dendritic structure) around the fatigue crack initiation region on the fracture surface of one Super Star alloy specimen, which failed after 1,516,640 cycles at  $0.15\sigma_{0.2}$  (scale bar length = 10  $\mu\text{m}$ ).



Continued

Figure 6.3. Secondary electron SEM images of fatigue fracture surfaces for (a) Super Star, 1,516,640 cycles at  $0.15\sigma_{0.2}$  (scale bar length = 20  $\mu\text{m}$ ), (b) Rx 91, 1,226,010 cycles at  $0.15\sigma_{0.2}$  (scale bar length = 10  $\mu\text{m}$ ), and (c) W-1, 907,330 cycles at  $0.20\sigma_{0.2}$  (scale bar length = 10  $\mu\text{m}$ ), showing typical fatigue striations in the alloys.

Figure 6.3 continued



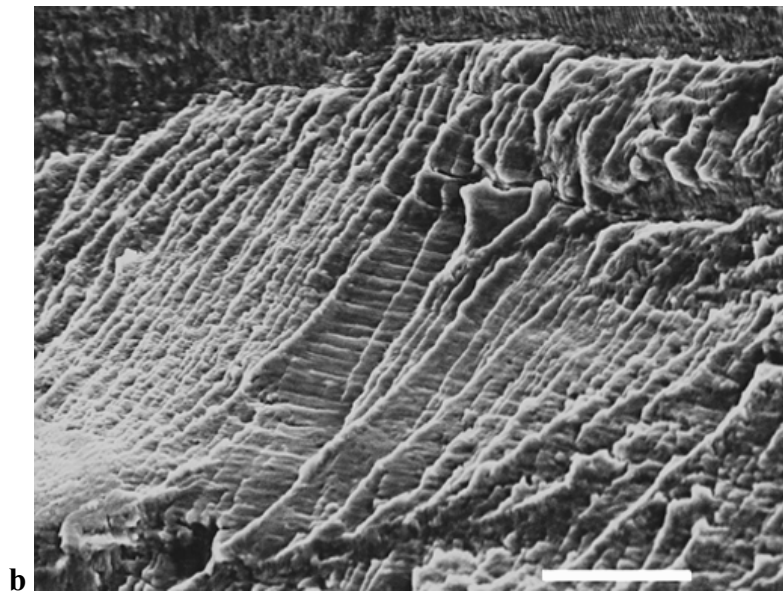
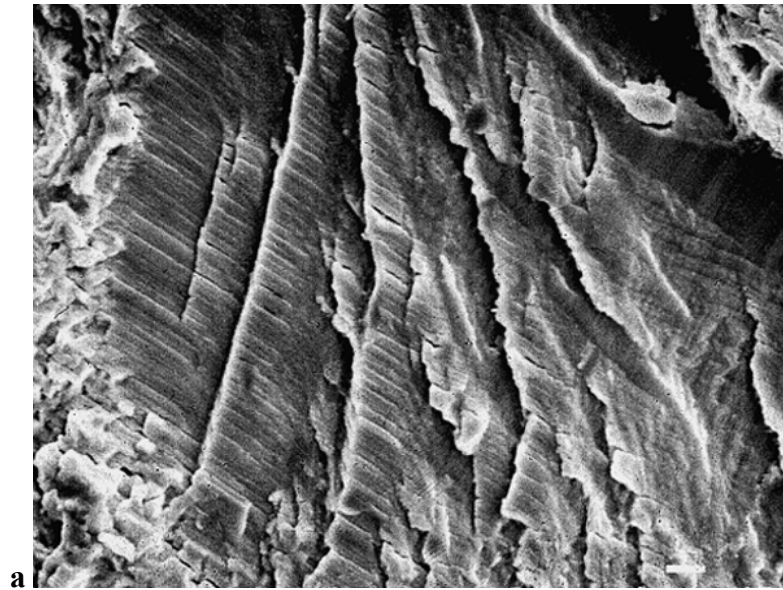


Figure 6.4. Secondary electron SEM images of the fatigue fracture surfaces for (a) Super Star, 715,875 cycles at  $0.20\sigma_{0.2}$  (scale bar length =  $1\ \mu\text{m}$ ) and (b) W-1, 659,555 cycles at  $0.15\sigma_{0.2}$  (scale bar length =  $5\ \mu\text{m}$ ), showing terraced patterns of striations.

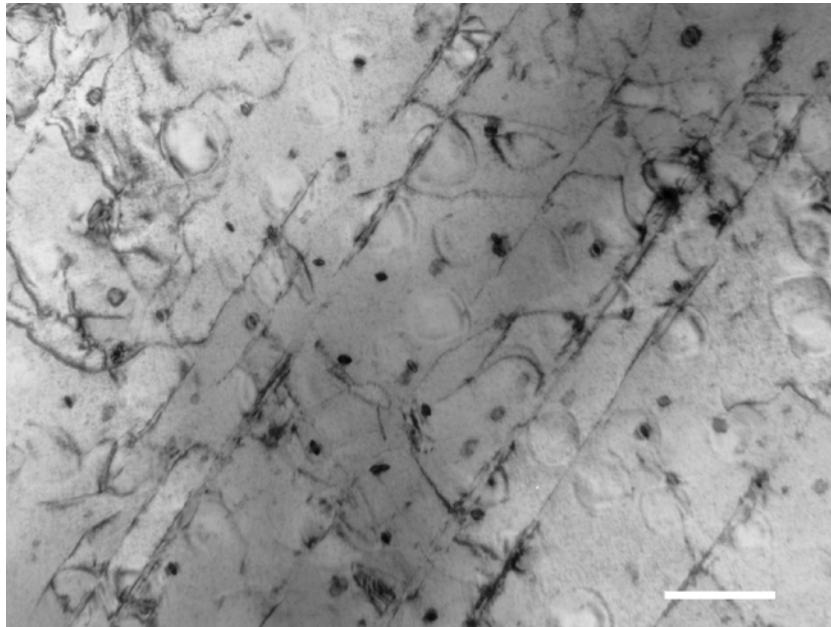


Figure 6.5. TEM bright-field image of tangled dislocations and stress-induced slip bands in fatigued W-1, 183,210 cycles at  $0.20\sigma_{0.2}$  (scale bar length = 200 nm).

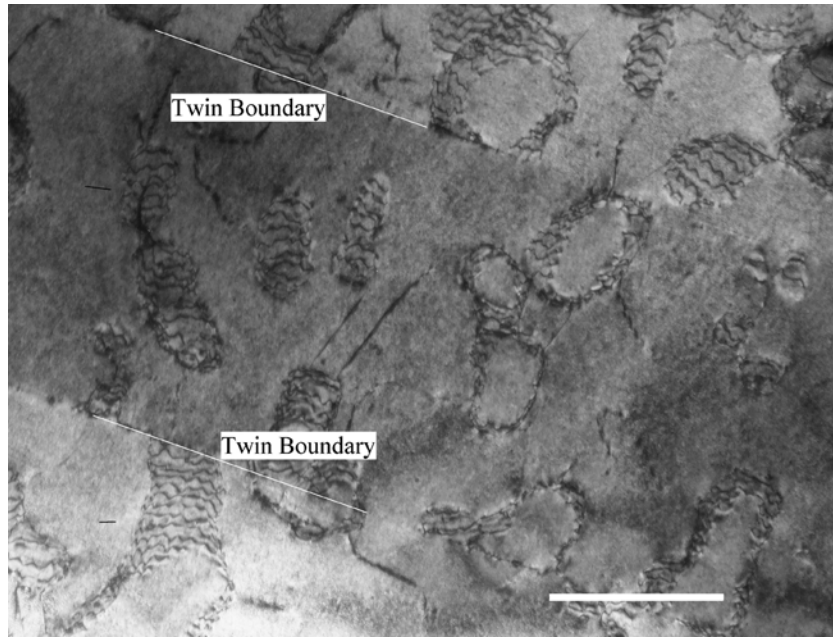


Figure 6.6. TEM bright-field image showing interphase boundary dislocations between the spherical precipitates and the surrounding twinned matrix of fatigued Rx 91, 983,905 cycles at  $0.15\sigma_{0.2}$  (scale bar length = 200 nm).

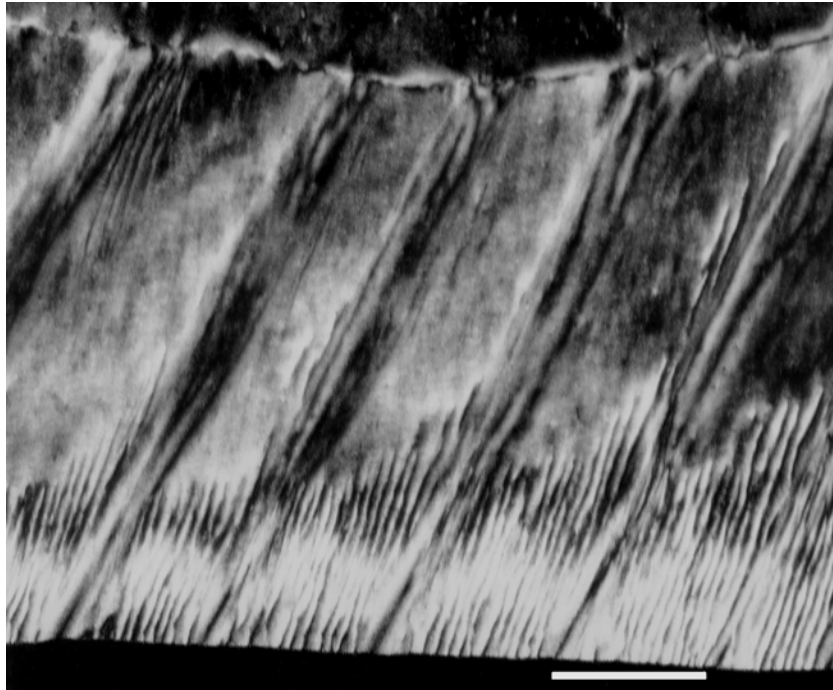


Figure 6.7. TEM dark-field image showing twinning inside discontinuous precipitates due to fatigue deformation in Rx 91, 983,905 cycles at  $0.15\sigma_{0.2}$  (scale bar length = 50 nm).

## CHAPTER 7

### MICROSTRUCTURES AND FATIGUE BEHAVIOR OF TWO COMMERCIAL PD–AG DENTAL CASTING ALLOYS IN THE PRESENCE OF CASTING POROSITY

#### 7.1 Introduction

Since their introduction in the early 1970s, Pd–Ag dental casting alloys have been widely used for metal-ceramic restorations and superstructures for implants (Bertolotti, 1984; Goodacre, 1989; Huget and Civjan, 1974). The properties of Pd–Ag alloys are comparable or superior to gold-based and high-Pd ceramic alloys. They have acceptable yield strength, excellent ductility, high elastic modulus, high sag resistance during porcelain firing, excellent porcelain-metal bonding strength, favorable handling properties and solderability, and satisfactory tarnish and corrosion resistance (Huget, 1976; Bertolotti, 1983; Compton *et al.*, 1985; Reel *et al.*, 1986; Mezger *et al.*, 1989c; Limkool and Sumii, 1995; Papazoglou and Brantley, 1998; Papazoglou *et al.*, 2001; Sun, 2004). The clinical selection of Pd–Ag alloys has increased because of the alleviation or elimination of former porcelain discoloration concerns by proper melting and casting techniques, selection of particular brands of porcelain, and the incorporation of certain

elements in the alloy compositions (Lacy *et al.*, 1977; Bertolotti, 1984; Ringle *et al.*, 1986; Bertolotti, 1988; Goodacre, 1989; O'Brien *et al.*, 1998; Brantley and Laub, 2001; Stavridakis *et al.*, 2004).

As almost all restorations are subjected to cyclic forces from mastication, it is necessary to understand the fatigue performance of dental casting alloys. At present, there is no standard for fatigue testing of dental alloys. Using tensile test specimens following ADA Specifications No. 5 (1997) and No. 38 (2000), which were subjected to clinically relevant heat treatment simulating the process for bonding porcelain, the fatigue limits and fracture characteristics of representative high-Pd (Li *et al.*, 2002) and Pd–Ag (Chapter 6) dental casting alloys were previously determined. The fatigue limits for both types of palladium-based alloys were relatively low, approximately 0.15 to 0.20 of the 0.2% yield strength in tension. However, these fatigue test specimens were much larger than clinical cast restorations, and it has been found that the microstructures of these specimens may differ from much smaller specimens having the dimensions of clinical restorations (Vermilyea *et al.*, 1996; Papazoglou *et al.*, 2000).

The question arises as to whether fatigue properties for these larger fatigue test specimens are appropriate for clinical restorations. The purposes of this study were to (a) compare the microstructures and Vickers hardness values of fatigue test specimens and specimens simulating copings for maxillary incisor restorations prepared from two Pd–Ag alloys that had not previously been investigated and (b) study the fatigue limits and fracture characteristics of these alloys.

## 7.2 Materials and Methods

Two Pd–Ag alloys, IS 64 and d.SIGN 59 (Ivoclar Vivadent, Amherst, NY), were selected. Nominal compositions and mechanical properties (after simulated heat treatment for porcelain application) of the alloys are listed in Tables 2.1 and 7.1, respectively. The IS 64 alloy has physical properties intended to match those for dental implant superstructures. The d.SIGN 59 alloy has mechanical and physical properties that are coordinated with the IPS d.SIGN fluorapatite-leucite glass-ceramic material (Ivoclar Vivadent).

A fine-grained, carbon-free, phosphate-bonded investment (Cera-Fina, Whip-Mix, Louisville, KY) was used to prepare two types of cast specimens. The first type simulated a coping for a maxillary central incisor restoration (Vermilyea, 1996), and wax patterns were used. The second type met the dimensional requirements of ADA Specification Nos. 5 (1997) and 38 (2000) for tensile test bars, with gauge diameter of 3 mm and gauge length of 15 mm, and polystyrene plastic patterns (Salco, Romeoville, IL) were used. The alloys were melted with a multi-orifice gas-oxygen torch, centrifugally cast using a broken-arm casting machine, and bench-cooled. After divesting, the sprues were cut from the specimens using a carborundum disk, and any visible nodules were removed. The specimens for fatigue testing otherwise had the as-cast surface condition, and were not subsequently air-abraded or polished.

Cast specimens that simulated copings were cross-sectioned into halves, using a slow-speed water-cooled diamond saw (Leco, St. Joseph, MI). One half was used to investigate the as-cast microstructure, and the other half was subjected to the entire heating regimen for application of dental porcelain (Ultra-Mat CDF, 3M Unitek,

Monrovia, CA). The initial oxidation treatment followed the instructions of the alloy manufacturer, and the subsequent firing cycles followed the recommendations for IPS Classic porcelain (Ivoclar Vivadent). All specimens for fatigue testing received the full heat-treatment regimen for porcelain application.

Fatigue tests were performed in air at room temperature, using uniaxial sinusoidal tension-compression loading with a servohydraulic mechanical testing machine (Model 1322, Instron Corp., Canton, MA). The ratio (R) between compressive and tensile stress amplitudes was  $-1$ , and the frequency was 10 Hz. Starting stress amplitudes were based on previous experience with high-Pd (Li *et al.*, 2000) and Pd–Ag (Chapter 6) alloys, which resulted in the need for considerably fewer specimens than with conventional staircase methods (ASTM, 1963; Collins, 1993). Two replicate specimens were tested at each stress amplitude, and the highest stress at which fracture did not occur after a clinically relevant number (Anselm, 1995) of  $2 \times 10^6$  cycles was designated as the fatigue limit. Fracture surfaces of fatigued specimens were examined with a scanning electron microscope (SEM) JSM-820 (JEOL Ltd, Tokyo, Japan) over a range of magnifications. Before SEM examination, these specimens were ultrasonically cleaned in ethanol.

Microstructural observations were carried out with the same SEM on the coping specimens in both the as-cast and heat-treated conditions, and on specimens from the fractured fatigue test bars (axial and longitudinal). Both types of metallographic specimens were first obtained by sectioning with the use of a slow-speed water-cooled diamond saw. Specimens were mounted in transparent epoxy resin (Leco, St. Joseph, MI). After grinding with 320, 400, and 600 grit silicon carbide papers, and polishing with a series of gamma-alumina slurries ending with  $0.05 \mu\text{m}$  particles, specimens were etched

in aqua regia solutions, using appropriate times to obtain optimum microstructures. Porosity evaluation was conducted on fatigue fracture surfaces and on samples sectioned both axially (about 3 mm from fracture surface) and longitudinally from fatigue test specimens, using the SEM and an optical microscope (Nikon Epiphot, Nippon Kogaku K.K., Japan). Preparation method of the samples is the same as that of specimens for microstructural observation, except that these samples were not etched. Image analysis was completed using ImageJ software (ImageJ 1.34, National Institute of Health, Bethesda, MD). An equivalent pore diameter  $D_e$  (Yi *et al.*, 2003; Gao *et al.*, 2004) was used to describe the size of near spherical or irregular shape pores, which is defined here as  $D_e = 2[A_p/\pi]^{1/2}$  with  $A_p$  the pore area measured directly from metallographic samples or fatigue fracture surfaces.

Vickers hardness (M-400, Leco Corp, St. Joseph, MI) was measured on etched specimens, using a 1 kg load and dwell time of 30 seconds. Mean hardness values were obtained from 5 indentations. Analysis of variance (ANOVA) at the  $\alpha = 0.05$  level was used to determine if significant differences in hardness existed between (a) as-cast and heat-treated specimens of the same alloy, (b) the two alloys in the as-cast or heat-treated condition, and (c) coping specimens and fatigue test specimens of the same alloy in the heat-treated condition.

## **7.3 Results**

### **7.3.1 Microstructures**

Microstructures of as-cast and heat-treated IS 64 and d.SIGN 59 coping specimens are shown in Figure 7.1a and b, and Figure 7.1c and d, respectively. The as-cast microstructures of both alloys were inhomogeneous. After simulated porcelain firing heat treatment, the microstructures of the coping specimens were homogenized and contained numerous precipitates. Microstructures of heat-treated fatigue test specimens are shown in Figure 7.2a and b. Compared to the heat-treated coping specimens for IS 64 and d.SIGN 59, the much larger fatigue test specimens had incompletely homogenized microstructures.

### **7.3.2 Vickers Hardness**

Table 7.2 summarizes the Vickers hardness measurements for the as-cast and heat-treated coping specimens and the heat-treated fatigue test specimens for the IS 64 and d.SIGN 59 alloys. The results of statistical comparisons using ANOVA are presented in Tables 7.3 and 7.4. There was no significant difference in Vickers hardness of the coping specimens for the two alloys in either the as-cast condition or the simulated porcelain-firing heat-treated condition. However, after heat treatment, the Vickers hardness of the coping specimens fabricated from each alloy decreased significantly, compared to the as-cast condition. The Vickers hardness of the heat-treated fatigue test specimens was significantly higher than that of the heat-treated coping specimens which had much smaller dimensions. The Vickers hardness for the heat-treated fatigue test specimens fabricated from both alloys were quite close to the value (230) provided by the manufacturer for the porcelain-fired heat-treated condition (Table 7.1).

### **7.3.3 Fatigue Limits**

Table 7.5 lists the number of cycles to failure at different stress amplitudes for IS 64 and d.SIGN 59. Because the fatigue limit of cast Pd-based dental alloys is sharply dependent upon stress amplitude (Li *et al.*, 2002; Chapter 6), the fatigue limit of IS 64 is close to 0.20 of its 0.2% yield strength, while the fatigue limit of d.SIGN 59 is close to 0.25 of its 0.2% yield strength.

### **7.3.4 Casting Porosity and Fracture Characteristics**

Numerous unevenly distributed casting pores were observed in all fatigue test specimens, with a tendency to segregate to one half along the fracture surface and cross-section of the specimens, as shown in Figure 7.3. IS 64 specimens exhibited less porosity than d.SIGN 59 specimens. The porosity in one d.SIGN 59 fatigue test specimen (Specimen 8 in Table 7.5) was serious with an overall pore area percentage of 12% and maximum equivalent pore diameter of 280  $\mu\text{m}$ . In this specimen, near-surface porosity was considered to be the cause of fracture at a low number of 405,874 cycles with 0.25  $\sigma_{0.2}$ . Among all other specimens, the overall pore area percentage was not more than 5% in IS 64 and 10% in d.SIGN 59. The maximum equivalent pore diameter in IS 64 and d.SIGN 59 specimens was observed to be 85  $\mu\text{m}$  (Specimen 4 in Table 7.5, fractured at 1,651,575 cycles) and 150  $\mu\text{m}$  (Specimen 7 in Table 7.5, survived 2 million cycles), respectively. Figure 7.4 shows casting pore distribution on the cross-sectioned and polished surface of this d.SIGN 59 fatigue specimen. Such relatively large and widely separated casting pores could be tolerated in these relatively large test specimens without serious degradation of the fatigue properties.

On the complex fatigue fracture surfaces, fatigue crack initiation sites were not uniformly determined, either near the specimen surface or inside the specimen, or with multiple locations. Fatigue striations were observed on the fracture surfaces of IS 64 and d.SIGN 59. The local orientation of the striations changed in IS 64, as shown in Figure 7.5a, but this change was not observed in the fracture surface of d.SIGN 59, as shown in Figure 7.5b.

## **7.4 Discussion**

### **7.4.1 Specimen Size and Microstructures**

The speed of liquid metal solidification is very high during conventional dental casting, and the microstructures of as-cast high-Pd alloys can deviate substantially from their equilibrium microstructures (Brantley *et al.*, 1993). During the porcelain firing process, the as-cast microstructures of the Pd–Ag alloy generally become homogenized, as shown in Figure 7.1. For the relatively large tensile test specimens (identical to those used in the fatigue tests) of one high-Pd alloy, Spartan Plus (Ivoclar Vivadent, Amherst, NY), the as-cast dendritic microstructure was not completely eliminated by porcelain-firing heat treatment (Papazoglou *et al.*, 2000). Moreover, the near-surface eutectic constituent Brantley *et al.*, 1993) in as-cast coping specimens of the high-Pd alloy Liberty (Heraeus Kulzer, Armonk, NY) was not observed in the much larger as-cast tensile test specimens (Papazoglou *et al.*, 2000). These examples illustrate the great importance of casting thickness, which controls the rate of heat flow from the solidifying alloy, on as-cast microstructure of the high-Pd alloys.

Similar observations were made for the Pd–Ag alloys in this study, in which the microstructures of the relatively large fatigue test specimens for both alloys were not homogenized after the porcelain firing heat treatment, as shown in Figure 7.2. Therefore, the effect of the test specimen dimensions for the Pd–Ag alloy on the resulting as-cast and heat-treated microstructures cannot be ignored. Consequently, the data for mechanical properties obtained with relatively large test specimens with dimensions meeting ADA specification requirements (1997; 2000) may not accurately reflect the mechanical properties of clinical restorations.

#### **7.4.2 Comparison of Fatigue Properties for IS 64 and d.SIGN 59**

The compositions of IS 64 and d.SIGN 59 are very similar, with only small differences in the percentages of component elements (Table 2.1). However, the microstructures of the two alloys are quite different (Figures 7.1 and 7.2) and the 0.2% yield strength of IS 64 is over 10% higher than that of d.SIGN 59 (Table 7.1). However, the stress value for fatigue limit of d.SIGN 59 appears to be 10% greater than that of IS 64 (Table 7.5), which is inconsistent with previous observations that the high-Pd or Pd–Ag alloy with higher yield strength exhibits higher fatigue limit (Li *et al.*, 2002; Chapter 6). The difference in fatigue performance for IS 64 and d.SIGN 59 can be attributed to microstructural differences and the mechanisms for fatigue fracture. For example, the variation of fatigue striation orientation in IS 64, shown in Figure 7.5a, suggests relative ease of fatigue crack initiation at multiple sites and/or relative ease of fatigue crack propagation in this alloy. Determination of the detailed mechanisms for fatigue crack initiation and propagation in these Pd–Ag alloys requires further study.

### ***7.4.3 Effects of Specimen Size and Casting Porosity on Fatigue Performance***

Experience in engineering has shown that in most cases a specimen size effect on fatigue performance exists, and two factors can result from change in fatigue specimen size: (a) the change in surface area, and (b) the variation of stress gradient across the specimen diameter and the volume of material that is highly stressed (Dieter, 1986; Dowling, 1993). Since specimen size effects on microstructures can occur for Pd-based dental alloy castings, it is important to have a standardized protocol for fatigue testing that provides performance information relevant to fatigue conditions for clinical restorations. Such a standardized tensile test or fatigue test for specimens having the dimensions of typical metal-ceramic restorations remains to be developed.

During practical dental casting processes, casting defects such as pores and microshrinkage, cannot be completely eliminated (Anusavice, 1996; Mizumoto *et al.*, 2003). Casting porosity in steels, engineering aluminum and magnesium alloys has been reported to be preferential fatigue crack initiation sites and constitute the main influence on fatigue properties (Stanzl-Tschegg *et al.*, 1995; Mayer *et al.*, 1999; Buffiere *et al.*, 2001; Wang *et al.*, 2001; Horstemeyer *et al.*, 2002; Mayer *et al.*, 2003; Yi *et al.*, 2003; Gao *et al.*, 2004; Sigl *et al.*, 2004; Mayer *et al.*, 2005). A cast Ag–Pd–Cu–Au–Zn alloy for dental applications has been found to have considerably smaller fatigue strength than the drawn Ag–Pd–Cu–Au–Zn alloy (Mizumoto *et al.*, 2002; Mizumoto *et al.*, 2003). Although quantitative approaches (Wang *et al.*, 2001; Yi *et al.*, 2003; Mizumoto *et al.*, 2002; Mayer *et al.*, 2003; Mizumoto *et al.*, 2003; Sigl *et al.*, 2004; Gao *et al.*, 2004; Mayer *et al.*, 2005) have been made to predict the relation between fatigue life and casting porosity, there is no well accepted method to predict the effects of porosity on fatigue life.

Important measures of casting porosity include morphology, size, density and fraction of pores. Under cyclic stresses, high stress concentration around sharp porosity can be released by localized plastic deformation and thus the shape effect of pores on fatigue performance can be negligible (Gao *et al.*, 2004). The present results indicate that specimens with many pores in both IS 64 and d.SIGN 59 survived 2 millions cycles, while only one d.SIGN 59 specimen with severe casting porosity fractured after an expectedly low number cycles (specimen 8 in Table 7.5, with total pore area percentage of 12% and a maximum equivalent pore diameter of 280  $\mu\text{m}$ ). This suggests that in the present Pd–Ag alloys there exists a critical pore size, below which the alloys exhibit fatigue tolerance to the pores. Similar pores size affects on fatigue have been reported in cast aluminum and magnesium alloys (Mayer *et al.*, 1999; Buffiere *et al.*, 2001; Wang *et al.*, 2001; Horstemeyer *et al.*, 2002; Mayer *et al.*, 2003; Gao *et al.*, 2004; Mayer *et al.*, 2005) and in Ag–Pd alloys (Mizumoto *et al.*, 2002, 2003). The critical pore size is approximately on the order of 150  $\mu\text{m}$  for d.SIGN 59 and 85  $\mu\text{m}$  for IS 64. The corresponding critical stress intensity amplitude  $K_{\text{cr}}$  can be roughly calculated using equation (Mayer *et al.*, 2003):

$$K_{\text{cr}} = \sigma_{\text{cr}} \alpha [\pi A_p^{1/2}]^{1/2} \quad (1)$$

where  $\sigma_{\text{cr}}$  is the critical stress amplitude and here can be correlated to fatigue limit (Mayer *et al.*, 2003);  $A_p$  is the area of the pore with maximum equivalent pore diameter, which was measured on the metallographic or fatigue fracture surface;  $\alpha=0.65$  for surface cracks and  $\alpha=0.50$  if the cracks originate from internal porosity. As both experimental observation and finite element analysis indicated that large pores close to or at the specimen surface induce higher stress/strain concentration than other pores (Yi *et al.*,

2003; Gao *et al.*, 2004), pores at or near surface were considered to simplify calculation. The critical stress intensity amplitude was then calculated to be approximately 1.12 MPam<sup>1/2</sup> and 1.63 MPam<sup>1/2</sup> for IS 64 and d.SIGN 59, respectively, which are quite close to the critical stress intensity amplitude values (Mayer *et al.*, 2003) in casting magnesium alloys. When the size of casting pores is less than the critical pore size, the critical stress intensity amplitude is below long crack threshold stress intensity. In such case, even though fatigue cracks may initiate at porosity, they will not propagate to cause fatigue failure. Therefore, these pores are in non-propagating conditions (Mayer *et al.*, 2005) and thus tolerable for fatigue performance. It should be noted that the effective cross-section reduction due to existence of one pore with critical pore size and the resulting rise in overall mean stress inside the specimen is considerably small. However, if many pores with comparable size aggregate in the same cross-section, the rise in overall mean stress in specimen will be significant. Characterization of the locations and distribution of casting pores and an investigation of the effects of casting porosity on fatigue properties of Pd–Ag alloys are strongly recommended for future research. The casting porosity in these alloys, along with their complex microstructures, should be directly related to their relatively low ratios of fatigue limit to yield strength.

## **7.5 Conclusions**

Under the conditions of present study, the following conclusions can be drawn:

1. While the microstructures of as-cast IS 64 and d.SIGN 59 coping specimens were inhomogeneous, after simulated porcelain-firing heat treatment the microstructures were substantially homogenized with the formation of numerous precipitates.

2. In comparison with the heat-treated coping specimens, the relatively larger heat-treated fatigue test specimens of the two alloys had incompletely homogenized microstructures.
3. There was no significant difference in Vickers hardness between the IS 64 and d.SIGN 59 coping specimens for the as-cast condition and for the heat-treated condition. After the simulated porcelain-firing heat treatment, significant decreases occurred in the Vickers hardness of the coping specimens prepared from the two alloys. The Vickers hardness of the heat-treated fatigue test specimens was significantly higher than that of the heat-treated coping specimens.
4. The fatigue limit of IS 64 is close to 0.20 of its 0.2% yield strength, while the fatigue limit of d.SIGN 59 is close to 0.25 of its 0.2% yield strength. The relative values of fatigue limit for these two alloys are reversed from the relative values of yield strength, suggesting differences in fatigue crack initiation and propagation at the microstructural level.
5. The general insensitivity of fatigue limit to casting porosity for most IS 64 and d.SIGN 59 specimens suggests that there is a critical pore size, above which fatigue resistance reduces significantly. The low ratio of fatigue limit to yield strength for these Pd–Ag alloys is attributed to their complex microstructures and casting defects.

Alloy	0.2% Yield Strength (MPa)	Vickers hardness	Elongation (%)
IS 64	560	230	31.0
d.SIGN 59	490	230	14.0

Ivoclar Vivadent, Amherst, NY.

Table 7.1. Mechanical properties reported by manufacturer (simulated heat treatment for porcelain application).

Alloy	As-cast copings	Heat-treated copings	Fatigue test specimens (Heat-treated)
IS 64	237 (8.8)	201 (7.3)	224 (10.3)
d.SIGN 59	244 (7.3)	206 (9.9)	229 (3.6)

Data are mean values (standard deviations). Heat treatment simulated application of dental porcelain.

Table 7.2. Vickers hardness (VHN) for copings and fatigue test specimens.

Source	df	Sum of Squares	Mean Square	F-value	P-value
Alloy	1	409.657	409.657	43.730	0.096
Condition	1	13752.528	13752.528	1468.065	0.017
Alloy × Condition	1	9.368	9.368	0.132	0.718
Error	36	2546.482	70.736		

Table 7.3. Statistical comparisons between as-cast and heat treated coping specimens by using two-way ANOVA.

Source	d.f.	Sum of Squares	Mean Square	F-value	P-value
Alloy	1	266.779	372.798	2.798	0.033
Specimen Type	1	5307.695	7417.015	7417.015	0.007
Alloy × Specimen Type	1	0.716	0.716	0.011	0.919
Error	36	2439.738	67.770		

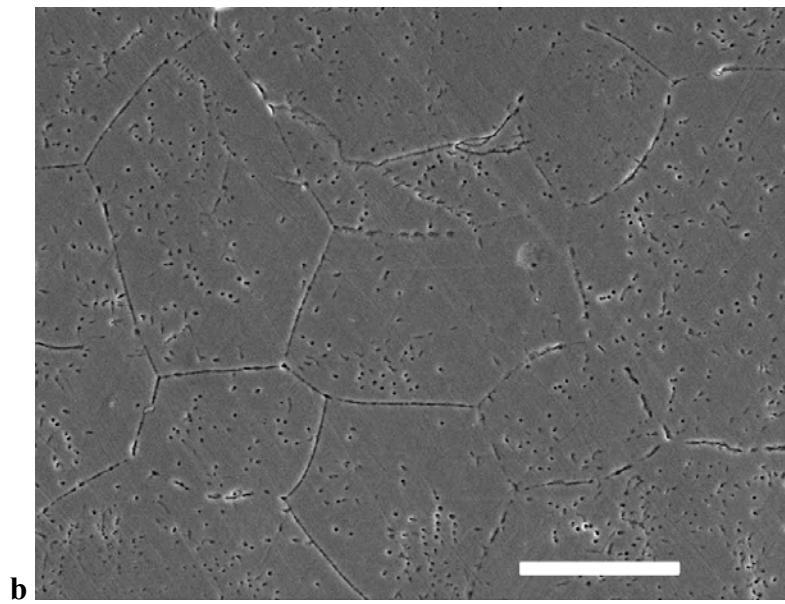
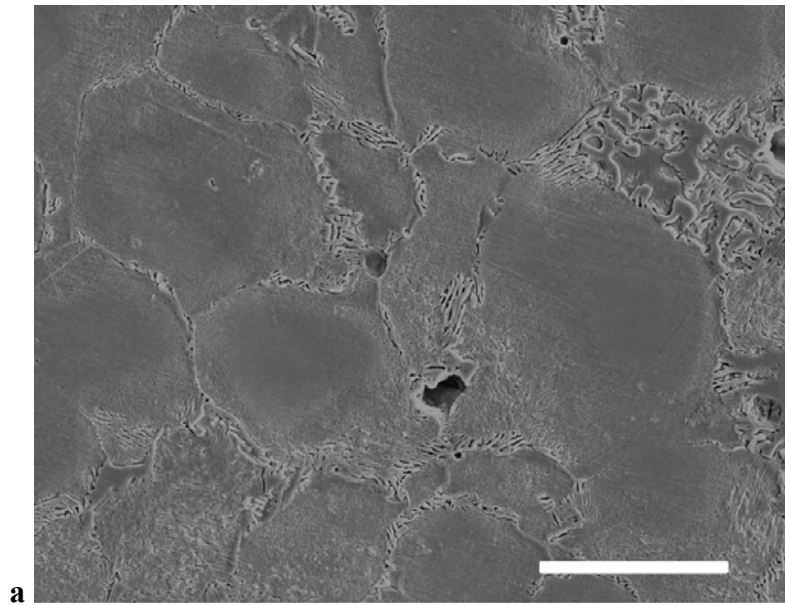
Table 7.4. Statistical comparisons between heat-treated coping specimens and fatigue test specimens by using two-way ANOVA.

Specimen No.	Alloy	Stress Amplitude	Cycles to Failure
1	IS 64	0.15 $\sigma_{0.2}$ (84 MPa)	> 2,000,000
2		0.15 $\sigma_{0.2}$ (84 MPa)	—*
3		0.20 $\sigma_{0.2}$ (112 MPa)	1,350,751
4		0.20 $\sigma_{0.2}$ (112 MPa)	1,651,575
5	d.SIGN 59	0.20 $\sigma_{0.2}$ (98 MPa)	> 2,000,000
6		0.20 $\sigma_{0.2}$ (98 MPa)	> 2,000,000
7		0.25 $\sigma_{0.2}$ (123 MPa)	> 2,000,000
8		0.25 $\sigma_{0.2}$ (123 MPa)	405,874 **

\* Specimen 2 was inadvertently damaged during the initial set-up before the cyclic fatigue testing began.

\*\* The anomalously low number of cycles to failure for Specimen 8, compared to Specimen 7, was attributed to excessive surface porosity.

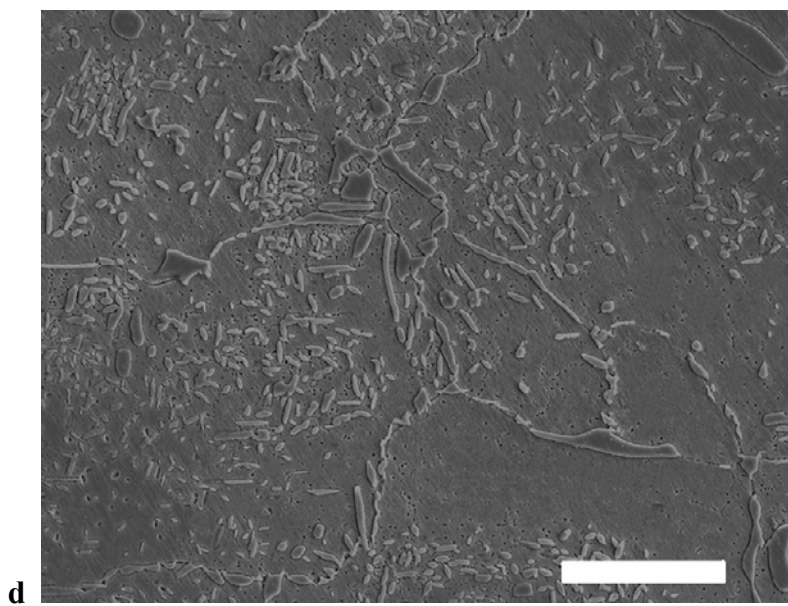
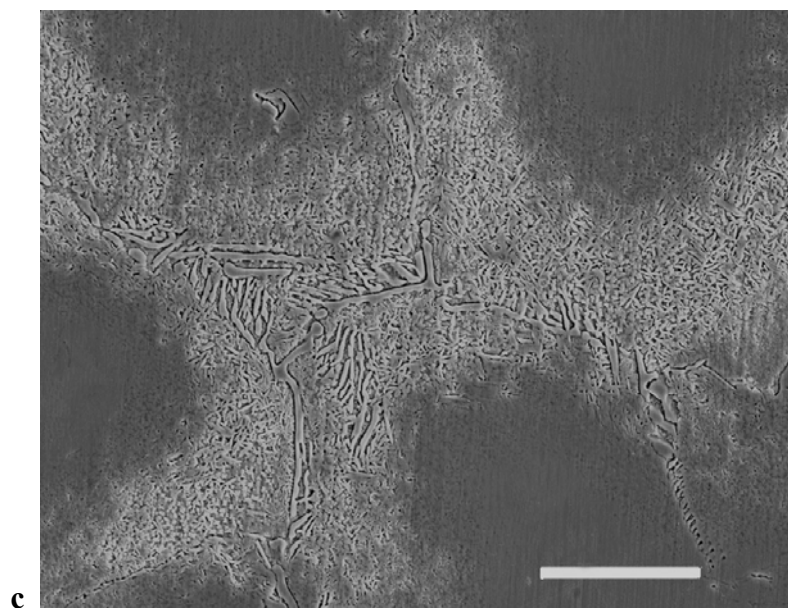
Table 7.5. Number of cycles to failure for IS 64 and d.SIGN 59 specimens tested at different stress amplitudes.



Continued

Figure 7.1. SEM images showing the microstructures of (a) as-cast and (b) heat-treated IS 64 coping specimens, and (c) as-cast and (d) heat-treated d.SIGN 59 coping specimens. Length of scale bar = 15  $\mu\text{m}$  for (a), and 10  $\mu\text{m}$  for (b), (c) and (d).

Figure 7.1 continued



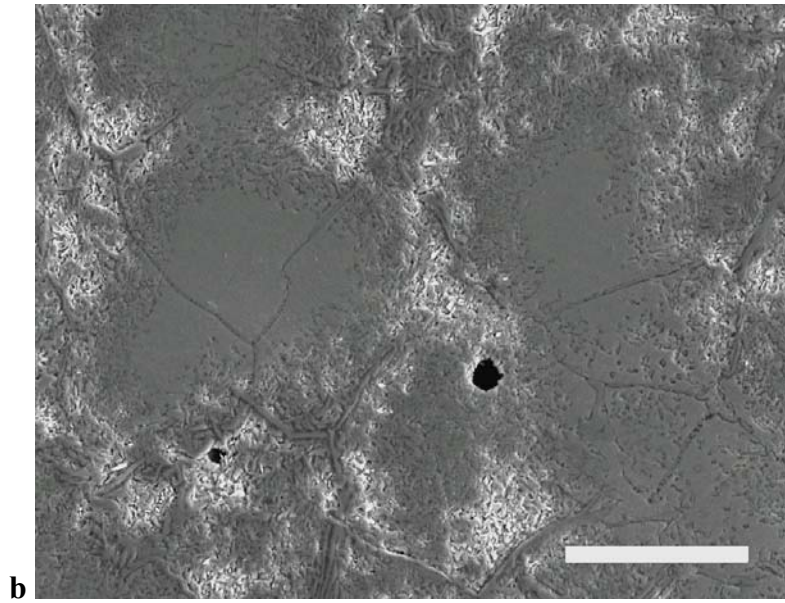
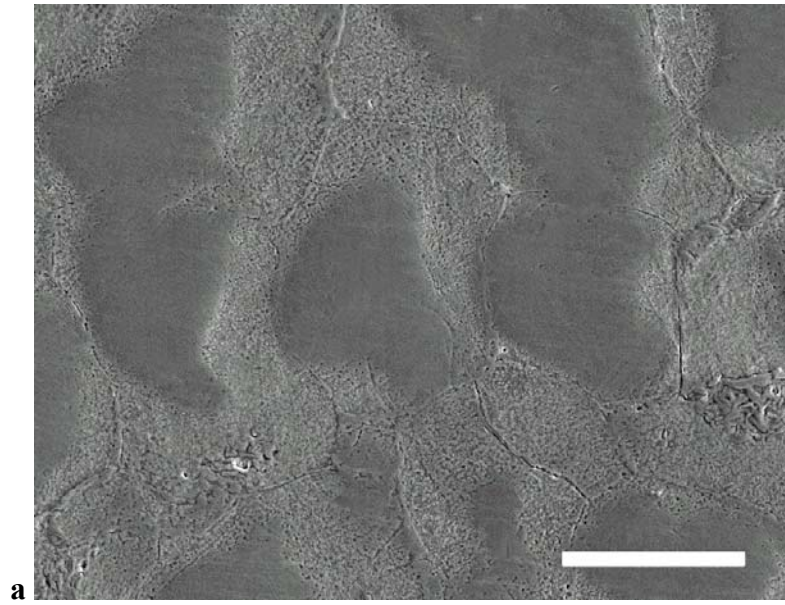


Figure 7.2. SEM images showing the incompletely homogenized microstructures in fatigue test specimens after simulated porcelain-firing heat treatment for (a) IS 64 and (b) d.SIGN 59. Length of scale bar = 30  $\mu\text{m}$  for (a) and 10  $\mu\text{m}$  for (b).

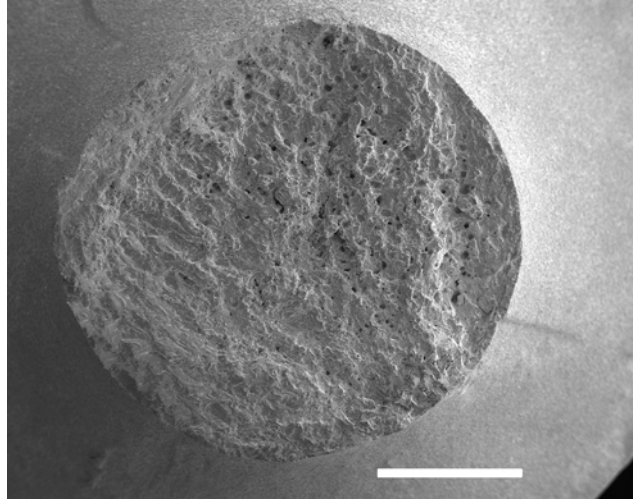
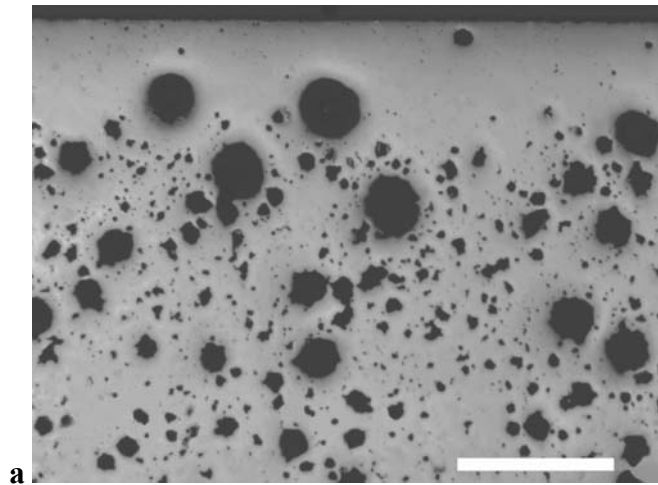


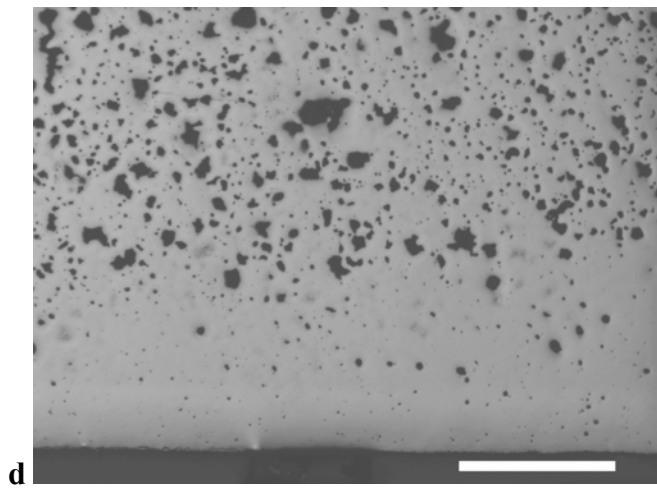
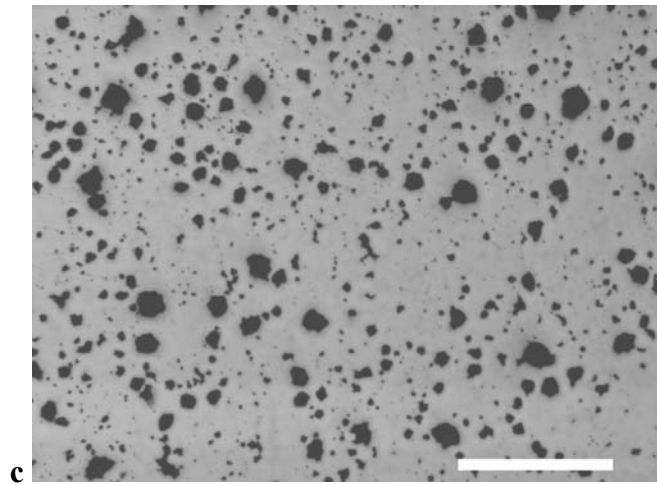
Figure 7.3. SEM image showing casting porosity in IS 64 specimen broken at 1,651,575 cycles (length of scale bar = 1 mm).



Continued

Figure 7.4. Optical micrographs showing casting porosity in longitudinally cross-sectioned d.SIGN 59 specimen survived 2 million cycles. (a) and (c) were taken in regions near two opposite surfaces; (b) was taken in central region. Length of scale bar = 400  $\mu\text{m}$ .

Figure 7.4 continued



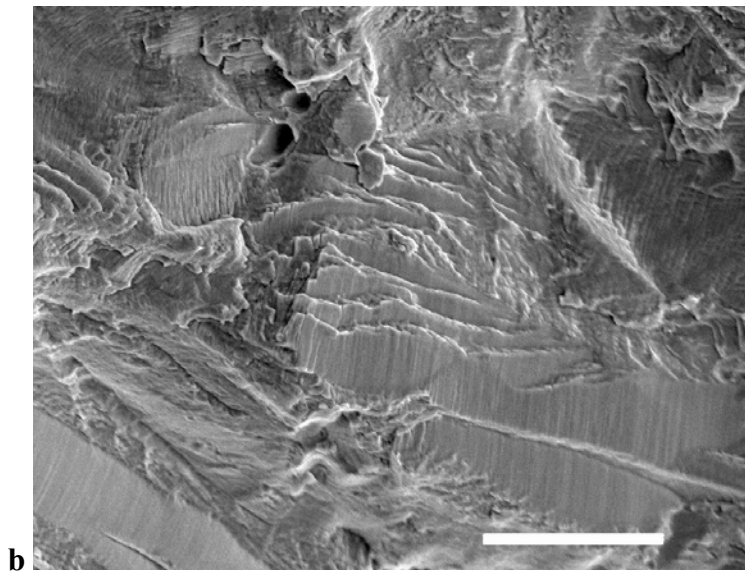
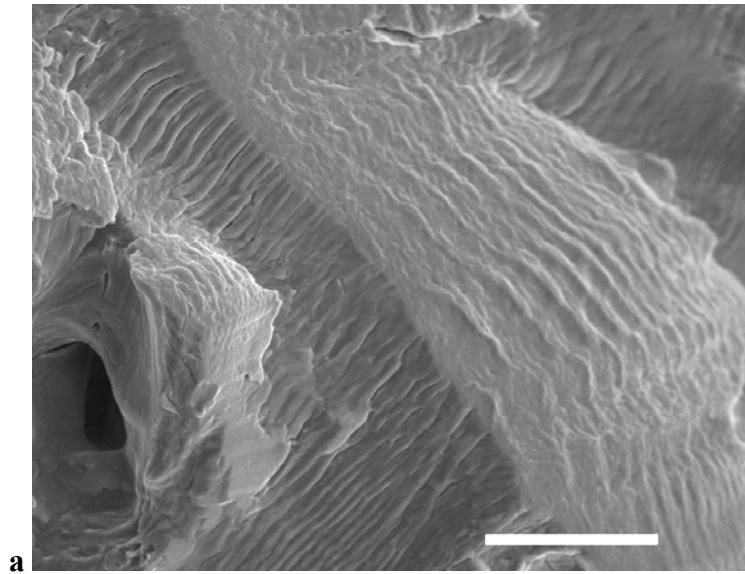


Figure 7.5. SEM images showing fatigue striations on the fracture surfaces of (a) IS 64 specimen broken at 1,651,575 cycles and (b) d.SIGN 59 specimen broken at 405,874 cycles. Length of scale bar = 10  $\mu\text{m}$  for (a) and 15  $\mu\text{m}$  for (b).

## BIBLIOGRAPHY

American Dental Association Report (1984). Classification system for cast alloys. *J Am Dent Assoc* 109:838.

American National Standards Institute/American Dental Association Specification No. 5 for dental casting alloys (American Dental Association, Council on Scientific Affairs, Chicago, IL, USA, 1997).

American National Standards Institute/American Dental Association Specification No. 38 for metal-ceramic dental restorative systems (American Dental Association, Council on Scientific Affairs, Chicago, IL, USA, 2000).

Anselm Wiskott HW, Nicholls JI, Belser UC (1995). Stress fatigue: basic principles and prosthodontic implications. *Int J Prosthodontics* 8:105-116.

Anusavice KJ, Shen C, Hashinger D, Twigg SW (1985). Interactive effect of stress and temperature on creep of PFM alloys. *J Dent Res* 64:1094-1099.

Anusavice KJ (1996). Phillips' Science of Dental Materials (10th ed). Saunders, Philadelphia, PA. p 423-430,

Asgar K (1988). Casting metal in dentistry: past-present-future. *Adv Dent Res* 2:33-43.

Ashton RF, Wesley RP, Dixon CR (1975). The effect of porosity on 5086-H116 aluminum alloy welds. *Welding J* 54:95s-98s.

ASTM special technical publication No. 91-A (2<sup>nd</sup> edn) (1963). A Guide for fatigue testing and the statistical analysis of fatigue data. American Society for Testing and Materials (ASTM). Philadelphia, PA. p 12-13.

Bertolotti RL (1983). Alternative casting alloy for today's crown and bridge restorations. Part II: metal-ceramic restorations. *J Calif Dent Assoc* 11:63-69.

Bertolotti RL (1984). Selection of alloys for today's crown and fixed partial denture restorations. *J Am Dent Assoc* 108:959-966.

- Bertolotti RL (1988). Rational selection of casting alloys. In: Perspectives in dental ceramics; Proceedings of the Fourth International Symposium on Ceramics (edited by Preston JD). Chicago: Quintessence. p 79.
- Bertolotti RL (2002). Alloys for porcelain-fused-to-metal restorations. In: Dental Materials and Their Selection (Edited by O'Brien WJ), 3rd edn (Quintessence, Chicago, 2002), p 204-204.
- Berzins D, Sarkar NK, Kawashima I. (1999). Electrochemical behavior of oxidized high Pd ceramic alloys [Abstract]. J Dent Res 78:112.
- Berzins D, Sarkar NK, Kawashima I. (2000a). Effect of oxidation on the corrosion of commercial high-Pd alloys [Abstract]. J Dent Res 79:596.
- Berzins DW, Kawashima I, Graves R, Sarkar NK (2000b). Electrochemical characteristics of high-Pd alloys in relation to Pd-allergy. Dent Mater 16:266-273.
- Bessing C, Kallus T (1987). Evaluation of tissue response to dental alloys by subcutaneous implantation. Acta Odontol Scand 45:247-255.
- Blanco-Dalmau L (1983). Preventing green discoloration of porcelain baked over silver-palladium alloys. J Prosthet Dent 50: 865.
- Böning K, Walter M (1990). Palladium alloys in prosthodontics: selected aspects. Int Dent J 40:289-297.
- Boyajian BK (1981). Palladium-based dental alloy containing indium and tin. U.S. Patent No. 4,261,744.
- Braemer W (2001). Biocompatibility of dental alloys. Adv Eng Mater 10: 753-761.
- Brantley WA, Cai Z, Carr AB, Mitchell JC. Metallurgical structures of as-cast and heat-treated high-palladium dental alloys. Cells Mater 1993;3:103-114.
- Brantley WA, Cai Z, Foreman DW, Mitchell JC, Papazoglou E, Carr AB (1995). X-ray diffraction studies of as-cast high-palladium alloys. Dent Mater 11:154-160.
- Brantley WA, Cai Z, Papazoglou E, Mitchell JC, Kerber SJ, Mann GP, Barr TL (1996). X-ray diffraction studies of oxidized high-palladium alloys. Dent Mater 12:333-341.
- Brantley WA, Wu Q, Cai Z, Vermilyea SG, Mitchell JC, Comerford MC (1999). Effects of casting conditions and annealing on microstructures and Vickers hardness of dendritic Pd-Cu-Ga dental alloys. Cells Mater 9: 83-92.

- Brantley WA, Laub LW (2001). Metal Selection. Framework design and metal selection for metal-ceramic restorations. In: Contemporary Fixed Prosthodontics (3rd edition. Edited by Rosenstiel SF, Land MF, Fujimoto J) St. Louis: Mosby. p 497-509.
- Buffiere JY, Savelli S, Jouneau PH, Maire E, Fougères R (2001). Experimental study of porosity and its relation to fatigue mechanisms of model Al–Si7–Mg0.3 cast Al alloys. *Mater Sci Eng A* 316:115-126.
- Cai Z, Chu X, Bradway SD, Papazoglou E, Brantley, WA (1995). On the biocompatibility of high-palladium dental alloys. *Cells Mater* 5:357-368.
- Cai Z, Brantley WA, Clark WA, Colijn HO (1997). Transmission electron microscopic investigation of high-palladium dental casting alloys. *Dent Mater* 13:365-371.
- Cai Z, Vermilyea SG, Brantley WA (1999). In vitro corrosion resistance of high-palladium dental casting alloys. *Dent Mater* 15:202-210.
- Canay S, Oktemer M (1992). In vitro corrosion behavior of 13 prosthodontic alloys. *Quint Int* 23:279-287.
- Carr AB, Brantley WA (1991). New high-palladium casting alloys: Part 1. Overview and initial studies. *Int J Prosthodont* 4:265-275.
- Carr AB, Cai Z, Brantley WA, Mitchell JC (1993). New high-palladium casting alloys: Part 2. Effects of heat treatment and burnout temperature. *Int J Prosthodont* 6:233-241.
- Cascone PJ (1984). Phase relations of the palladium-base, copper, gallium, indium system [Abstract]. *J Dent Res* 63:233.
- Chang E, Tseng B, Chou JC, Yin V (1989). Processing, Structure and Mechanical Property of Investment Cast IN-713LC Superalloy. *Trans Amer Foundry Soc* 96:47-54.
- Collins JA (1993). Fatigue of materials in mechanical design: analysis, prediction, and prevention (2nd Edition). New York: John Wiley & Sons. p 383-392.
- Compton HK, Lacefield WR, O'Neal SJ (1985). Marginal fit evaluation of palladium alloys vs a gold alloys [Abstract]. *J Dent Res* 64:317.
- Craig RG, Hanks CT (1990). Cytotoxicity of experimental casting alloys evaluated by cell culture tests. *J Dent Res* 69:1539-1542.
- Dieter GE (1986). Mechanical Metallurgy. New York: McGraw-Hill. p 375-380, 406-407.

- Dowling NE (1993). *Mechanical Behavior of Materials: Engineering Methods for Deformation, Fracture and Fatigue*. Prentice Hall, Englewood Cliffs, NJ. p 346-347, 396-398, 420-421.
- Gao YX, Yi JZ, Lee PD, Lindley TC (2004). The effect of porosity on the fatigue life of cast aluminum-silicon alloys. *Fatigue Fracture Eng Mater Structures* 27:559-570.
- Geurtsen W (2002). Biocompatibility of dental casting alloys. *Crit Rev Biol Med* 13: 71-84.
- Goehlich V, Marek M (1990). Corrosion behavior of Pd-Cu and Pd-Co alloys in synthetic saliva. *Dent Mater* 6:103-110.
- Goodacre CJ (1989). Palladium-silver alloys: A review of the literature. *J Prosth. Dent* 62: 34-37.
- Guo WH, Brantley WA, Li D, Monaghan P, Clark WA (2002). Fatigue studies of high-palladium dental casting alloys: Part II. Transmission electron microscopic observations. *J Mater Sci Mater Med* 13: 369-374.
- Guo WH, Brantley WA, Clark WAT, Xiao JZ, Papazoglou E (2003a). Transmission electron microscopic studies of deformed high-palladium dental alloys. *Dent Mater* 19:334-340.
- Guo WH, Brantley WA, Clark WAT, Monaghan P, Mills MJ (2003b). *Biomaterials* 24: 1705-1712.
- Hackle H, Miller K, Elsner P, Burg G (1991). Unusual combined sensitization to palladium and other metals. *Contact Dermatitis* 24:131-132.
- Herrera A, Kondic V (1979). The effect of porosity on tensile properties of two Al-Si alloys. *Solidification Cast. Met., Proc Inter Conf Solidification and Casting*. p 460-465.
- Hisatsune K, Hasaka M, Sosrosoedirdjo BI, Udoh K (1990). Age-hardening behavior in a palladium-based dental porcelain-fused alloy. *Mater Characterization* 25: 177-184.
- Horstemeyer MF, Yang N, Gall K, McDowell D, Fan J, Gullett P (2002). High cycle fatigue mechanisms in a cast AM60B magnesium alloy. *Fatigue Fracture Eng Mater Structures* 25:1045-1056.
- Huget EF, Civjan S (1974). Status report on palladium-silver-based crown and bridge alloys. *J Am Dent Assoc* 89:383-385.
- Huget EF, Dvivedi N, Cosner HE (1976). Characterization of gold-palladium-silver and palladium-silver for ceramic-metal restorations. *J Prosthet Dent* 36:58-65.

- Kerber SJ, Barr T, Mann G, Brantley WA, Papazoglou E, Mitchell JC (1998). The complementary nature of x-ray photoelectron spectroscopy and angle-resolved x-ray diffraction: II. Analysis of oxides on dental alloys. *J Mater Eng Perform* 7:334-342.
- Lacy AM, Hirose R, Jendresen MD (1977). Observation on the discoloration of low-fusing porcelain. *J Calif Dent Assoc* 5:44-49.
- Li D, Brantley WA, Guo WH, Clark WAT, Alapati SB, Heshmati RH, Daehn GS (2006). Fatigue limits and SEM/TEM of fracture characteristics for Pd – Ag alloys. *J Mater Sci: Mater Med* (in press).
- Li D, Brantley WA, Mitchell JC, Daehn GS, Monaghan P, Papazoglou E (2002). Fatigue studies of high-palladium dental casting alloys: Part I. Fatigue limits and fracture characteristics. *J Mater Sci: Mater Med* 13:361-367.
- Limkool P, Sumii T (1995). Study of a Pd–Ag–Sb system alloy for metal-ceramics. *Bull Tokyo Dental Coll* 36:103-114.
- Liu Z, Chen L, Zhao H, Wang Y, Wang Z, Klein F (2000). The influence of porosity of magnesium die casting alloys on its mechanical properties. *Metall* 54: 122-125.
- Mackert JR Jr, Ringle RD, Fairhurst CW (1983). High-temperature behavior of a Pd–Ag alloys for porcelain. *J Dent Res* 62: 1229-1235.
- Mayer HR, Lipowsky H, Papakyriacou M, Rosch R, Stich A, Stanzl-Tschegg S (1999). Application of ultrasound for fatigue testing of lightweight alloys. *Fatigue Fracture Eng Mater Structures* 22:591-599.
- Mayer H, Papakyriacou M, Zettl B, Stanzl-Tschegg SE (2003). Influence of porosity on the fatigue limit of die cast magnesium and aluminium alloys. *Int J Fatigue* 25:245-256.
- Mayer H, Papakyriacou M, Zettl B, Vacic S (2005). Endurance limit and threshold stress intensity of die cast magnesium and aluminum alloys at elevated temperatures. *Int J Fatigue* 27:1076-1088.
- Meyer JM, Reclaru L (1995). Electrochemical determination of the corrosion resistance of noble casting alloys. *J Mater Sci Mater Med* 6:534-540.
- Mezger PR, Vrijhoef MMA, Greener EH (1985). Corrosion resistance of three high-palladium alloys. *Dent Mater* 1:177-179.
- Mezger PR, Vrijhoef MMA, Greener EH (1989a). The corrosion behavior of high-palladium porcelain-bonding alloys. *J Dent* 17:33-37.

- Mezger PR, Stols ALH, Greener (1989b). Metallurgical aspects and corrosion behavior of yellow low-gold alloys. *Dent Mater* 5:350-354.
- Mezger PR, Vrijhoef MMA, Greener EH (1989c). The corrosion behavior of palladium–silver–ceramic alloys. *Dent Mater* 5:97-100.
- Mizumoto T, Niinomi M, Nakano Y, Akahori T, Fukui H (2002). Fatigue properties of cast Ag–Pd–Cu–Au–Zn alloy for dental applications in the relation with casting defects. *Mater Trans* 43:3160-3166.
- Mizumoto T, Niinomi M, Akahori T, Fuhui H (2003). Effects of casting defects and microstructure on fatigue properties of cast Ag–Pd–Cu–Au–Zn alloys for dental applications. *Mater Sci Forum [Part 4, THERMEC]* 426-432:3207-3212.
- Monroe R (2005). Porosity in castings. *Trans Amer Foundry Soc* 113:519-546.
- Mugica GW, Tovio DO, Cuyas JC, Gonzales AC (2004). Effect of porosity on the tensile properties of low ductility aluminum alloys. *Mat Res* 7:221-229.
- Murdoch RD, Pepys J (1986). Enhancement of antibody production by mercury and platinum metal halide salts. *Int Arch Allergy Appl Immunol* 80:405-411.
- Nielsen JP, Tuccillo JJ (1966). Grain size in cast gold alloys. *J Dent Res* 45:964-969.
- Niemi L, Herø H (1984). The structure of a commercial dental Ag–Pd–Cu–Au casting alloy. *J Dent Res* 63:149-154.
- Nitta SV, Clark WA, Brantley WA, Grylls RJ, Cai Z (1999). TEM analysis of tweed structure in high-palladium dental alloys. *J Mater Sci Mater Med* 10:513-517.
- O'Brien LA, German RM (1984). Compositional effects on Pd-Ag dental alloys [Abstract]. *J Dent Res* 63:175.
- O'Brien WJ, Boenke KM, Linger JB, Groh CL (1998). Cerium oxide as a silver decolorizer in dental porcelains. *Dent Mater* 14: 365-369.
- Odén A, Herø H (1986). The relationship between hardness and structure of Pd–Cu–Ga alloys. *J Dent Res* 65:75-79.
- Okamoto H (2000). In: Desk hand book phase diagrams for binary alloys. ASTM International, Materials Park, OH. p 10, 15, 20, 388, 487, 659.
- Papazoglou E, Brantley WA, Carr AB, Johnston WM (1993). Porcelain adherence to high-palladium alloys. *J Prosthet Dent* 70:386-394.

- Papazoglou E, Brantley WA, Mitchell JC, Cai Z, Carr AB (1996). New high-palladium casting alloys: Studies of the interface with porcelain. *Int J Prosthodont* 9:315-322.
- Papazoglou E, Brantley WA (1998). Porcelain adherence vs force to failure for palladium–gallium alloys: A critique of metal–ceramic bond testing. *Dent Mater* 14:112-119.
- Papazoglou E, Brantley WA, Johnston WM, Carr AB (1998). Effects of dental laboratory processing variables and in vitro testing medium on the porcelain adherence of high-palladium casting alloys. *J Prosthet Dent* 79: 514-519.
- Papazoglou E, Wu Q, Brantley WA, Mitchell JC, Meyrick G (1999). Mechanical properties of dendritic Pd-Cu-Ga dental alloys. *Cells Mater* 9: 43-54.
- Papazoglou E, Wu Q, Brantley WA, Mitchell JC, Meyrick G (2000). Comparison of mechanical properties for equiaxed fine-grained and dendritic high-palladium alloys. *J Mater Sci: Mater Med* 11:601-608.
- Papazoglou E, Brantley WA, Johnston WM (2001). Evaluation of high-temperature distortion of high-palladium metal-ceramic crowns. *J Prosthetic Dent* 85:133-140.
- Payan J, Moya GE, Meyer JM, Moya F (1986). Changes in physical and chemical properties of a dental palladium–silver alloy during metal–porcelain bonding. *J Oral Rehab* 13: 329-338.
- Pinasco MR, Cordano E, Giovannini M (1999). X-ray diffraction and microstructural study of PFM precious metal dental alloys under different metallurgical conditions. *J Alloys and Compounds* 289: 289-298.
- Reel DC, Kemper JT, Jones WB, Mitchell RJ (1986). A clinical comparison of Au–Pd and Pd–Ag PFM alloys [Abstract]. *J Dent Res* 65:237.
- Ringle RD, Mackert JR, Fairhurst CW (1986). Prevention of porcelain “greening” by external oxidation in a Pd–Ag–Mn–Al dental alloy system [Abstract]. *J Dent Res* 65:218.
- Samuel AM, Samuel FH (1995). Effect of melt treatment, solidification conditions and porosity level on the tensile properties of 319.2 endchill aluminum castings. *Journal of Materials Science* 30: 4823-4833.
- Sarkar NK, Berzins DW, Prasad A (2000). Dealloying and electroformation in high-Pd dental alloys. *Dent Mater* 16:374-379.
- Schaffer SP (1983). Novel palladium alloy and dental restorations utilizing same. U.S. Patent No. 4,387,072.

- Sigl KM, Hardin RA, Stephens RI, Beckermann C (2004). Fatigue of 8630 cast steel in the presence of porosity. *Inter J Cast Metals Res* 7:130-146.
- Stanzl-Tschegg SE, Mayer HR, Beste A, Kroll S (1995). Fatigue and fatigue crack propagation in AlSi7Mg cast alloys under in-service loading conditions. *Int J Fatigue* 17:149-155.
- Stavridakis MM, Papazoglou E, Seghi RR, Johnston WM, Brantley WA. Effect of different high-palladium metal-ceramic alloys on the color of opaque and dentin porcelain. *J Prosthetic Dent* 2004;92:170-178.
- Sun D, Monahan P, Brantley WA, Johnston WM (2002a). Potentiodynamic polarization study of the in vitro corrosion behavior of high-palladium alloys in five media. *J Prosthet Dent* 87: 86-93.
- Sun D, Monaghan P, Brantley WA, Johnston WM (2002b). Electrochemical impedance spectroscopy study of high-palladium dental alloys. Part I. Behavior at open-circuit potential. *J Mater Sci: Mater Med* 13: 435-442.
- Sun D, Monaghan P, Brantley WA, Johnston WM (2002c). Electrochemical impedance spectroscopy study of high-palladium dental alloys. Part II. Behavior at elevated potentials. *J Mater Sci: Mater Med* 13: 443-448.
- Sun D (2004). On the corrosion behavior and biocompatibility of palladium-based dental alloys. Ph.D. Dissertation, The Ohio State University, Columbus, OH, USA.
- Syverud M, Dahl JE, Herø H, Morisbak E (2001). Corrosion and biocompatibility testing of palladium alloy castings. *Dent Mater* 17:7-13.
- Tani T, Udoh K, Yasuda K, Van Tendeloo G, Van Landuyt J (1991). Age-hardening mechanisms in a commercial dental gold alloy containing platinum and palladium. *J Dent Res* 70:1350-1357.
- Tufekci E, Mitchell JC, Olesik JW, Brantley WA, Papazoglou E, Monaghan P (2002). Inductively coupled plasma-mass spectroscopy measurements of elemental release from 2 high-palladium dental casting alloys into a corrosion testing medium. *J Prosthet Dent* 87:80-85.
- Vaidyanathan TK, Prasad A (1981). In vitro corrosion and tarnish analysis of the Ag-Pd binary system. *J Dent Res* 60:707-715.
- Van Joost TH, Roesyanto-Mahadi (1990). Combined sensitization to palladium and nickel. *Contact Dermatitis* 22:227-228.

- Van Loon LAJ, Van Elsas PV, Van Joost TH, Davidson CL (1984). Contact stomatitis and dermatitis to nickel and palladium. *Contact Dermatitis* 11:294-297.
- Vermilyea SG, Huget EF, Vilca JM (1980). Observations on gold–palladium–silver and gold–palladium alloys. *J Prosthet Dent* 44:294-299.
- Vermilyea SG, Cai Z, Brantley WA, Mitchell JC (1996). Metallurgical structure and microhardness of four new palladium-based alloys. *J Prosthodont* 5:288-294.
- Vrijhoef MMA, Greener EH (1988). Some academic reflections on casting alloy patents. *Dent Mater* 4: 313-317.
- Walton TR, O'Brien WJ (1985). Thermal stress failure of porcelain bonded to a Palladium–silver alloy. *J Dent Res* 64:476-480.
- Wang QG, Apelian D, Lados DA (2001). Fatigue behavior of A356-T6 aluminum cast alloys. Part I. Effect of casting defects. *J Light Metals* 1:73-84.
- Wataha JC, Craig RG, Hanks CT (1991). The release of elements of dental casting alloys into cell-culture medium, *J Dent Res* 70:1014-1018.
- Wataha JC, Craig RG, Hanks CT (1995). Element release and cytotoxicity of Pd–Cu binary alloys. *Int J Prosthodont* 8:228-232.
- Wataha, JC, Hanks, CT (1996). Biological effects of palladium and risk of using palladium in dental casting alloys. *J Oral Rehabil* 23:309-320.
- Watanabe I, Watanabe E, Cai Z, Okabe T, Atsuta M (2001). Effect of heat treatment on mechanical properties of age-hardenable gold alloy at intraoral temperature. *Dent Mater* 17:388-393.
- Weinstein M, Katz S, and Weinstein AB (1962). Fused porcelain-to-metal teeth. U.S. Patent No. 3,052,982.
- Wu Q, Brantley WA, Mitchell JC, Vermilyea SG, Xiao J, Guo W (1997). Heat-treatment behavior of high-palladium dental alloys. *Cells Mater* 7: 161-174.
- Yi JZ, Gao YX, Lee PD, Flower HM, Lindley TC (2003). Scatter in fatigue life due to effects of porosity in cast A356-T6 aluminum-silicon alloys. *Metall Mater Trans* 34A:1879-1890.